Development and Implementation of an Adaptive PMP-Based Control Strategy for a Conventional Vehicle Electrical System

THESIS

Presented in Partial Fulfillment of the Requirements for the Degree Master of Science in
the Graduate School of The Ohio State University

By

Colin A. Waldman

Graduate Program in Mechanical Engineering

The Ohio State University

2014

Master's Examination Committee:

Professor Marcello Canova, Advisor

Dr. Shawn Midlam-Mohler

Abstract

This thesis details the development, implementation, and experimental testing of a supervisory energy management control strategy for the vehicle electrical system of a passenger car. The control strategy commands the alternator duty cycle such that vehicle fuel economy is optimized whilst the instantaneous load current demand is met and constraints on the system voltage and battery state of charge are satisfied.

To this extent, Pontryagin's Minimum Principle (PMP) is utilized alongside a vehicle plant model in order to evaluate the behavioral characteristics of the vehicle electrical system subjected to optimal control. These observations are employed in the development of an adaptive, PMP-based supervisory strategy capable of real-time control. Experimental testing of the in-house developed control strategy, termed "A-PMP", is benchmarked against a baseline production control strategy, demonstrating consistent improvements in vehicle fuel economy.

Dedication

This document is dedicated to my family, friends, and all those who have helped me during my time at The Ohio State University.

Acknowledgments

I am incredibly fortunate to have had the opportunity to work towards my Master of Science in Mechanical Engineering at The Ohio State University's Center for Automotive Research (OSU-CAR); an automotive-oriented academic institution full of brilliant students, faculty and staff. I would firstly like to extend my gratitude and thanks towards my graduate advisor, Dr. Marcello Canova, for providing me with such a well-rounded and exciting project. Dr. Canova has consistently challenged me to better myself, both from an academic and professional perspective, over the course of my MSME research; something which will (and already has) help me tremendously as I move forward in my own career. Dr. Lisa Fiorentini deserves a great deal of thanks for her assistance and guidance in the development of the adaptive, PMP-based control strategy (A-PMP). Dr. Shawn Midlam-Mohler deserves a notable mention, both for serving on my advisory committee and providing insight into the implementation of the A-PMP control strategy. Thank you to Dr. Yann Guezennec for sharing his acumen and expertise regarding lead-acid battery parameter identification, and much appreciation to Nick Warner and B.J. Yurkovich for their assistance in battery testing and data post-processing, respectively. A special thanks also to Eric Schacht for his near-infinite Labview expertise, Jim Shively for his patience and assistance in hardware development, and Keith Rogers for always being willing to help out with the chassis dynamometer.

Thank you to all of the graduate students at OSU-CAR who have provided me with a much-needed laugh from time to time. Finally, I must extend my greatest thanks to my mother – Kay Molt, my sister – Brenn Waldman, my father – Dr. W. James Waldman, my brother-in-law – Joshua Hinderliter, my stepfather – John Molt, and my girlfriend – Jamie Gavagan. My family has been my backbone and moral support throughout my studies at OSU, and words alone cannot adequately express my gratitude for this.

While my time spent at The Ohio State University seems all too short in hindsight, the memories I have formed over the past 6 years are priceless to say the least and will stay with me regardless of where I am or what I am doing. Columbus, OH and The Ohio State University will always be my home, and once again thank you to all of my friends, family, and academic colleagues and classmates.

Vita

2008	Dublin Scioto High School
2013	B.S. Mechanical Engineering, The Ohio State University
2013 to present	Graduate Research Associate, Department of Mechanical and Aerospace Engineering, Center for Automotive Research, The Ohio State University

Fields of Study

Major Field: Mechanical Engineering

Table of Contents

List of Tables

List of Figures

Chapter 1: Introduction

The modern era within the United States automotive industry has experienced tremendous growth, with the number of registered motor vehicles increasing steadily by an estimated 3.69 million units annually from 1960 to 2008 [1]. Only in 2009, following the automotive industry crisis, did the U.S. fleet decrease in size. Light vehicle sales in the U.S. have rebounded since 2009; Ford Motor Company, Chrysler LLC and GM experienced an overall sales increase of approximately 13.5% between 2012 and 2013 [2]. Furthermore, by the year 2020, global profits for automotive OEMs are expected to increase by almost 50% [3]. Figure 1 illustrates the growth in the number of registered motor vehicles from 1960 to 2009.

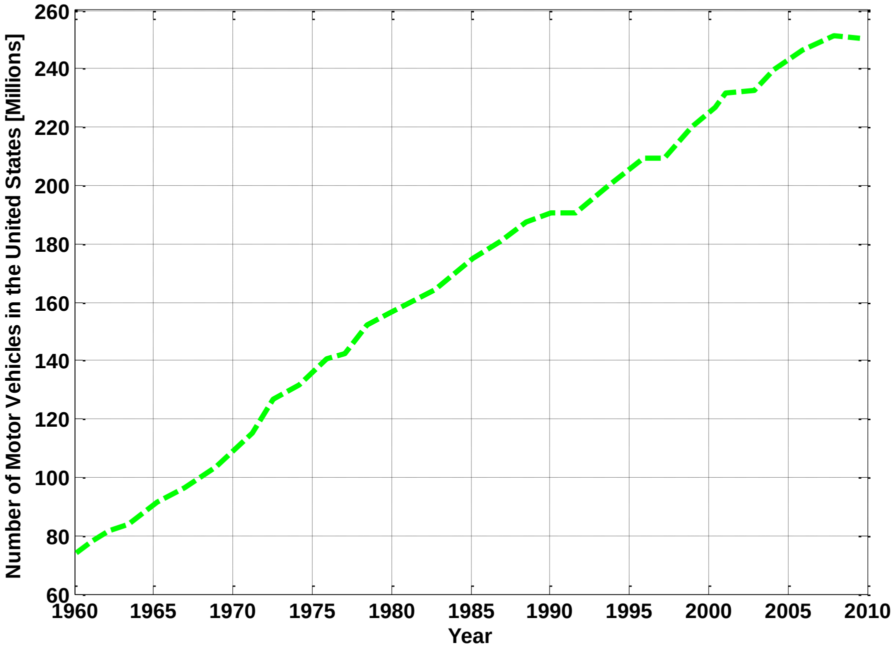

Figure 1: Growth in the number of U.S. Motor Vehicles [4]

From an environmental standpoint, this rapid growth presents a two-fold issue; an increasing number of petroleum-consuming vehicles both diminishes already dwindling oil supplies and invokes concern regarding the impacts of automotive exhaust byproducts on the ecosystem. For these reasons, the EPA and NHTSA have enacted stringent fuel economy and emissions policies on OEMs, with manufacturers who fail to achieve these policies either forced to purchase surplus credits from other manufacturers or pay heavy fines. Therefore, there is tremendous pressure on OEMs to look towards new and innovative methods to improve fuel economy across their entire fleet. Figure 2 depicts the United States CAFE compliance targets (in miles per gallon) for light-duty passenger vehicles up to model year 2025. With the EIA estimating a 40.3 mpg fleet-wide average for light-duty vehicles by model year 2021, it is clear that OEMs need to invest significant research into reducing vehicle fuel consumption.

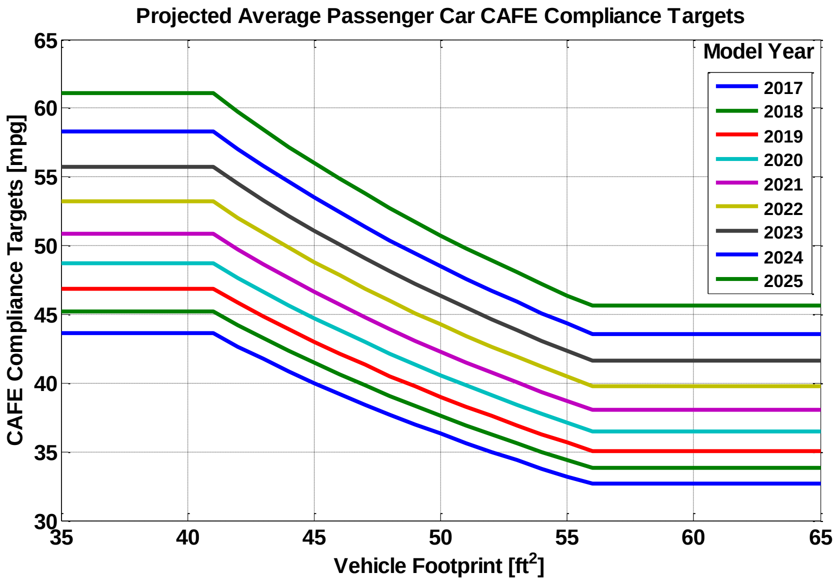

Figure 2: CAFE Compliance Targets [5]

The effort to improve vehicle fuel economy and emissions quality without compromising vehicle performance has resulted in an industry-wide push towards powertrain optimization, with OEMs investing significant effort in a wide variety of fuel-reduction technologies such as engine downsizing, cylinder deactivation, powertrain hybridization and electrification, and flexible valve actuation. Improvements in vehicle fuel economy, however, are not only limited to the benefits realized through optimizing engine efficiency. As illustrated in Figure 3, coolant losses, exhaust energy losses, and the losses associated with providing power to the ancillary loads all contribute to overall vehicle fuel economy and therefore provide suitable grounds for vehicle efficiency improvements.

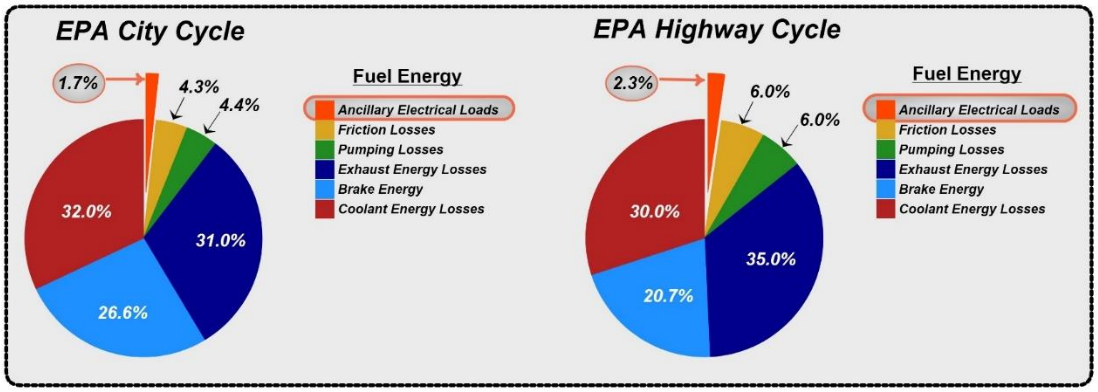

Figure 3: EPA City/Highway Fuel Consumption [6]

The parasitic losses associated with the ancillary electrical loads, induced by the alternator and transmitted through the auxiliary belt to the crankshaft, supply the electrical power required for automotive necessities and appliances such as component actuation, lighting, and infotainment systems. The management and control of these electrical loads, with the objective of minimizing vehicle fuel consumption, has been largely neglected in years past. However, as fuel economy mandates continue to challenge powertrain designers in the coming years, the vehicle electrical system will become an increasingly attractive reservoir of potential fuel savings.

The passenger vehicle electrical system has undergone dramatic changes throughout history in order to compensate for ever-increasing vehicular load demands. What began as a power system designed to satisfy in-cylinder ignition, cranking, and few (if any) lighting loads has developed over time into a complex electrical system which supplies power to various driver safety features, infotainment systems, control units, and electrical assist systems. For example, the Volkswagen Golf, a typical passenger vehicle, experienced a nearly 300% increase in the number of integrated ECUs from the 1998 to 2010 production model [7]. Furthermore, it is predicted that by the model year 2020, dual-voltage electrical systems composed of a 12/48V (nominal) battery pair will be commonplace within the automotive industry [8]. This will allow for the electrification of loads once mechanically coupled to the engine crankshaft, as well as the recuperation of the automobile's kinetic energy upon braking, improving overall vehicle fuel economy. Figure 4 illustrates the evolution and predicted trajectory of the typical commercial automotive electrical system, whereas Figure 5 demonstrates the increase in automotive electric power demand over time. Given the incorporation of increasingly complex electrical systems, one can easily imagine how quickly automotive electric power requirements will grow in the future.

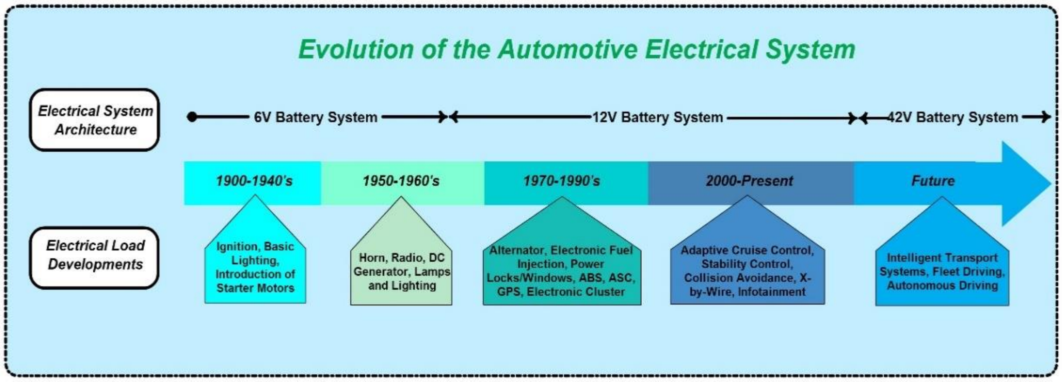

Figure 4: Evolution of the Automotive Electrical System [9].

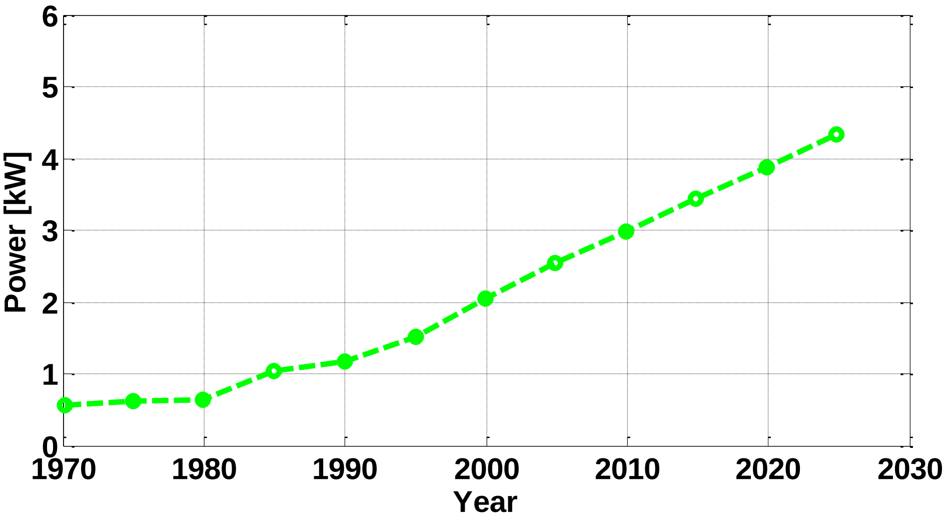

Figure 5: Predicted Automotive Electric Power Requirements [10].

Figure 5 depicts one possible trajectory for automotive electrical power requirements up to model year 2025, with power requirements predicted to more than double to approximately 4.5kW (6 HP) between 2000 and 2025. The automotive electrical system is inarguably responsible for a small, but increasingly significant percentage of overall vehicle fuel consumption compared with years past, and the relevance of these electrical systems can no longer be overlooked when optimizing for vehicle fuel economy. This, coupled alongside increasingly stringent fuel consumption and emissions policies enforced by the EPA (reference Figure 3), signifies that appreciable benefits may be recognized through control optimization and management of the automotive electrical system.

Section 1.1: Overview on the Role of Optimal Control Theory in the Energy Optimization of Advanced Vehicles

One promising method of vehicle electrical system control and optimization lies in the domain of optimal control theory. Optimal control theory, an extension of the well-known calculus of variations, allows for the control of the trajectory of a dynamic system in some “best way”, as defined by the user (i.e. minimization of fuel consumption). Optimal control theory’s origins may be traced all the way back to the 17th century, when the calculus of variations was first developed [11]. However, it was not until the development of the digital computer, first commercially available in the 1950’s, that optimal control theory truly found widespread application. In more recent years, the rise of the hybrid electric vehicle (HEV) has brought optimal control to the forefront of the automotive industry. The potential benefits brought about by the management and optimization of the various energy flows which accompany automotive hybridization makes optimal control-based strategies an attractive field of study [12-14]. For instance; dynamic programming (DP), while not implementable in real-time control systems, allows one to easily observe the optimal “power-split” trajectory of an HEV, given that the vehicle driving schedule is known a priori. This task is performed via a DP algorithm, which examines all possible trajectories between two points and selects the most “optimal” solution. A very simple illustration of how dynamic programming functions may be observed in the “shortest path” example featured in Figure 6. If the objective of the dynamic programming sequence is minimization of the total distance travelled from point A to point Z, then clearly path 2, with a net “distance” of 7 units, is the optimal trajectory. This same logic may be expanded to very complex engineering problems, however care should be taken as dynamic programming can become very computationally expensive when analyzing particularly detailed systems.

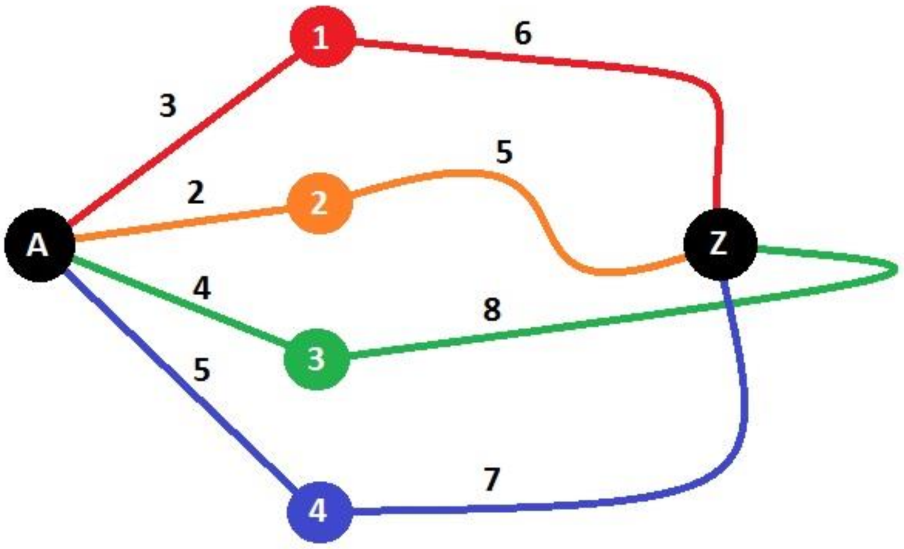

Figure 6: Shortest Path Dynamic Programming Example.

Referencing [15], the advantages that dynamic programming present over a baseline rule-based control strategy are significant, and upwards of an 18% reduction in fuel consumption may be achieved over a single UDDS drive cycle. Dynamic programming may therefore be utilized as a benchmarking tool to evaluate the efficacy of online, sub-optimal control strategies. In the same study, a control strategy termed the Equivalent Consumption Minimization Strategy (ECMS), based off of Pontryagin’s Minimum Principle, yields fuel savings of approximately 12%. The ECMS control strategy effectively weights usage of the chemical energy stored within the automotive battery against the consumption of fuel by the internal combustion engine in order to determine the optimal power split and, similar to dynamic programming, cannot be implemented into real-time control without some adaptions being made first. The development of an adaptive-ECMS controller, implementable in real-time, utilizes feedback from the battery state of charge to realize fuel savings only 1-2% lower than that of an ideally tuned ECMS model [16]. In a study performed at OSU, a control strategy utilizing Pontryagin's Minimum Principle demonstrates the flexibility of optimal control theory, minimizing cumulative PHEV tailpipe and corresponding power-plant carbon dioxide emissions in place of fuel consumption [17].

The benefits of optimal control within the automotive sector certainly are not limited to applications involving hybrid electric vehicles. Conventional powertrain automobiles with a standard, 12V charging system exhibit significant improvements in fuel economy when subjected to implementable control. Research indicates that quadratic programming has been successfully applied to the electrical system of a conventional powertrain automobile, leading to experimental fuel economy improvements of up to 2.6% on a Ford Mondeo [18]. In a separate study performed at The Ohio State University's Center for Automotive Research, the efficacy of the well-known ECMS control strategy is evaluated side-by-side, in simulation, with a standard commercial control scheme, demonstrating fuel economy improvements of up to 1.5% on a vehicle [19].

The rapid rise of information and communication technology, particularly developments in Vehicle-to-Vehicle and Vehicle-to-Infrastructure communication, has allowed for a very promising application of optimal control; intelligent transportation systems (ITS). By enabling inter-vehicle communication, large, densely-packed arrangements of automobiles (termed “platoons”) may be formed. These tight formations ideally reduce the cumulative aerodynamic drag on the platoon, improving fuel economy while cutting down on roadway congestion. One particular study even points towards fuel savings ranging from 5-15% in an optimal control, heavy-truck platooning application [20]. Figure 7 illustrates the general concept of platooning and intelligent transport systems.

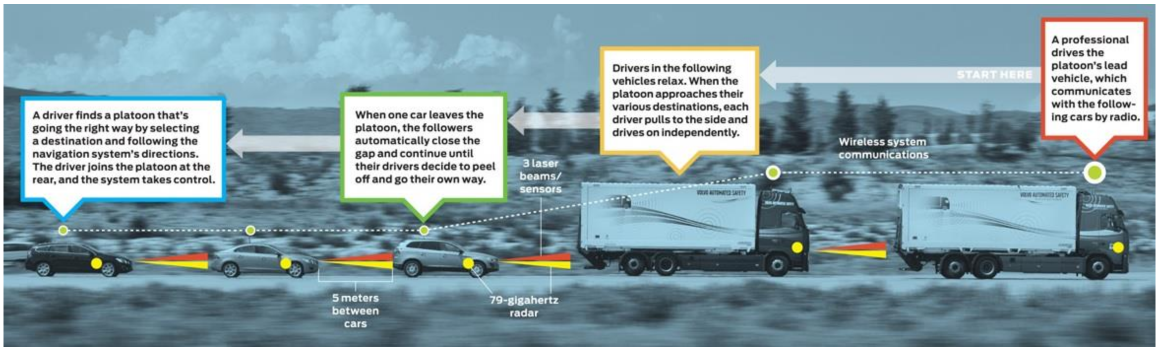

Figure 7: Intelligent Transport Systems, Platooning Scenario [Volvo].

The benefits of optimal control in the ITS industry go beyond improving vehicle fuel economy; by allowing automobiles to access information regarding surrounding road conditions, the optimal vehicle trajectory with respect to net time travelled may be developed and adapted in real time. This not only improves driver comfort, but also provides a partial solution to the issue of increasingly crowded metropolitan transportation systems. As ITS-enabling technologies gain a foothold in the United States and become commonplace in the automotive sector, significant research effort will likely be dedicated towards the study of automotive platooning and fleet management optimal control.

With the advent of the digital age in the 1950's, optimal control theory has become an increasingly valuable tool to engineers. The adaptability of optimal control theory allows for widespread application in the automotive sector, from determining the most time-effective path to an end destination, to minimizing an individual vehicle's fuel consumption and exhaust emissions, and even utilizing Intelligent Transport System data to reduce net time spent in traffic and maximize fleet fuel economy. As consumer dependence on automotive electronics continues to grow and CAFE regulations stress OEMs to look to new and innovative methods of reducing fuel consumption, the integration of optimal control-based strategies will prove a cost-effective solution.

Section 1.2: Scope of Work

The Ohio State University's Center for Automotive Research (OSU-CAR) is working in conjunction with Chrysler Group LLC and the U.S. Department of Energy in order to develop advanced powertrain technologies which demonstrate an overall fuel economy improvement, on a Vehicle, of 25% over the Federal Test Procedure drive cycle. As part of the team dedicated to this effort, OSU-CAR is responsible for the development of a supervisory vehicle energy control strategy for vehicle ancillary loads which should improve fuel economy through an improved coordination of the main vehicle energy consumers. These improvements are recognized through the management and reduction of the ancillary loads, as well as the management of the vehicle thermal system. The focus of this document is on the development and implementation of an ancillary load reduction (ALR) control strategy.

Section 1.3: Document Layout

The remainder of this thesis is structured as follows:

- Chapter 2 first describes the various experimental setups used to develop the comprehensive Vehicle Electrical System (VES) model. An in-depth discussion regarding the numerous designs of experiments used to develop the model is then laid out. The structure of the VES model is discussed from a component level, followed by validation of the VES model.
- Chapter 3 begins with a general discussion regarding the VES optimal control problem. An in-depth analysis of a single VES optimal control scenario is then performed. The robustness of the control strategy is then investigated through various sensitivity analyses. Finally, this analysis is expanded to numerous scenarios, and the overall behavior of the optimal control strategy is characterized.
- Chapter 4 discusses, in effect, how the gap was bridged between a non-implementable optimal control strategy and a real-time capable VES controller. The adaptations made to the optimal control strategy in order to realize an online

controller are first discussed. The impact of these adaptations on both plant behavior and fuel economy are then investigated. Finally, the experimental improvement in vehicle fuel economy for the Chrysler Town & Country over numerous drive cycles is presented.

- Chapter 5 concludes the work performed on the Ancillary Load Reduction (ALR) project, highlighting the critical findings of the study and indicating potential directions for future work.

Chapter 2: Model Development, Calibration, and Validation

The development, design, and integration of a control strategy is typically an iterative process, which requires the designer to build, calibrate, test and modify new designs. The use of physics-based or empirically-derived system models are essential to this process, allowing the designer to perform several tasks in an accelerated environment with little to no hardware in hand. When considering a complex, multi-domain system, for instance the electrical infrastructure of a conventional automobile, the advantages that a system model presents become quite evident. The lengthy process of designing an experimental setup, testing a control algorithm, performing data acquisition, and post-processing may be significantly expedited, with time instead spent on control design improvements. For this reason, a Vehicle Electrical System (VES) model has been developed to facilitate in the energy analysis of an automotive electrical system and control algorithm development. This chapter first outlines the various experimental setups employed for the calibration and validation of the VES model. A brief overview of the vehicle fuel consumption model is then presented, followed by a more in-depth discussion regarding the development and validation of the vehicle electrical system model.

Section 2.1: Experimental Setup Overview

A reliable and robust design of experiment is required to ensure that a simulation model provides realistic and accurate results, a basic requirement for any energy management supervisory control. Numerous experimental setups are utilized for this purpose. The use of a chassis dynamometer, a 2011 Vehicle, and ETAS rapid prototyping equipment were employed to allow for the development and validation of the VES model, as well as for the proceeding implementation of the energy management control strategy. In addition, the development of the battery model required a separate experimental set-up, consisting of an environmental chamber and a programmable load/supply system.

2.1.1: Description of the Test Vehicle Setup

A 2011 Chrysler Town and Country minivan was available for testing at The Ohio State University Center for Automotive Research (OSU-CAR). The main vehicle specifications are given in Table 1 below.

Table 1: Vehicle Specifications

Make, Model, and Year	Chysler Town & Country, 2011
Engine	DOHC 24-valve V-6, 3604 cc
Transmission	62TE 6-Speed Automatic
Gear Ratio:1	4.127 – 2.842 – 2.284 – 1.452 – 1.0 – 0.69
Axle Ratio	3.16
Mass (kg)	2154
Frontal Area (m^2)	2.42
Drag Coefficient (C_d)	0.33

The test vehicle was installed on a light-duty chassis dynamometer available at CAR with real-time driver feedback monitoring and recording live data from the vehicle. This setup allowed for a level of experimental repeatability that may otherwise be difficult to achieve. The use of a chassis dynamometer, as opposed to an engine dynamometer, also allows one to observe the complex, multi-domain (electro-mechanical) dynamics that exist within modern-day automobiles. Take, for example, the interactions between an engine, the vehicle electrical system, and the numerous peripheral devices that are driven by the auxiliary belt. By utilizing a chassis dynamometer, the effects of the various electrical loads may be investigated, whereas with an engine dynamometer these effects are typically ignored. The light-duty chassis dynamometer at The Center for Automotive Research is equipped with two 24” rollers and is capable of handling up to 150 HP. A Labview VI containing both the vehicle velocity profile and the desired vehicle speed trace (if any) is displayed on a monitor to facilitate the driver in reproducing regulatory or custom-made drive cycles. Figure 8 depicts the experimental chassis dynamometer setup, complete with the drivers-aid display and the 2011 Vehicle.

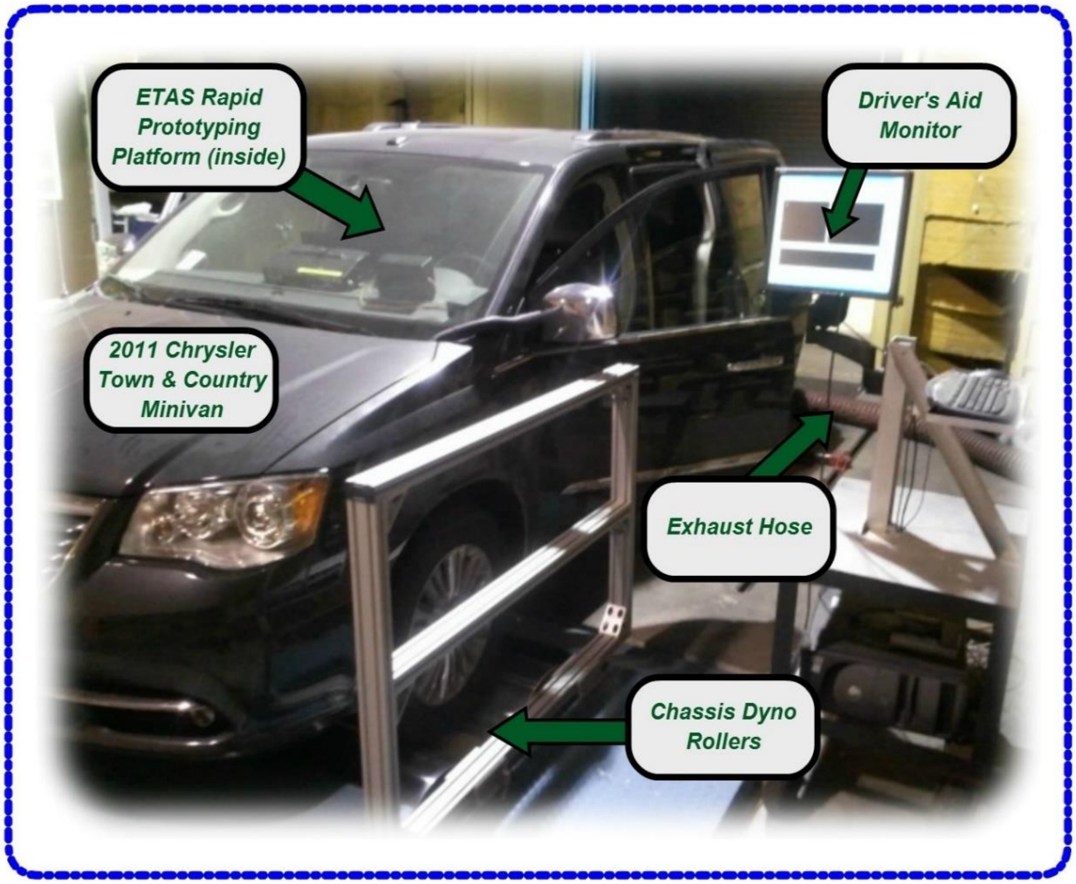

Figure 8: Overview of the Test Vehicle and Light-Duty Chassis Dynamometer at CAR.

2.1.2: Description of the Vehicle Electrical System Test Setup

Real-time measurement and data acquisition of the various dynamic variables and states that exist within the vehicle's electrical system is of the utmost importance in the development of the Vehicle Electrical System model and validation of the vehicle energy supervisory control strategy. An ETAS ES1000.3 rapid prototyping platform coupled with Intecrio software allows for data acquisition and control testing. Shunts routed to an

ES1303 A/D board allow for measurement of the battery current, alternator current, and cumulative electrical load demand, while an ETAS ETK-ECU interface gives direct access to the control variables and parameters of the vehicle ECU. In addition to the data acquisition setup, an ETAS ES1310 D/A board in conjunction with a PWM driver allows for the override of the production control strategy for the vehicle alternator. This feature allows one to implement and test control algorithms for the electrical system, as discussed in Chapter 4. Finally, a programmable load was also required for fully characterizing the vehicle electrical system, simulating the impact of auxiliary electrical loads in a controllable and repeatable fashion. The use of a chassis dynamometer, ETAS rapid prototyping and data acquisition platform, and the programmable load/supply allows for a full characterization of the vehicle electrical system. A simplified schematic of this experimental setup is featured in Figure 9. The physical setup of the ETAS system, in the backseat area of the minivan, is pictured in Figure 10.

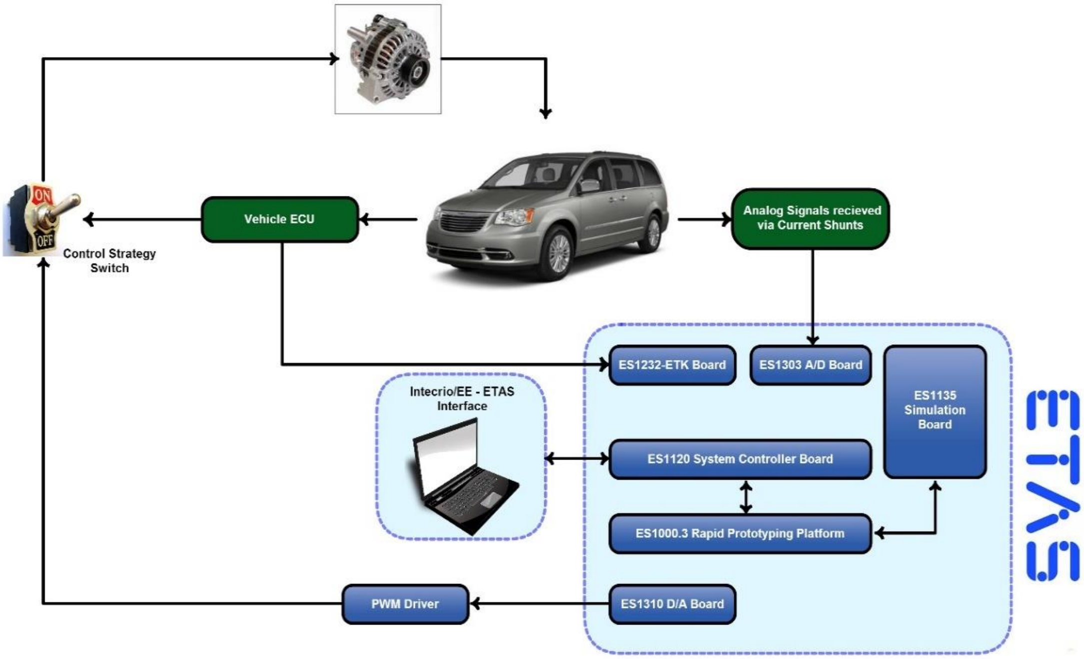

Figure 9: Schematic of the Vehicle Electrical System Test Setup.

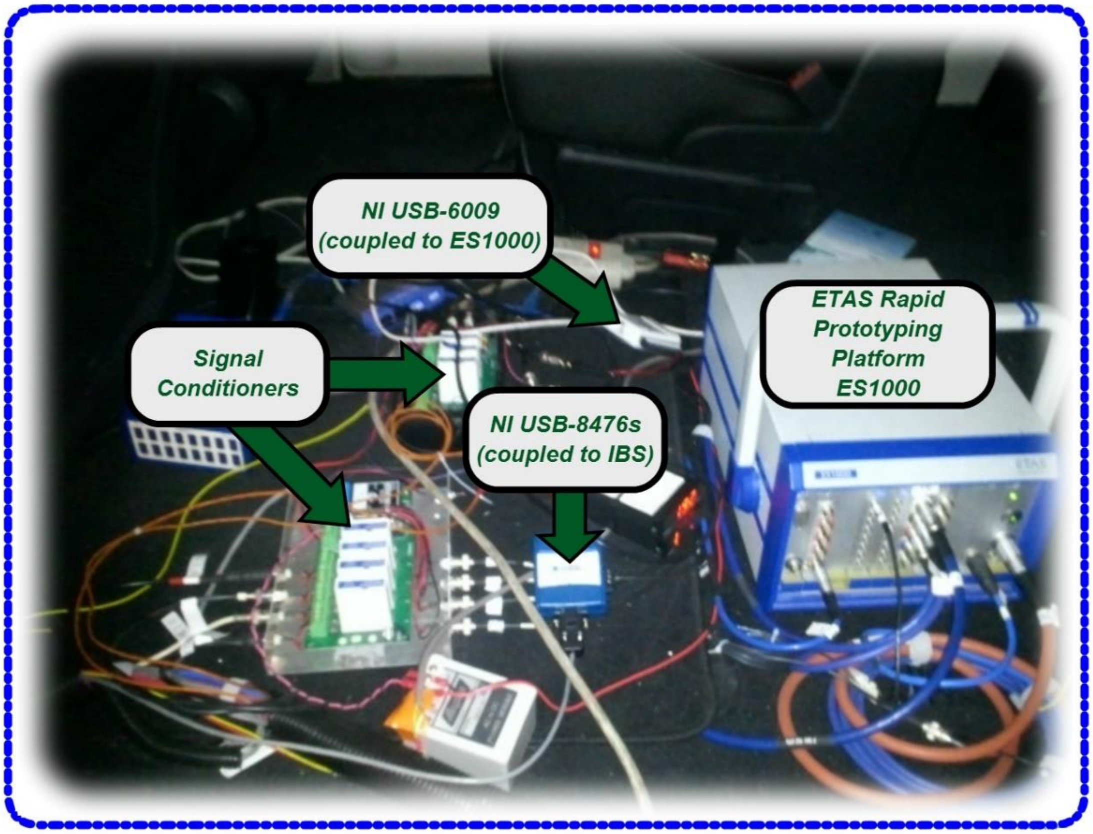

Figure 10: ETAS Experimental Setup

2.1.3: Description of the Battery Testing Experimental Setup

A standalone experimental setup for the battery present in the Chrysler vehicle allows for one to conduct tests in a more controlled environment than what is possible with a test vehicle. Battery parameter calibration and model validation are more easily performed on a standalone battery setup due to the ability to accurately control the input current profile and the thermal boundary conditions. Table 2, featured below, summarizes the main specifications of the VES battery.

Table 2: Automotive Battery Specifications

Type	Lead-Acid, Flooded
Nominal Voltage (V)	12
Nominal Capacity (Ah)	75
Maximum Charging Current (A)	120

In order to control the electrical loads on the battery, determine the temperature-dependent battery model parameters, and facilitate the deployment of the numerous experiments required to fully characterize a battery model, a Testequity Model 140 environmental chamber and a Maccor Series 4000 programmable load/supply are utilized. The Maccor battery cycler allows for the user to define current profiles, such as constant current – constant voltage (CC-CV) charge/discharge profiles or custom-made current profiles, integrate looped combinations of these profiles, and record the resultant current and voltage traces to a test computer for data post-processing. These tests may be repeated at numerous set temperatures through the use of the environmental chamber. Figure 11 depicts this experimental setup.

Figure 11: Experimental Setup for Battery Testing (Left: Environmental Chamber with Instrumented Batteries; Right: Maccor Battery Cycler).

Section 2.2: Overview of the Engine Fuel Consumption Model

The development of an accurate engine fuel consumption map is crucial to evaluating the impact of a vehicle energy supervisory control strategy on fuel economy. To this extent, Chrysler provided a set of engine experimental data (termed “Big Grid”) consisting of 247 steady-state engine speed and torque combinations. For each engine operating point, a complete set of variables characterizing the breathing, fuel injection, combustion, torque generation and emissions performance of the engine was available. From the given experimental data, a simple fuel consumption map was built as a function of the engine speed and torque inputs. This model is purely algebraic, and therefore does not take into account any dynamic effects on the engine fuel consumption. While this approximation would be inaccurate for the simulation of the engine dynamics, it is compatible with the purpose of evaluating vehicle fuel consumption over extended periods of time, such as drive cycles. In this case, the breathing and fuel dynamics of the engine, which affect the fast dynamics of the engine torque output, are negligible, allowing for a static fuel consumption model to be considered sufficiently accurate. Figure 12 depicts the block diagram of the fuel consumption model.

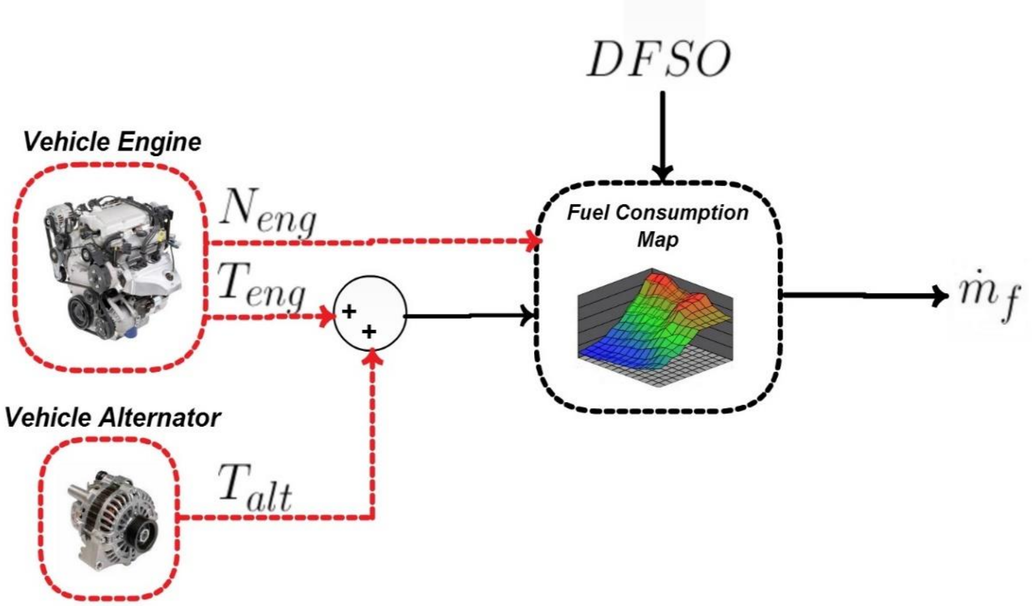

Figure 12: Block Diagram of the Engine Fuel Consumption Model.

The fuel consumption model takes both the engine speed and the sum of the engine and alternator torques as inputs, and outputs the fuel mass flow-rate. This allows one to quantify the impact of the alternator power consumption on the vehicle fuel economy once the engine fuel consumption model is integrated into the Vehicle Electrical System model. The additional input, termed DFSO, accounts for the engine deceleration fuel shut off, and sets the instantaneous fuel consumption to zero when active. A linear curve-fitting approach is utilized as the method of interpolation to interpolate the experimental fuel consumption and populate the map. Figure 13 depicts the fuel consumption data points and resulting fitted lines.

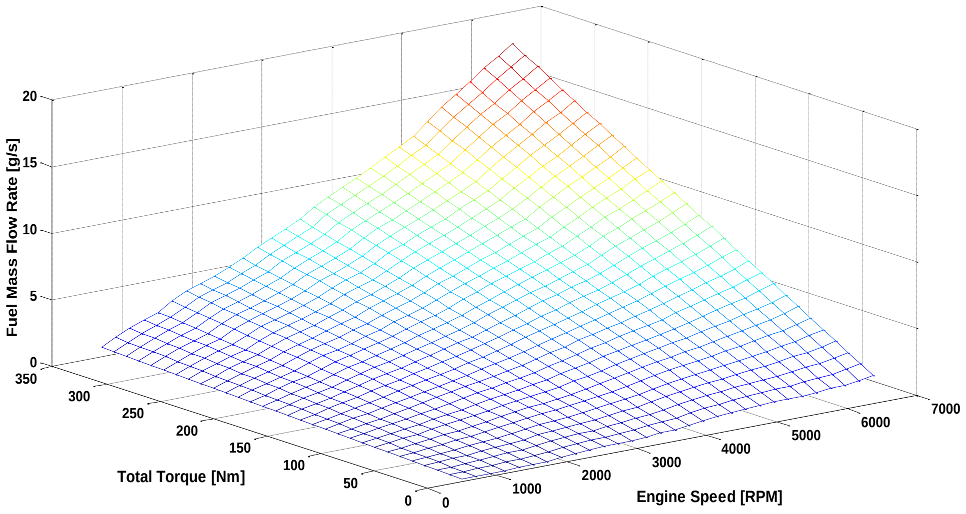

Figure 13: Linear Fit of Fuel Mass Flow Rate.

Section 2.3: Description of the Vehicle Electrical System Model

A model of the Chrysler Town and Country's electrical system is necessary for the successful design of an energy management control strategy. In order to develop the vehicle electrical system model, three subsystem models, namely the alternator, battery and Chrysler controller (termed "Electronic-Voltage Regulator, or "EVR"), are developed and independently validated. Figure 14 presents a block diagram showing the cause and effect relationships of the three interconnected models.

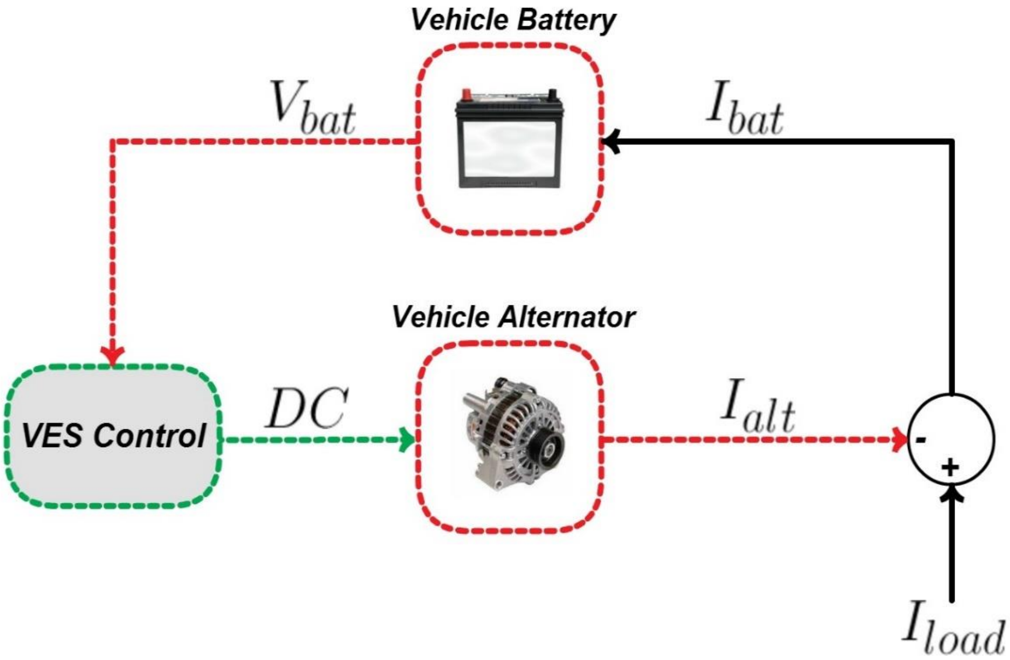

Figure 14: Block Diagram of the Vehicle Electrical System Model.

The Electronic-Voltage Regulator is a model that mimics the production control strategy for the electrical system. The algorithm monitors the battery voltage and outputs the appropriate duty-cycle (DC) PWM signal to the alternator with the objective of maintaining a nominal, temperature-dependent reference battery voltage. The duty-cycle command results in an increase in the alternator field current, thus increasing the alternator output current. The difference between the electrical load demand and the alternator current is the current directed to the battery. The alternator, battery, and EVR model will all be described in greater depth in the following sections, followed by an analysis of the entire vehicle electrical system model.

2.3.1: Alternator Model

Numerous methods are available to model the input-output response of an automotive alternator, ranging from the more complex and calibration-intensive circuit models to the simpler, empirically-derived “black-box” models. [21] discusses the development of an alternator circuit model in great detail. This type of approach is useful in capturing the high-frequency dynamics of the electric generator and the switching behavior of the AC/DC converter, and is typically used for electrical system fault diagnosis or actuator-level control design. In this work, an experimentally-derived, map-based alternator model will be integrated into the vehicle electrical system model. Maps provided by Chrysler for both the alternator torque and alternator efficiency were supplemented by OSU-generated maps for the field current and the resultant alternator current. The general form of these four look-up tables is described in Equations 1, 2, 3 and 4 below, followed by Figure 15 which features contour plots depicting each output variable for a fixed battery voltage:

$$T_{alt} = T_{alt}(\omega_{alt}, I_f, V_{bat}) \tag{1}$$

$$\eta_{alt} = \eta_{alt}(\omega_{alt}, I_f, V_{bat}) \tag{2}$$

$$I_{alt} = I_{alt}(\omega_{alt}, DC, V_{bat}) \tag{3}$$

$$I_f = I_f(\omega_{alt}, DC, V_{bat}) \tag{4}$$

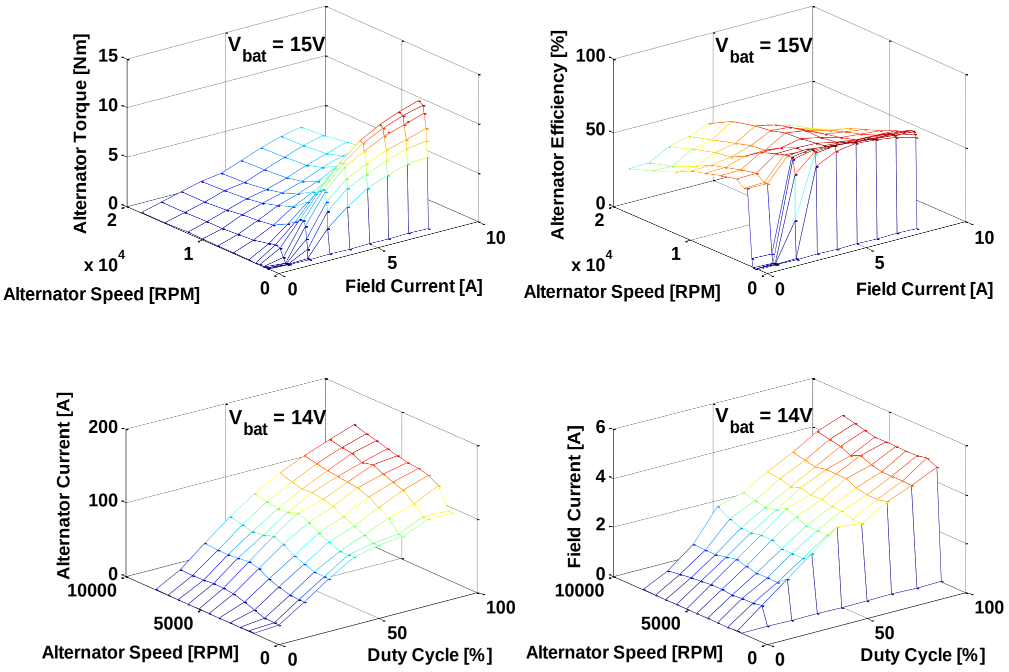

Figure 15: Alternator Contour Plots for a Fixed Battery Voltage.

The field current and alternator current maps, both considered functions of the alternator duty-cycle, rotor speed, and battery voltage, are developed with the assistance of the vehicle experimental setup (reference Section 2.1.3). The light-duty chassis dynamometer, a vehicle modified with shunts to monitor the alternator and field currents, a programmable load to fix the battery voltage, and a PWM driver which controls the duty cycle are utilized for this purpose. With all three model inputs fully controlled, steady-state data is then extracted via an ETAS ES1000.3 rapid prototyping platform, post-processed, and incorporated into the corresponding look-up tables. The block diagram depicting the alternator model may be observed in Figure 16. Take note that RR_{alt} is the reduction ratio across the engine crank and alternator pulleys.

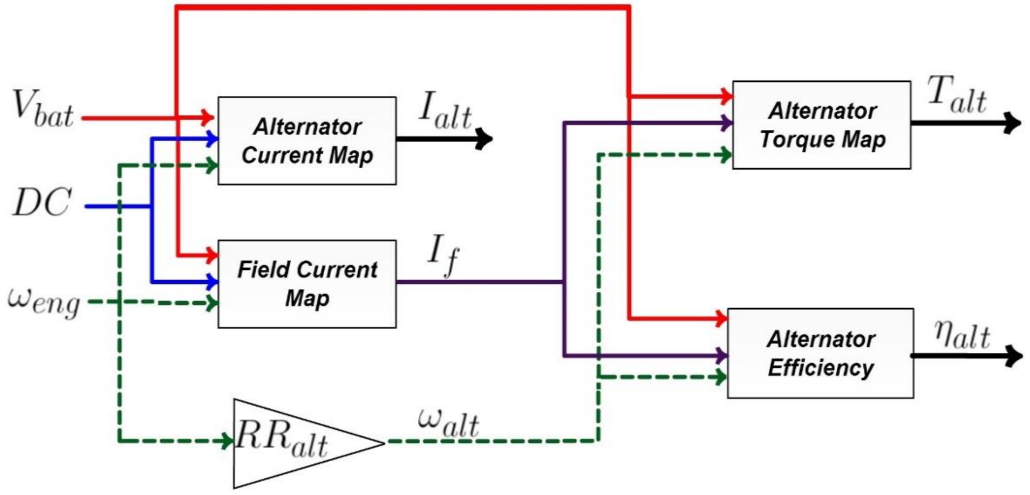

Figure 16: Block Diagram of the Alternator Model.

2.3.2: Battery Model

Modeling the voltage response of lead-acid batteries is a well-known process, which has been approached by many researchers in the past [22-24]. In this context, several modeling approaches have been proposed, depending upon the particular requirements and the objectives of the model. For instance, electrochemical lead-acid battery models have been developed to predict the very complex thermal and chemical interactions between the electrodes and electrolyte [24]. Such models, while useful to explain the voltage output behavior from first principles, are often too complex for integration into an electrical system model for control development. On the other hand, equivalent electrical circuit models offer a trade-off between accuracy and complexity that favors the application of model-based control. These models typically relinquish a certain degree of accuracy and physical consistency in exchange for increased simplicity. Despite the simplistic nature of such a model, the overall input-output behavior of a battery may be captured for a variety of operating conditions assuming that proper calibration of all parameters is performed [22, 23].

In this work, the dynamics of the battery are modeled as a 1st order Randle equivalent circuit [25]. Figure 17 depicts the equivalent circuit used in the model, with the relevant model parameters.

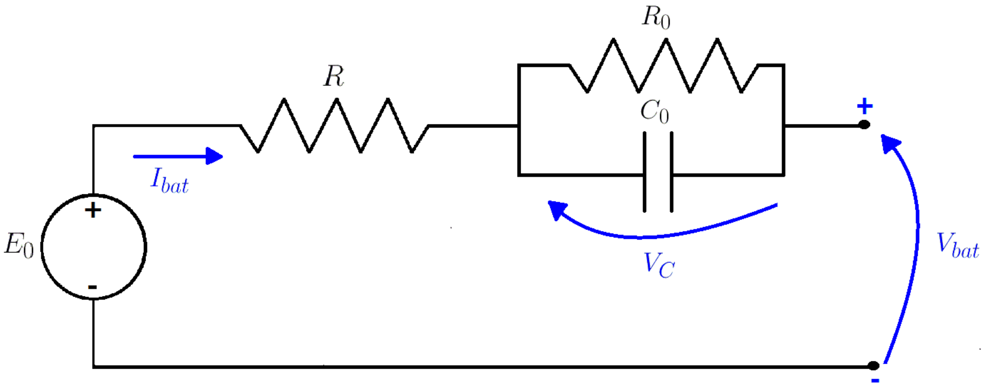

Figure 17: First-Order Battery Equivalent Circuit Model

The model consists of an ideal voltage source, E_0, a linear resistive element, R, and a parallel combination of a resistor and capacitor, R_0 and C_0, connected in series with the voltage source and resistive element. The battery voltage, as observed at the battery terminals, may be determined from the following circuit equation:

$$V_{bat} = E_0 - RI_{bat} - V_c \tag{5}$$

The dynamics of the battery voltage are therefore contingent upon the capacitive term (V_c) in Equation 5. The governing equation for the voltage drop across R_0 and C_0 can be expressed as follows [26]:

$$\frac{dV_c}{dt} = -\frac{V_c}{R_0 C_0} + \frac{I_{bat}}{C_0} \tag{6}$$

In order to fully define the battery model, it is necessary to calibrate the four battery parameters: E_0, R, R_0 and C_0. It is common practice to model these parameters as functions of the battery state of charge (SOC), temperature (T_{bat}), C-rate, and the sign of the battery current [27, 28]. To reduce the complexity of the required calibration procedure and the resulting parameter maps, the sign of the battery current and the C-rate are combined into a single variable, termed the current level (I_{level}). The battery SOC and current level are defined as follows:

$$SOC = SOC_0 - \frac{1}{Ah_{nom}} \int_{t_0}^{t_f} I_{bat} dt \tag{7}$$

$$I_{level} = sign(I_{bat}) \cdot Ah_{nom} \cdot C - rate \tag{8}$$

Where Ah_{nom} is the nominal battery capacity in ampere-hours, SOC_0 is the initial battery capacity, and $sign(I_{bat})$ denotes the sign of the battery current (positive for discharge, negative for charge).

The battery parameters can therefore be expressed in the following form:

$$E_0 = f(SOC, T_{bat}) \tag{9}$$

$$R, R_0, C_0 = f(SOC, T_{bat}, I_{level}) \tag{10}$$

The calibration and validation of the battery model required a thorough set of experiments, which were performed on the battery test bench described in Section 2.1.3. Specific testing procedures were engineered to provide a set of experimental data that allowed for separately calibrating the key model parameters.

Prior to the identification of the equivalent circuit parameters, the nominal capacity (Ah_{nom}) of the battery was determined. This procedure is outlined as follows, and is graphically depicted in Figure 18 for clarity:

1. The battery is fully charged utilizing a CC-CV (constant current, constant voltage) profile.
2. The battery is fully discharged at a constant current of 0.1C.
3. The battery is then fully charged to the upper voltage threshold by using a CC-CV profile.

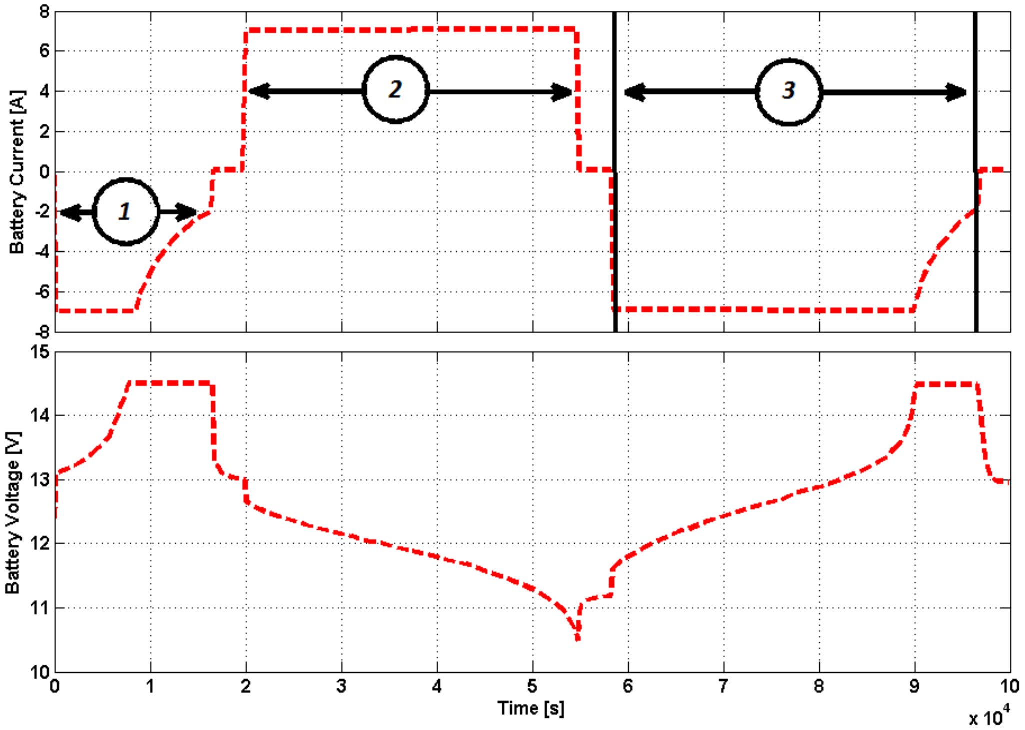

Figure 18: Current and Voltage Profile for Battery Capacity Test

The battery is considered fully discharged when the battery voltage reaches 10.5 V. Similarly, the battery is considered fully charged when the battery voltage reaches 14.5 V and the battery current drops below 2 A. The charge and discharge capacities (determined by steps 2 and 3, respectively) are then averaged, resulting in a nominal battery capacity of 72.3 Ah. This procedure was only performed once in order to minimize the excessive battery aging that would be induced by the deep-cycling of a flooded lead-acid battery. The aging may manifest itself as sulfation on the plates of the lead-acid battery, reducing the apparent battery capacity and increasing the internal resistance [29].

The second experimental test conducted on the battery was oriented towards the determination of the open-circuit voltage (E_0) which is generally assumed a function of the battery SOC and temperature [27, 28]. The experimental procedure designed for determining E_0 is summarized as follows:

1) The battery is fully discharged.
2) The battery is charged at a constant current level in order to increase the battery SOC by 5%.
3) The battery is rested sufficiently, and the open-circuit voltage is approximated as the voltage measured across the battery terminals.
4) Steps 2 and 3 are repeated until the battery is charged to 100% SOC
5) The battery is discharged at a constant current level in order to decrease the battery SOC by 5%.
6) The battery is rested sufficiently, and the open-circuit voltage is approximated as the voltage measured across the battery terminals.
7) Steps 5 and 6 are repeated until the battery is completely discharged.
8) The battery is charged to 100% SOC.
9) Steps 1-8 are performed at temperatures of $25^\circ C$, $40^\circ C$, and $50^\circ C$.

From the above procedure, two curves were generated for each temperature, one describing the relationship between the open-circuit voltage and the battery SOC when the battery is charging, and a similar curve for battery discharge. The two curves were then averaged to produce the open-circuit voltage E_0 as a function of the battery state of charge. The results for all three battery temperatures is illustrated in Figure 15. The upper-left, upper-right, and lower-left plots show the open-circuit voltage curves for temperatures of 25, 40, and 50 degrees Celsius, respectively. The lower right plot shows the averaged open-circuit voltage plots for all three temperatures.

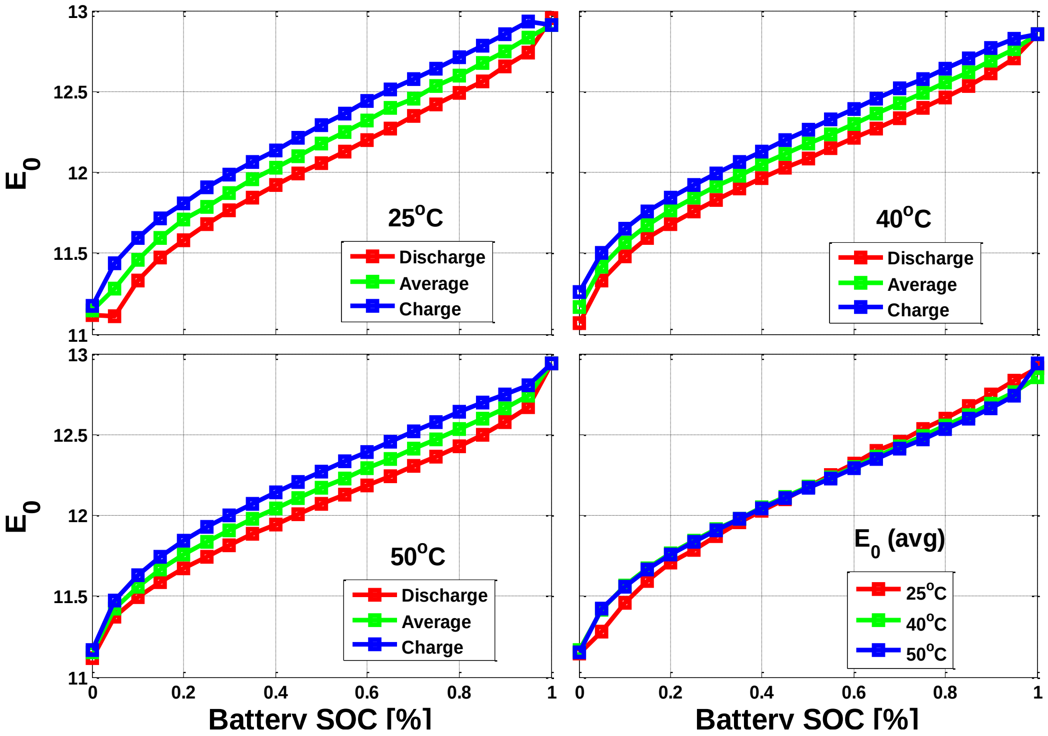

Figure 19: Summary of the Open-Circuit Voltage Characterization Test.

Finally, the equivalent circuit model parameters, $R, R_0,$ and C_0 were all determined through a single, extensive test where a transient current profile was imposed by the programmable load and supply system. In order to develop a model accurate for a wide range of operating conditions, the battery was subjected to numerous current levels and current steps of varying magnitude. The parameter values were then averaged across all current steps at each current level. A brief summary of this experimental procedure is detailed as follows:

1) The battery is charged to 100% SOC utilizing a CC-CV profile
2) A current profile composed of numerous current levels and current steps of various magnitudes and sign is imposed on the battery.
3) The battery is discharged at constant current to a new state of charge.
4) Steps 2 and 3 are repeated until a predetermined cutoff SOC is reached.
5) Steps 1-4 are performed at temperatures of $25^{\circ}C$, $40^{\circ}C$, and $50^{\circ}C$.

Figure 20 illustrates the parameter identification procedure, evaluated for just one battery SOC value. The numbers in the figure indicate the current profile for steps 1, 2 and 3 described above.

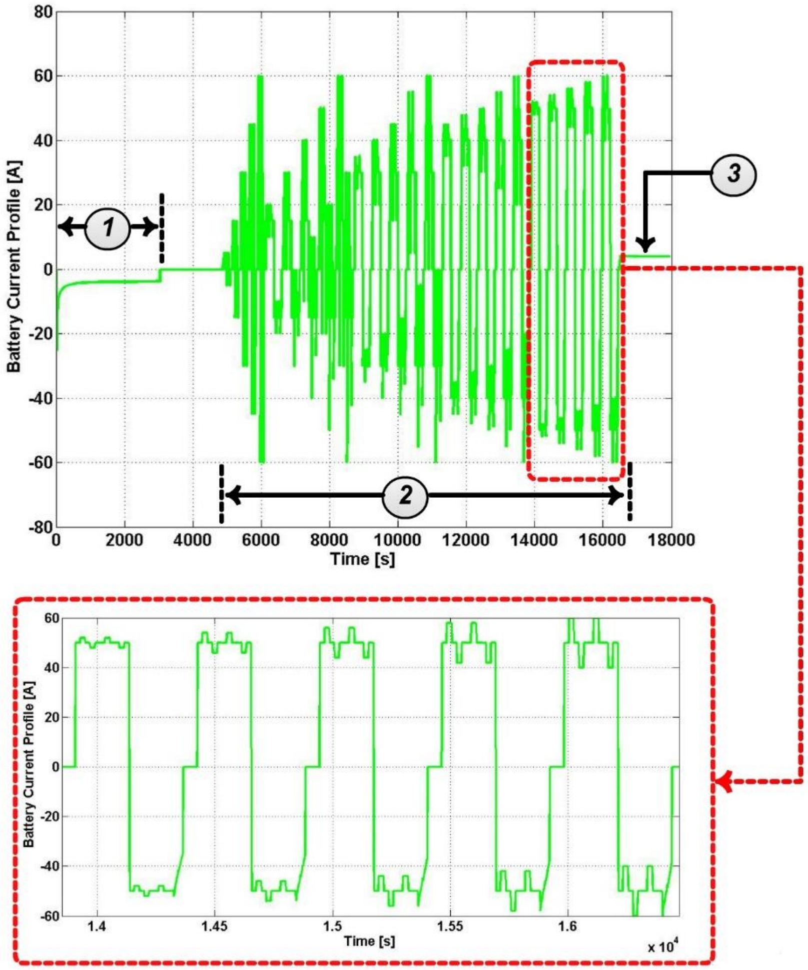

Figure 20: Current Profile for the Identification of Battery Model Parameters.

The values for $R, R_0,$ and C_0 were then determined following the identification procedure described in [30].

Following the initial calibration procedure, the model parameter values were smoothed with respect to the battery state of charge and current level in order to ensure continuity of the predicted voltage output. This task was performed by first developing a “surface” of battery parameter values for each battery temperature considered. Each surface was then fit with a 5th order polynomial with respect to both the battery SOC and current level. The resulting parameter maps were found to be consistent with the experimental data, providing a smooth transition between battery operating points, and being consistent with the expected behavior typically exhibited by equivalent circuit battery model parameters (such as a growth in internal resistance due to a higher charging current) . Furthermore, the battery is not expected to operate outside of the SOC range considered during calibration, making smoothing of the battery parameters via curve-fitting a reasonable approach. Figures 21, 22, and 23 illustrate the smoothed calibration results for $R, R_0,$ and C_0 (respectively) at a temperature of $40^\circ C$.

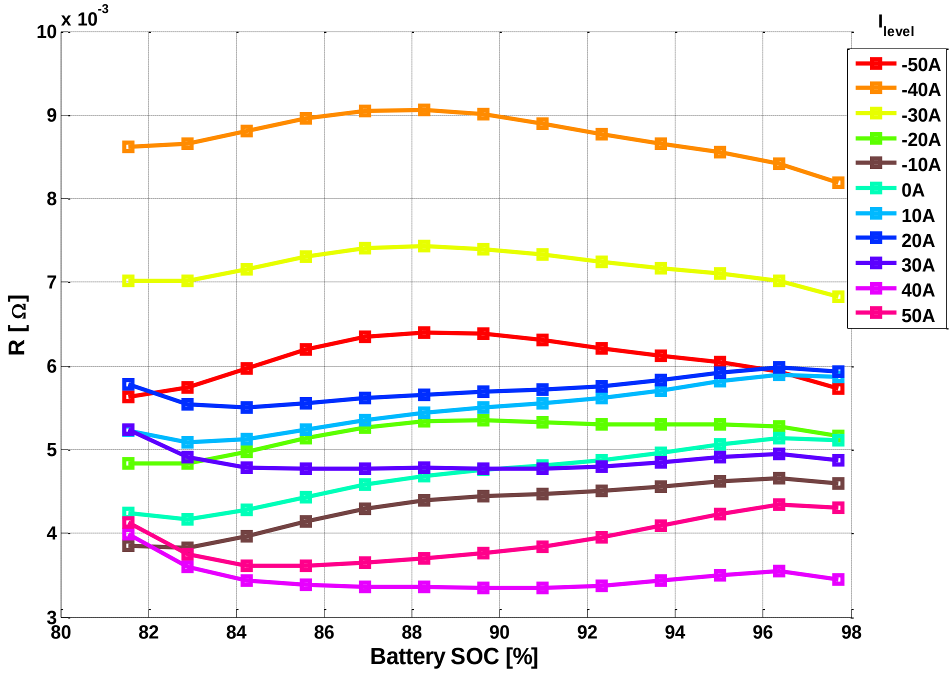

Figure 21: Battery Model Parameter Identification: Parameter R for 40 C

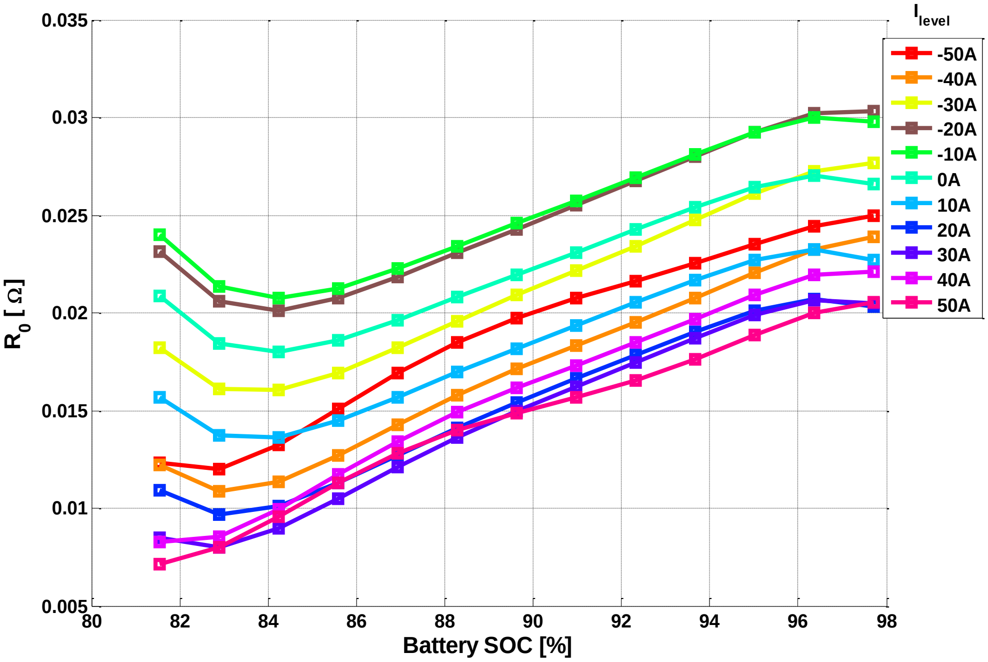

Figure 22: Battery Model Parameter Identification: Parameter R_0 for 40 C

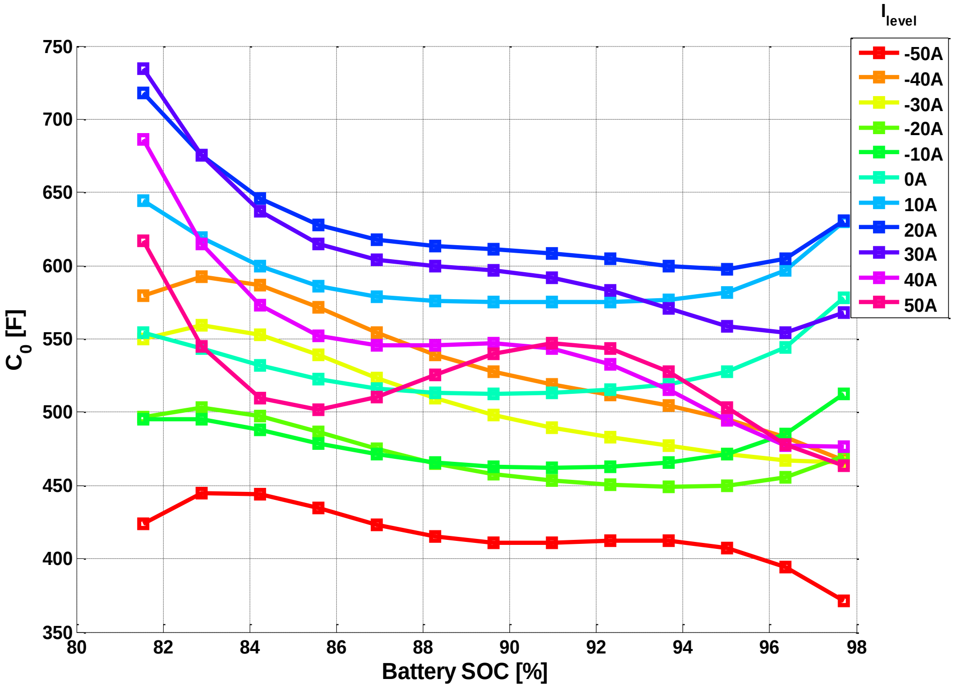

Figure 23: Battery Model Parameter Identification: Parameter C_0 for 40 C

From Figures 21 and 22, the battery internal resistances (R, R_0) are observed to increase overall as the battery current changes directions from discharging to charging. This is to be expected, as the charge acceptance of the battery is expected to decrease as charging currents of larger and larger magnitudes are imposed. As the battery state of charge is increased towards 100%, the internal resistance (R) is also expected to increase significantly. However, this behavior is not depicted in Figure 21 due to the SOC only achieving a value of approximately 98%. Of particular interest in this experiment is the dependence of the battery parameters on the temperature (T_{bat}), as the temperature of the air and mounting brackets surrounding an automotive battery are expected to fluctuate heavily depending on the particular testing environment. Figure 24 illustrates the temperature-dependence of the battery internal resistance for $I_{level} = 50A$. Note that not all constant-SOC lines are plotted to avoid overcrowding of the figure.

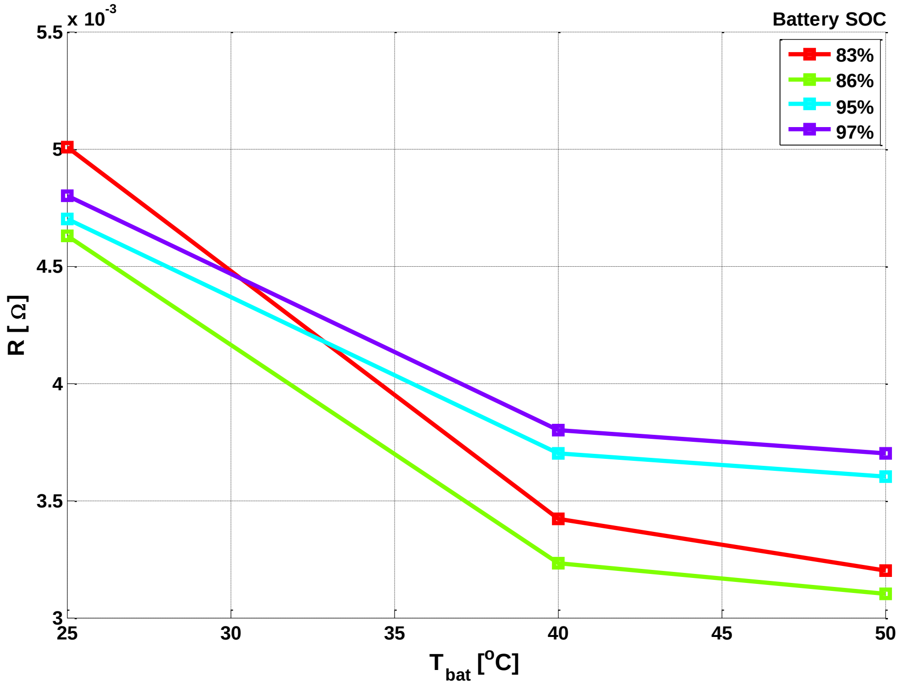

Figure 24: R-values as a function of Battery Temperature

The internal resistance of the battery exhibits an approximately inverse relation with the battery temperature. While Figure 24 only depicts this relationship for a single current level, a large portion of the internal resistance map is consistent with these findings. This behavior can be attributed to the well-known Arrhenius Equation:

$$k = Ae^{\frac{-E_a}{RT}} \tag{11}$$

Where k is the rate constant of the chemical reaction, E_a is the activation energy, R is the universal gas constant, and T is the absolute temperature in degrees Kelvin.

According to Equation 11, as the temperature increases, the rates of the chemical reactions occurring within the battery increase significantly. This facilitates faster current transport, translating to a lower internal resistance. With the internal resistance maps largely in agreement with this, confidence in the calibration of the battery parameters may be achieved.

2.3.3: Chrysler EVR Controller Model

As the motivation for this project is to demonstrate the ability of a supervisory controller to provide improved fuel economy through the intelligent management of the vehicle electrical system, some baseline for comparison is necessary. The control strategy currently employed in the vehicle is termed the Electronic-Voltage Regulator (EVR). The EVR compares some temperature-dependent reference battery voltage with the immediate battery voltage, and attempts to minimize the difference between the two by commanding the alternator duty cycle. Given this information, a model of the EVR is then developed and tuned to agree with experimental data. A block diagram depicting the general underlying logic of the EVR controller may be studied in Figure 25.

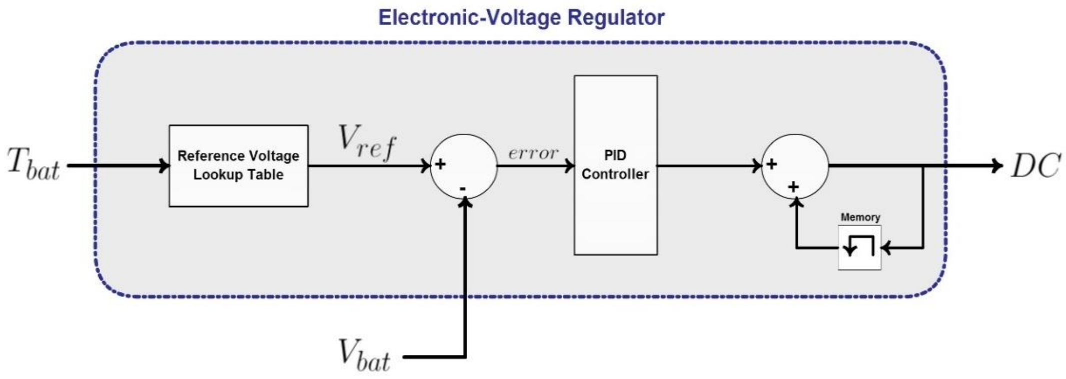

Figure 25: Electronic-Voltage Regulator Block Diagram

Calibration of the EVR was achieved through trial-and-error in regards to both the reference-voltage lookup table and the PID-controller parameters.

2.3.4: Vehicle Electrical System Model Validation

In order to ensure the validity of the alternator and battery models in a standalone environment and guarantee compatibility between all sub-components of the vehicle electrical system, each VES sub-model is first validated independently with experimental data collected via the ETAS ES1000. The entire model is then validated with the same on-road experimental data. This experimental data is collected over a wide range of operating conditions by subjecting the vehicle to an on-road driving cycle with the air-conditioning (A/C) system switched to automatic to create a variable load current profile. The vehicle velocity, engine torque and speed, and vehicle electrical load are all depicted for this drive cycle in Figure 26. Take note that a significant portion of this experimental data was collected on the highway.

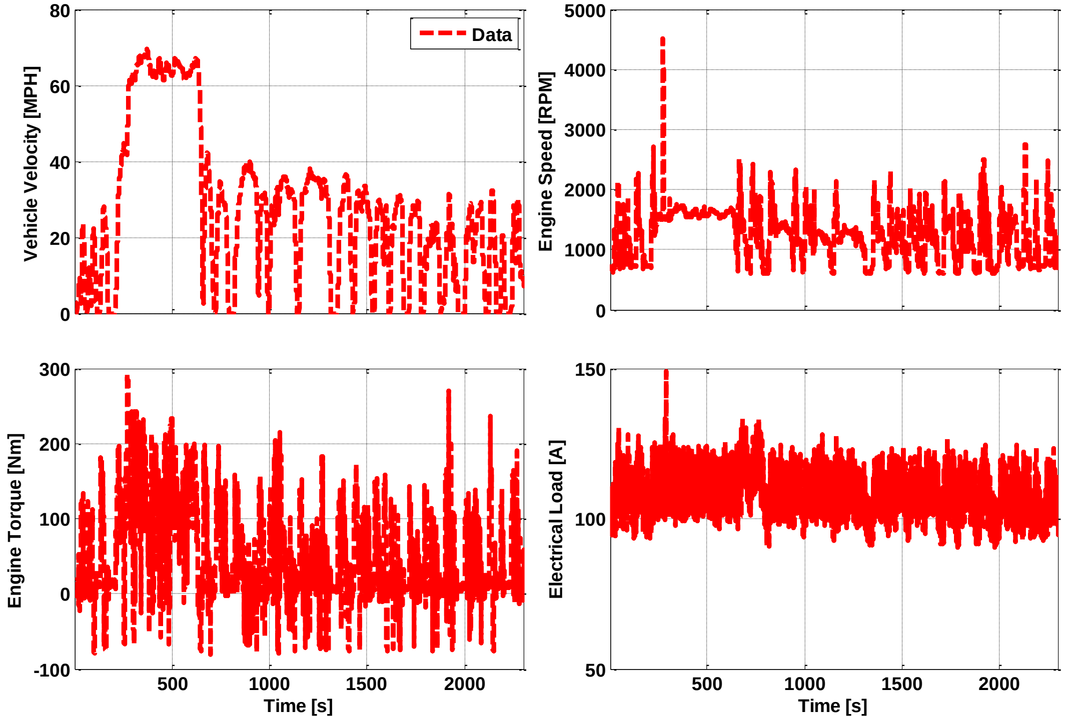

Figure 26: VES Validation Experimental Data.

The standalone alternator model results are compared with the experimental data in Figure 27. The RMS error over the entire timespan of the on-road cycle is 5.1 A, or 4.5%.

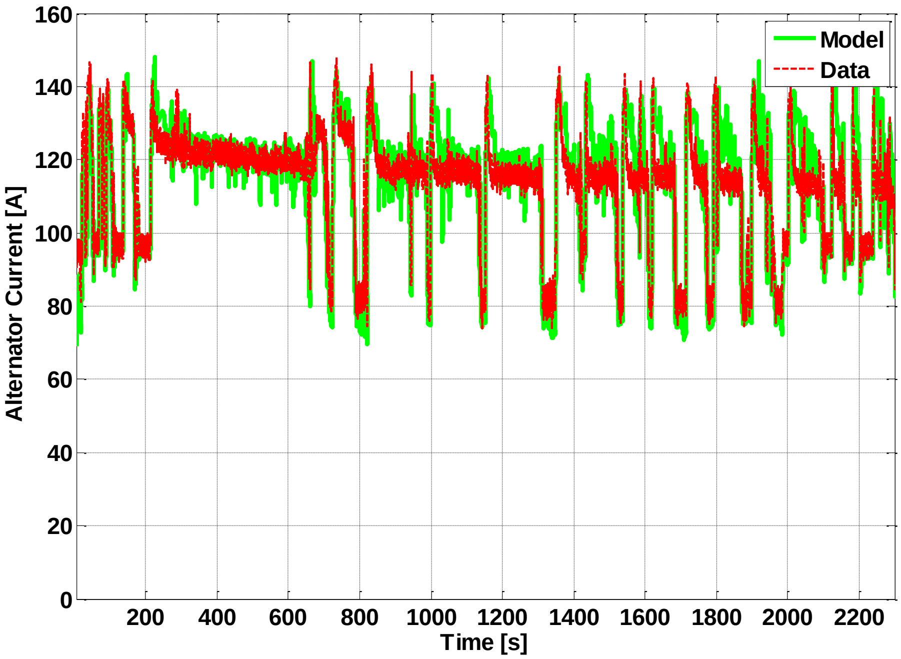

Figure 27: Results of Standalone Alternator Model Validation.

In order to ensure the legitimacy of the battery parameter maps outside of the range of calibration, a verification of the standalone battery model is performed. In conjunction with the verification of the alternator model, experimental data extracted from the on-road drive cycle with the A/C set to automatic mode is used to mimic realistic driving conditions. Figure 28 illustrates the electrical current input to the battery model, as well as both the experimental and simulated battery voltages. The RMS error over the entire drive cycle is 0.25 V, or 1.8%. Given the wide range of operating conditions that the vehicle is subjected to for this on-road driving cycle (i.e. city and highway driving, A/C and radiator fan switching on/off, etc…) this error may be considered acceptable.

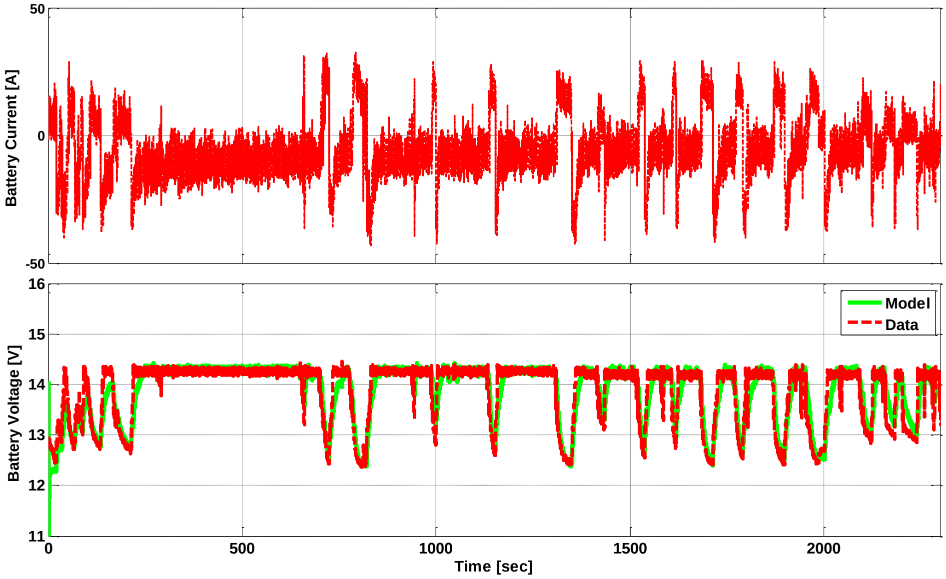

Figure 28: Results of Standalone Battery Model Validation.

Figures 29 and 30 depict the experimental battery voltage and alternator current (respectively) alongside the simulation results for the assembled vehicle electrical system model. Note that the inaccuracies of each sub-model amplify as the entire vehicle electrical system model is assembled. The RMS error of the battery voltage is 0.26 Volts, whereas the RMS error of the alternator current is 8.4 A.

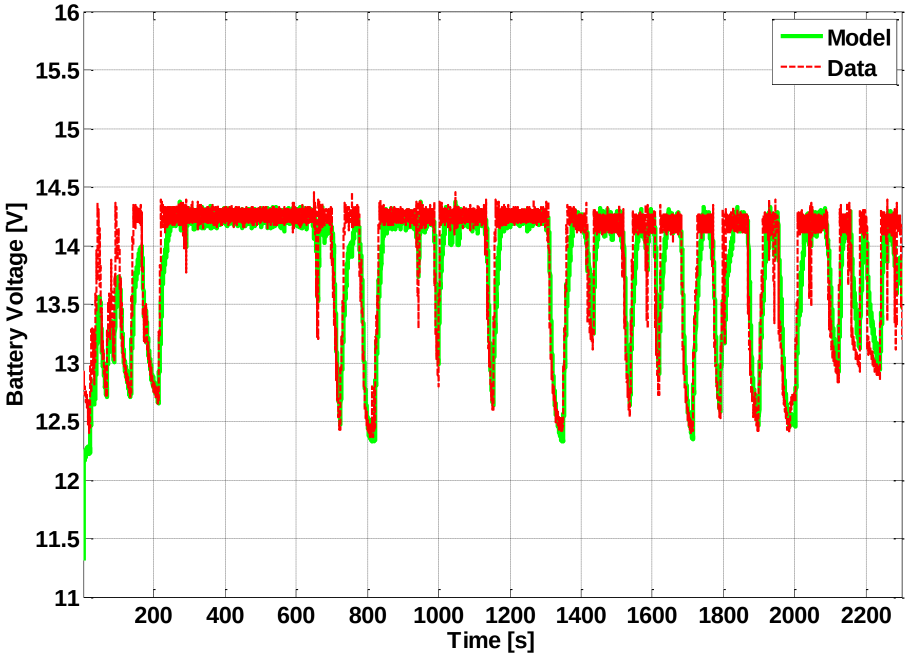

Figure 29: Full Vehicle Electrical System Validation: Battery Voltage.

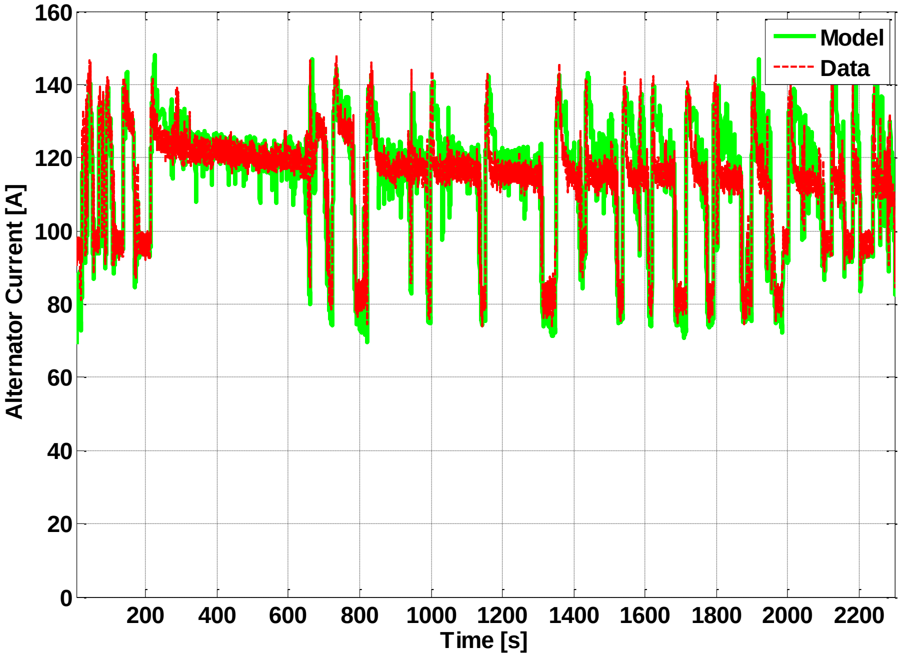

Figure 30: Full Vehicle Electrical System Validation: Alternator Current.

The increase in the overall predictive error of the electrical system model, and in particular the alternator sub-model, is more than likely due to the inaccuracies of each subsystem compounding upon one another. The model calibration procedures utilized for developing the alternator model, which obtains quasi-static steady-state data points, may be partially to blame for these inaccuracies. A design of experiment which is able to take into account the dynamics of the alternator may yield a more accurate VES model. Referencing [31], a mean-value approach may be taken towards alternator modeling which includes lumped inductances and a bridge rectifier circuit and takes into account the fast dynamics of the alternator, and results in a very good match with experimental data over a wide range of operating conditions. However, given that the fast dynamics of the vehicle electrical system are not of crucial importance when evaluating cumulative vehicle fuel consumption over an extended period of time such as a drive cycle, this error is acceptable for the purposes of developing the energy supervisory controller.

As an investigation into the effects of the VES model inaccuracies, the cumulative energy error of the battery over the drive cycle under consideration is studied. This is achieved through simply taking the integral of the product of the battery voltage and current over the entire drive cycle for both the experimental and model data sets. The results of the accumulated energy within the battery, for both the model and experimental data, are very similar and are summarized in Table 3.

Table 3: Impact of VES Model Inaccuracies on Accumulated Battery Energy

Data Source	$\boldsymbol{E_{bat}}$ **Accumulated (kWh)**
Model	-0.07
Experimental	-0.06

Chapter 3: Application of Optimal Control Theory to the Energy Management of a Vehicle Electrical System

An accurate baseline controller, the Electronic Voltage Regulator, for evaluating the performance of an energy management control strategy has been developed in Chapter 2. While fuel economy improvements upon this baseline controller may be quantified, it is necessary to establish an understanding of the maximum possible fuel savings that may be recognized. Optimal control theory allows for a relatively straightforward solution to this objective by addressing the issue of finding the control input trajectory which optimizes a specific performance criterion [32], i.e. minimization of the cumulative vehicle fuel consumption. Therefore, the application of optimal control theory to the energy management of a vehicle electrical system provides a useful benchmarking tool to evaluate the efficacy and performance of implementable, sub-optimal control strategies. The present chapter investigates the potential benefits of optimal control theory, as applied to the vehicle electrical system.

Chapter 3 begins with a discussion of the optimal control problem and objectives. An in-depth analysis of optimal control over a single drive cycle, as applied to the VES, is then performed. The robustness of the control strategy is then investigated through various sensitivity analyses. Finally, this analysis is expanded to numerous scenarios, and the overall behavior of the optimal control strategy is characterized.

Section 3.1: Optimal Control Objectives and Methodology

The control problem, specific to the vehicle electrical system under investigation, is first defined in this section. Electrical system constraints are then discussed, followed by an application-specific derivation of the selected optimal control solution.

3.1.1: Alternator-Battery Power Split Problem

The primary objective put forth is to improve the overall fuel economy of a vehicle through the development of a new electrical system control strategy. The currently employed control strategy, termed “Electronic-Voltage Regulation” (or EVR for short) maintains battery voltage at a predetermined value in order to ensure a full charge, only utilizing the battery when the alternator is incapable of providing the desired load. While this control strategy provides for reliable cold-cranking conditions, it is inherently inefficient for two reasons:

1) The charge acceptance of lead-acid batteries drops off considerably when fully charged, resulting in unnecessary system losses.
2) Holding the battery to a near-constant state of charge negates many of its potential benefits as a dynamic, on-board energy storage system.

The development of a less conservative control strategy (with respect to the battery’s cold cranking ability), which can exploit the battery’s ability to function as a reversible energy storage device, may therefore prove beneficial to vehicle fuel economy. Such control strategies are commonplace in hybrid electric vehicles, being utilized to optimize the “power-split” between the engine and electric motor. The overall architecture of a conventional automotive electrical system is quite similar to that of a mild, parallel HEV. It is therefore reasonable to develop an electrical system control strategy for use in a conventional automobile centered around a similar “current-split” principle. A block diagram depicting the vehicle electrical system of interest, and its interactions with the engine, may be observed in Figure 31.

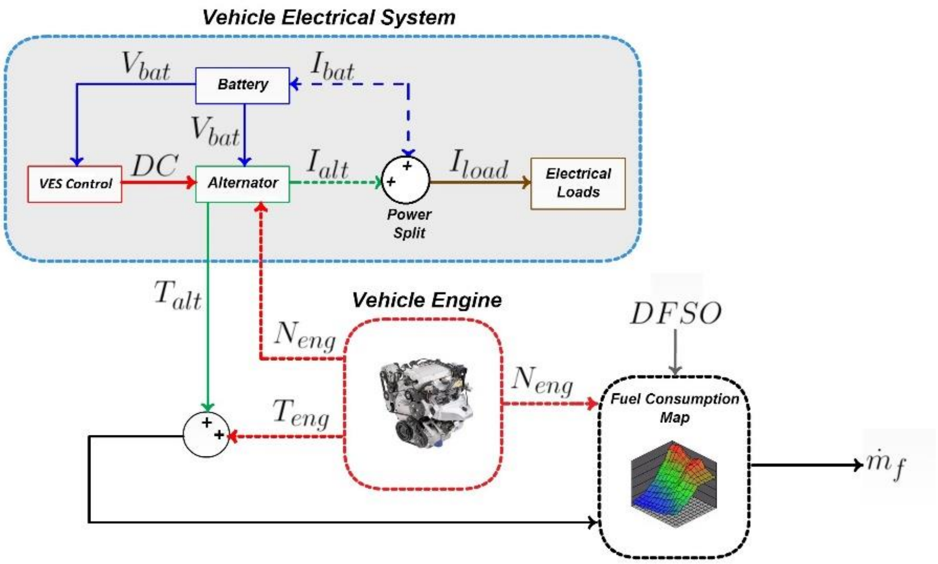

Figure 31: Vehicle Electrical System Schematic

Take note that T_{eng} refers to the baseline engine torque, which is equivalent to the engine brake torque minus the torque required to drive the vehicle alternator. During data acquisition, however, it is impossible to decouple these two torques from one another, as the vehicle ECU calculates the approximate net engine torque. Therefore, in order to approximate the baseline engine torque as closely as possible, the vehicle electrical loads (and therefore the alternator torque) are minimized during all experimental data collection discussed in Chapter 3. The effects of the alternator torque on the calculated net engine torque therefore result in a small, near-constant offset error which may be neglected for the purposes of the analyses performed.

Referencing Figure 31, it can be seen how the current-split is directly tied in to the vehicle fuel consumption. Determining the optimal current-split between the battery and alternator, via the alternator duty-cycle command, is therefore the control problem of interest. The optimal current-split is therefore defined as the control command which fulfills the following criteria:

1) Provides the desired current to the electrical loads at any given point in time;
2) Splits the current demand between the battery and alternator so to minimize energy consumption in relation with the operating conditions of the system;
3) Satisfies a set of constraints on battery and electrical system performance.

The latter of these requirements will be evaluated in the following section.

3.1.2: Constraints of the Vehicle Electrical System

Constraints on the vehicle electrical system, administered by the control strategy, are put in place in order to ensure driver comfort and safety and avoid damaging the alternator and coupled electrical loads, while the detrimental battery-aging effects that accompany rapid current and voltage swings are regulated and kept to a minimum. The exact form of these constraints is explicitly laid out as follows:

$$V_{min} \leq V_{bat}(t) \leq V_{max} \tag{12}$$

$$I_{bat,min} \leq I_{bat}(t) \leq I_{bat,max} \tag{13}$$

$$I_{alt}(t) \leq I_{alt,max} \tag{14}$$

$$\left|\frac{d}{dt}V(t)\right| \leq \dot{V}_{max} \tag{15}$$

Where constraint 1 represents the minimum and maximum allowable battery voltages, and ensures that all electrical loads in the vehicle remain operating within specification (ex. cabin lights and blowers maintaining acceptable operating voltages). Constraint 2 represents the minimum and maximum allowable battery currents, and is enacted for similar reasons. Constraint 3 represents the maximum possible alternator current (which is dependent upon operating conditions), and constraint 4 represents the maximum allowable battery voltage time rate of change. The implementation of these constraints is carried out by means of defining a current-split array ($\boldsymbol{\gamma}$) which, in conjunction with the maximum alternator current value, provides a discrete representation of all possible current-split options within the vehicle electrical system. The derivation of the current-split procedure is laid out below. From this point forward, all variables in bold font exist as vectors.

$$\boldsymbol{\gamma} = [0, 1] \in \mathbb{R}^n \tag{16}$$

$$\boldsymbol{I_{alt}} = \boldsymbol{\gamma} \cdot I_{alt,max} \tag{17}$$

$$\boldsymbol{I_{bat}} = I_{loads}(t) - \boldsymbol{I_{alt}} \tag{18}$$

Where $I_{loads}(t)$ represents the electrical load demand in amperes. The resultant battery current array is passed through a 0th-order simplified battery model having the ability to approximate future battery voltage, given the battery's present state and future current level. Any battery current values that result in violations of the constraints can then be filtered out before the remaining suitable candidates are passed on to the next step in the control process. Figure 32 graphically depicts the general structure of how the system constraints are implemented in the energy management strategy.

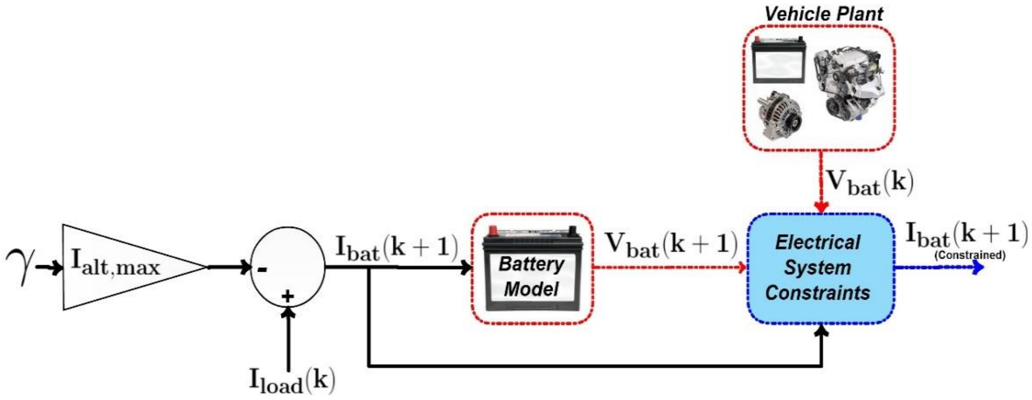

Figure 32: Implementation of Vehicle Electrical System Constraints

3.1.3: Optimal Control with Pontryagin's Minimum Principle

The desired outcome of the energy management strategy under consideration is the minimization of cumulative vehicle fuel consumption over a given drive cycle while sustaining battery charge. To this extent, a global optimal control problem may be formulated. An integral cost function, *J,* is first defined as follows:

$$J = \int_{t_0}^{t_f} \dot{m}_{fuel} \, dt \tag{19}$$

Mathematically speaking, the optimal control solution $u^*(t)$ may be described as the control trajectory which minimizes this integral cost function. As may be observed in Figure 32, the fuel mass flow rate depends in part on the alternator torque, which may ultimately be expressed as a function of the battery state of charge *x(t)* and battery power *u(t)*. Therefore, the following may be stated:

$$\dot{m}_{fuel} = L(x(t), u(t), t) \Rightarrow J = \int_{t_0}^{t_f} L(x, u, t) \, dt \tag{20}$$

The evolution of the vehicle electrical system in time may be described by a differential equation which relates the battery SOC to the battery power:

$$\frac{d}{dt} x(t) = f(x(t), u(t), t) = -\frac{I_{bat}(t)}{3600 \cdot Ah_{nom}} \;\; ; \;\; \forall t \in [t_0, t_f] \tag{21}$$

A negative current value signifies charging. In order to utilize optimal control theory, it is necessary to restructure Equation 21 such that the time rate of change of the battery state of charge is explicitly dependent upon the battery state (*SOC*) and control input (P_{bat}). This may be performed by analyzing the simplified battery model, featured in Figure 33 and referenced in Section 3.1.2.

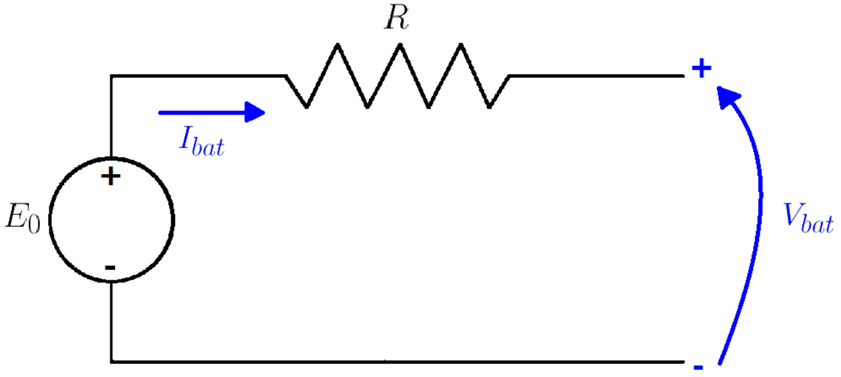

Figure 33: 0th-order Battery Model

$$V_{bat}(t) = E_0 - RI_{bat}(t) \tag{22}$$

$$P_{bt}(t) = V_{bat}(t) \cdot I_{bat}(t) \tag{23}$$

$$I_{bat}(t) = \frac{E_0 - V_{bat}(t)}{R} \tag{24}$$

By substituting Equation 23 into Equation 22, and recalling that both the open-circuit voltage and internal resistance are functions of the battery state of charge, the battery voltage can be expressed as an explicit function of the state and control variables. The resulting equation may then be plugged into Equation 24, which allows for the electrical system dynamics to be rewritten as follows:

$$\frac{d}{dt}x(t) = -\frac{1}{3600 \cdot Ah_{nom}} \cdot \frac{E_0 - \sqrt{E_0^2 - 4RP_{bat}(t)}}{2R} = -\frac{\varphi(x,u,t)}{3600 \cdot Ah_{nom}} \tag{25}$$

Where $\varphi(x,u,t) = I_{bat}(t)$.

Subject to the system constraints discussed in Section 3.1.2, as well as:

$$x(t_0) = x_0 \tag{26}$$

$$x(t_f) = x_f = x_0 \tag{27}$$

$$x_{min} \le x(t) \le x_{max} \tag{28}$$

Due to the constrained nature of the optimization problem at hand, Pontryagin's Minimum Principle proves particularly useful and may be utilized in order to account for both the upper and lower bounds on the battery state of charge, as well as the required charge-sustaining behavior of the battery. The global optimal control problem can then be recast into a local optimization problem. This is achieved by introducing a time-varying Lagrange multiplier, or co-state variable, λ, alongside a boundary penalty function, or inequality constraint, μ, which arises from the Karush-Kuhn-Tucker conditions. An extended Hamiltonian function, *H*, may then be developed such that the following necessary conditions are satisfied:

$$H(x^*, u^*, \lambda^*, \mu^*, t) \le H(x, u, \lambda, \mu, t) \;\; ; \;\; \forall u \ne u^* \tag{29}$$

$$x^*(t_f) = x^*(t_0) = x_0 \tag{30}$$

$$\dot{x}^*(t) = \nabla_\lambda H|^* \tag{31}$$

$$\dot{\lambda}^*(t) = \nabla_x H|^* \tag{32}$$

Where the Hamiltonian function is defined as follows:

$$H(x, u, \lambda, \mu, t) = \dot{m}_{fuel} - [\lambda(t) + \mu(t)] \cdot \frac{\varphi(x, u, t)}{3600 \cdot Ah_{nom}} \tag{33}$$

The objective being to minimize the Hamiltonian function at each time step. In order to apply this optimization method to the vehicle electrical system, analytical expressions for both the co-state variable λ and the boundary function μ are developed as follows:

$$\dot{\lambda}(t) = -\nabla_x \overline{H} = -[\lambda(t) + \mu(t)] \cdot \frac{d}{dx}\left(-\frac{\varphi(x,u,t)}{3600 \cdot Ah_{nom}}\right) \tag{34}$$

$$\mu(t) = \begin{cases} \mu_l & SOC \geq SOC_{max} \\ -\mu_l & SOC \leq SOC_{min} \\ 0 & else \end{cases} \quad ; \quad (\mu_l \geq 0) \tag{35}$$

The computationally intensive parameters, φ and $\frac{d\varphi}{dx}$, may be solved off-line and mapped vs. the battery SOC (state), power (input), and temperature to allow for rapid calculation of the co-state dynamics in real-time. These maps are shown in Figure 34 for a temperature of 40 deg. C.

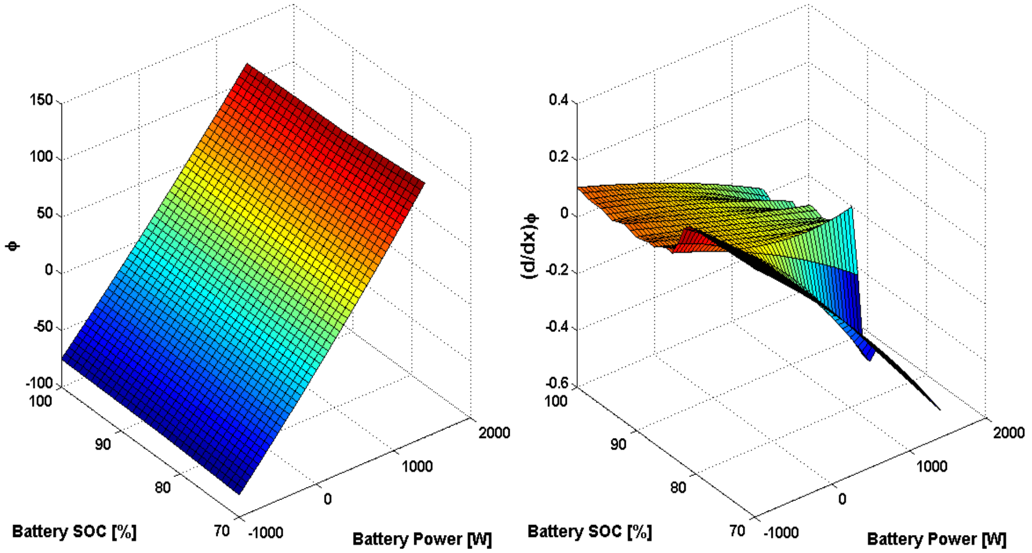

Figure 34: Co-state Dynamics Lookup Tables at 40 deg. C

The minimum (optimal) value of the Hamiltonian may now be located. For each discrete time step that the Pontryagin control strategy is triggered, the duty cycle command which results in this minimum Hamiltonian is fed back to the alternator, completing the closed-loop control circuit. The optimal control problem, now fully defined, may be summarized according to Figure 35. Take note of the contrast between the inputs of the inverted alternator maps in Figure 35, and the alternator maps featured in Figure 16. The inverted maps monitor the battery voltage, engine speed, and the alternator current array, and output a corresponding duty-cycle and alternator torque array. This duty-cycle array is passed through an index function which monitors the position of the minimum Hamiltonian function, and outputs the corresponding duty-cycle command.

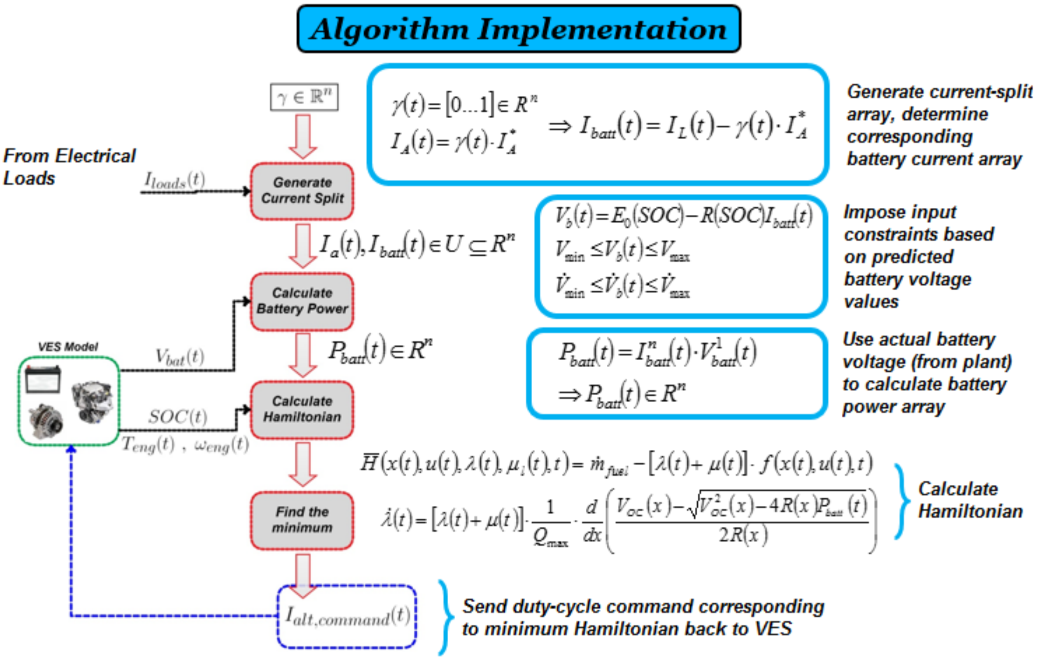

Figure 35: Structure of Pontryagin's Minimum Principle Control Strategy

The values of the electrical system constraints implemented into the control strategy, as well as the limitations on the operating conditions of the battery SOC, are defined in Table 4.

Table 4: Vehicle Electrical System Constraints

Parameter	Value	Description
$\boldsymbol{V_{min}}$	11.5 V	Minimum battery voltage
$\boldsymbol{V_{max}}$	15 V	Maximum battery voltage
$\boldsymbol{\dot{V}_{max}}$	0.5 V/s	Maximum rate of change of battery voltage
$\boldsymbol{I_{bat,min}}$	-50 A	Minimum battery current
$\boldsymbol{I_{bat,max}}$	50 A	Maximum battery current
$\boldsymbol{I_{alt,max}}$	150 A	Maximum alternator current
$\boldsymbol{SOC_{min}}$	82 %	Minimum desired battery state of charge
$\boldsymbol{SOC_{max}}$	88 %	Maximum desired battery state of charge
$\boldsymbol{SOC_0}$	85 %	Initial value of battery state of charge

Section 3.2: Analysis of Pontryagin's Optimal Solution

In order to gather a comprehensive understanding of the general behavior of the vehicle electrical system and the resultant vehicle fuel consumption when subjected to optimal control conditions, the VES will be evaluated in-depth for a specific drive cycle and electrical load profile. The New European Driving Cycle (NEDC) is assessed in Section 3.2.2 due to its relatively smooth velocity profile, which aids in concisely illustrating the various physical behaviors which are characteristic of Pontryagin's Minimum Principle. The electrical load profile is set to a constant value of 57.5 A, approximating the average electrical load value of the Chrysler minivan over numerous NEDC dynamometer runs with the A/C set to automatic. This analysis is then expanded upon in Section 3.2.3 by performing numerous sensitivity studies in regards to the control parameters, allowing one to partially assess the feasibility of an adaptive, optimal-based implementable control strategy. A more broad analysis of the Pontryagin control strategy is performed in

Section 3.2.4, encompassing various combinations of drive cycles and constant electrical loads.

3.2.1: Influence of Parameters

Prior to any vehicle controller and plant behavioral analysis, the optimal control solution for a given velocity trace and electrical load must be located. The primary control parameter which dictates charge-sustaining behavior is the initial value of the co-state variable, λ_0. Therefore, by determining this value optimality may be ensured. An optimization algorithm consisting of sequential "sweeps" across all potential co-state candidates is implemented in order to locate the optimal value, λ_0^*. The algorithm first searches for the appropriate co-state interval which contains a charge-sustaining solution. Once this interval is determined, the search is refined and the procedure is repeated until an acceptable degree of error (in regards to the net change of battery state of charge) is achieved. A summary of the underlying structure of this algorithm is laid out in Figure 36. For all drive cycles and electrical load values considered, the initial specified range of the co-state variable $(-225 \leq \lambda_0 \leq 0)$ is sufficient and contains the optimal solution. Figure 37 graphically depicts the location of λ_0^* for the case of the New European Drive Cycle with the electrical load demand set to a constant 57.5A. The optimal initial co-state value for the particular scenario under consideration is determined in only two iterations and is equal to -56. The optimal boundary penalty function is relatively easy to calibrate in comparison; a significantly high value which prevents violation of the state constraints is sufficient, thus μ may be held to a value of 400 for all driving scenarios.

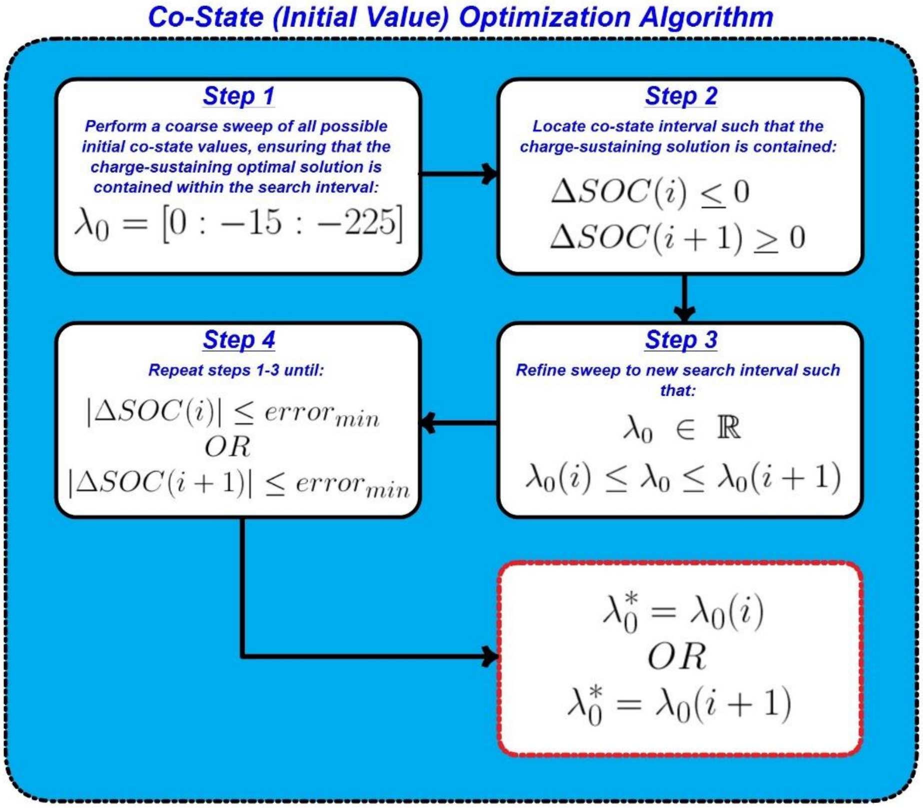

Perform a coarse sweep of all possible initial co-state values, ensuring that the charge-sustaining optimal solution is contained within the search interval:

$$\lambda_0 = [0 : -15 : -225]$$

Locate co-state interval such that the charge-sustaining solution is contained:

$$\Delta SOC(i) \leq 0$$
$$\Delta SOC(i+1) \geq 0$$

Refine sweep to new search interval such that:

$$\lambda_0 \in \mathbb{R}$$
$$\lambda_0(i) \leq \lambda_0 \leq \lambda_0(i+1)$$

Repeat steps 1-3 until:

$$|\Delta SOC(i)| \leq error_{min}$$
$$OR$$
$$|\Delta SOC(i+1)| \leq error_{min}$$

$$\lambda_0^* = \lambda_0(i)$$
$$OR$$
$$\lambda_0^* = \lambda_0(i+1)$$

Figure 36: Initial Co-state Variable Optimization Algorithm Outline

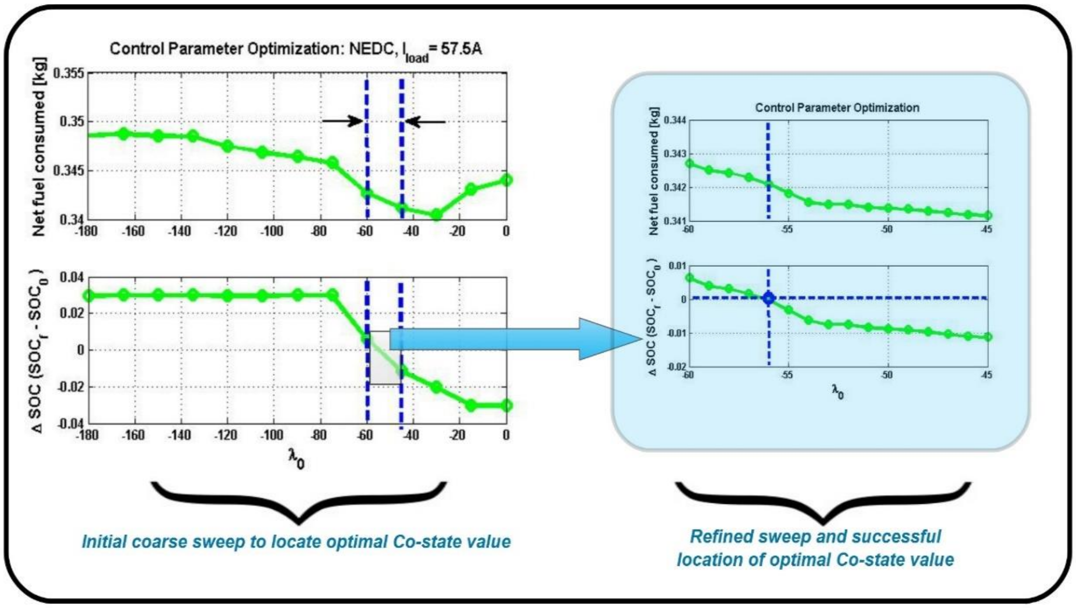

Initial coarse sweep to locate optimal Co-state value

Refined sweep and successful location of optimal Co-state value

Figure 37: Initial Co-state Variable Optimization for NEDC, $I_{loads} = 57.5A$

3.2.2: Case Study Results: New European Drive Cycle

The vehicle fuel economy and electrical system behavior, subjected to optimal control, are thoroughly investigated for a constant electrical load profile of 57.5A and the NEDC velocity profile. The vehicle velocity trace, engine speed and torque, and the electrical load may be observed in Figure 38.

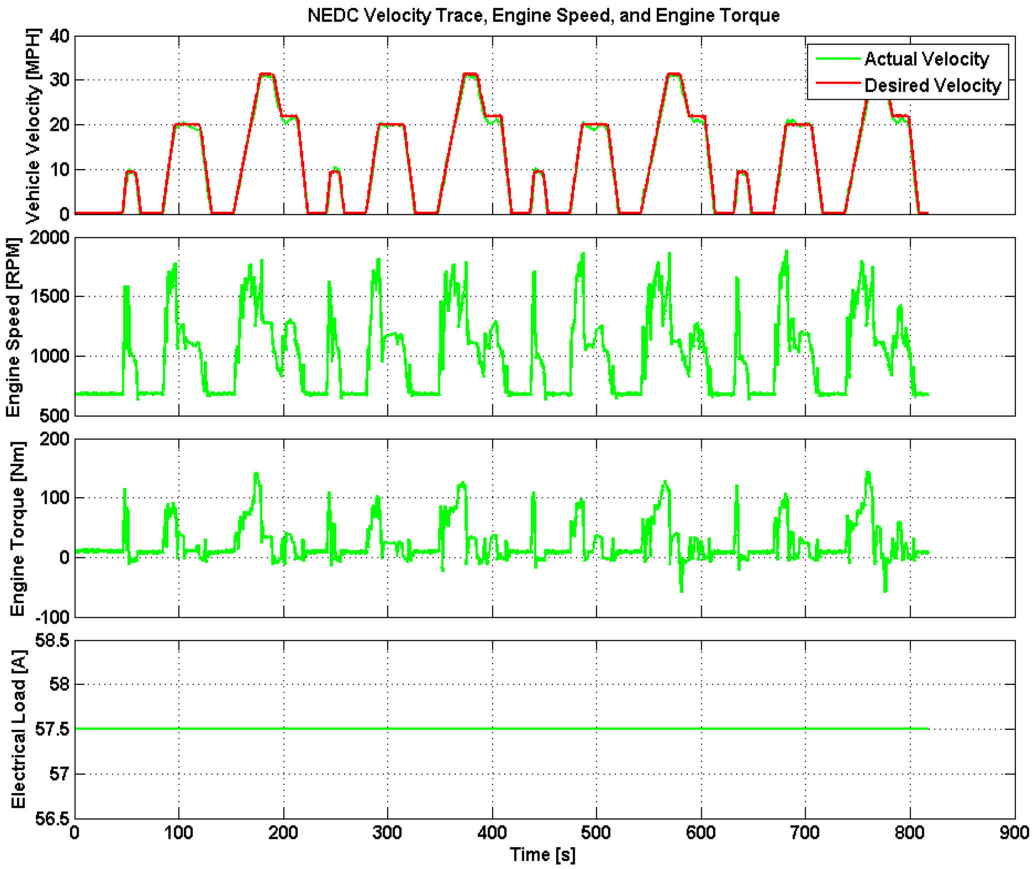

Figure 38: Optimal Control Case Study: New European Drive Cycle at 57.5A

As discussed in Section 3.2.1, and depicted in Figure 37, the optimal initial value of the co-state variable is equal to -56, which allows for charge-sustaining behavior over the drive cycle. The behavior of the vehicle electrical system, instantaneous fuel consumption, and co-state dynamics may be observed in Figure 39.

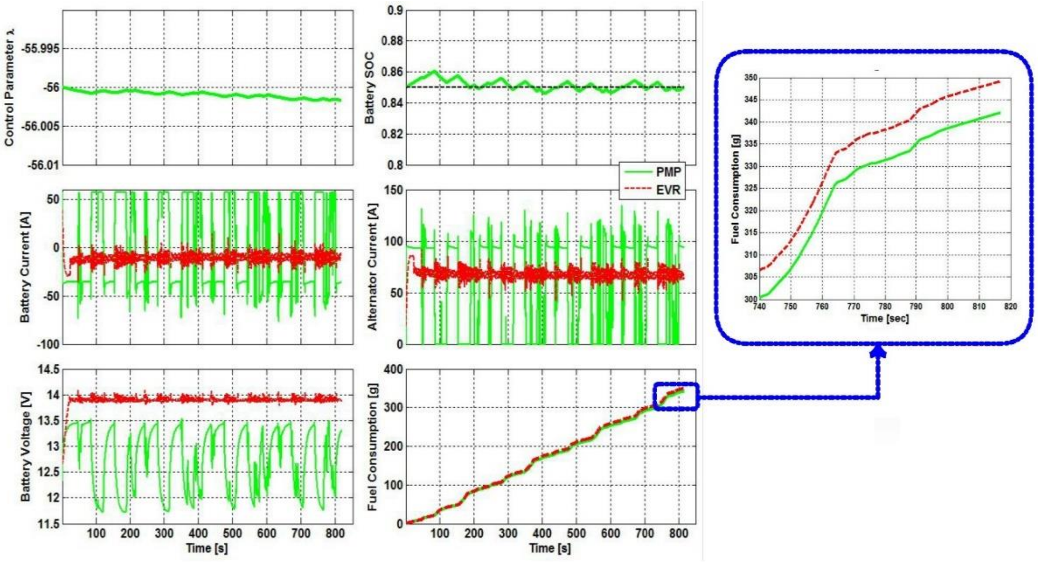

Figure 39: Results of Optimal Control Case Study

The co-state dynamics of the electrical load and driving schedule under consideration, depicted in the upper left corner of Figure 39, are essentially non-existent, varying by less than 0.01% over the entire length of the drive cycle. This trend is not isolated to this particular case study, and is rather observed in all scenarios considered (refer to Table 7). The variety of driving schedules and load profiles considered is discussed in greater detail in Section 3.2.4. The charge-sustaining behavior of the battery may be verified in the upper right corner of Figure 39, as the final state of charge is equal to the initial state of charge; 85%. This reference SOC was predetermined based on experience, and will be discussed in more depth in Section 3.2.3. The second row of plots in Figure 39 shows both the battery and alternator current profiles for the VES subjected to the baseline EVR controller and the PMP optimal control strategy. Of particular interest is the current commanded to and from the battery. While the EVR maintains a nominal charging current of approximately 15A in order to sustain the battery at the appropriate reference voltage, the PMP control strategy allows for the battery to be used as a dynamic energy storage device, with current values ranging from approximately -65A to 50A. The primary driver for these fluctuations between positive and negative current may be observed in Figure 40.

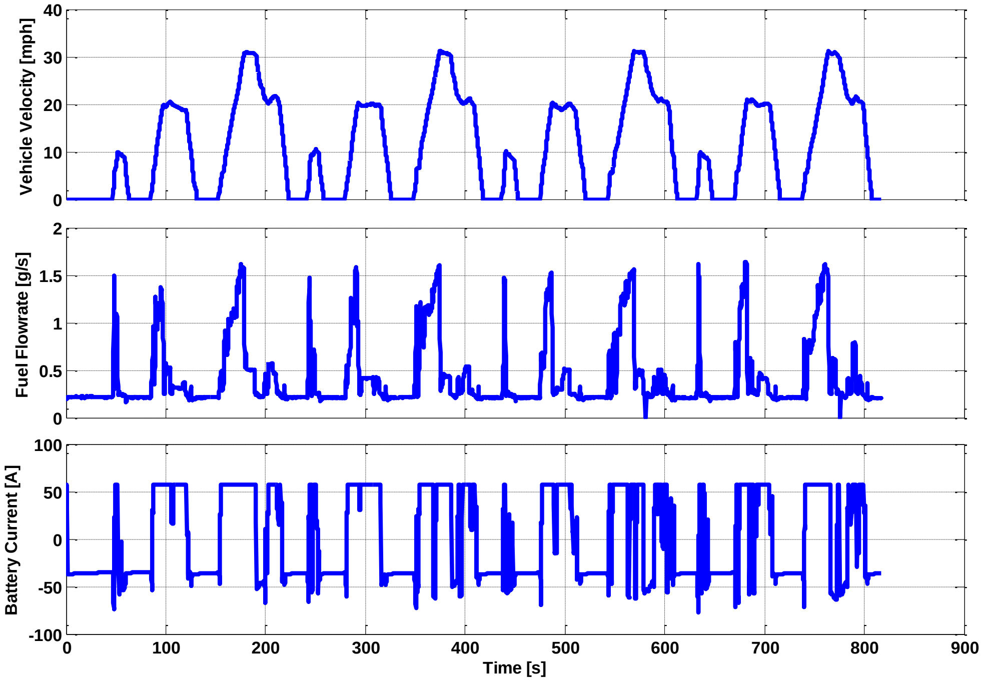

Figure 40: Optimal Control Case Study: Cause of Battery Current Fluctuations

An increase in the vehicle’s instantaneous fuel mass flow rate results in an increase in the battery current, corresponding to a battery discharge event. Keeping in mind Equation 33, the underlying reasons for this are evident. As the instantaneous fuel consumption of the vehicle increases, the apparent value of the battery energy imposed by the co-state variable diminishes in comparison. This translates to a de-weighting of the chemical energy contained within the automotive battery, ultimately resulting in battery discharge. As the fuel mass flow rate begins to drop off, the influence of the co-state variable increases, resulting in a battery charging event. It is interesting to compare both the battery current and vehicle velocity profiles; heavy acceleration events are accompanied by electrical assistance from the battery (as supplied to the loads), whereas coasting and braking events are associated with battery charging. This type of behavior is quite similar to regenerative braking schemes, where inertial energy otherwise lost to the atmosphere via an automobile's braking system may be recuperated by an electric machine. The lower left plot in Figure 40, which shows the battery voltage of the VES subjected to the EVR and PMP, assists in illustrating the dynamic behavior of the optimally controlled electrical system, and the importance of the imposed system constraints. The lower right plot in Figure 40 compares the vehicle fuel consumption of the EVR and PMP control strategies. The cumulative difference in fuel consumption between both control strategies results in a 2.1% improvement in fuel economy with optimal control. Table 5 provides the details of the overall fuel economy benefits realized with optimal control.

Table 5: Optimal Control Case Study: Fuel Economy Improvement

Controller	Fuel Economy (mpg)
Chrysler EVR	19.1
Optimal Control	19.5
% Improvement	**2.1%**

3.2.3: Control Parameter Sensitivity Analyses

In order to determine the most suitable control parameters, evaluate the robustness of the control strategy, and develop an implementable VES control strategy adapted from optimal control theory, numerous sensitivity analyses are performed. These analyses are performed for the same driving schedule and electrical load profile considered in Section 3.2.2. First, an analysis focusing on the resilience of the VES and PMP controller to errors in the selection of the optimal initial condition for the co-state variable is performed. The effects of changing the reference battery state of charge on fuel economy and VES model behavior are then studied, followed by an investigation into the effects of modifying the electrical system constraints. Finally, as the PMP controller subjects the battery to much more rapid and higher magnitude current swings than does the EVR, the cumulative energy flux of the battery for the control scenario is evaluated.

The ability of the controller to cope with sub-optimal control parameters is imperative in developing any sort of implementable control strategy, as the online controller will never have knowledge of a given drive cycle and VES load profile beforehand and can therefore only estimate an, almost assuredly sub-optimal, co-state value. In order to study the effects of sub-optimal co-state values, the VES model (subjected to PMP control) is simulated with co-state values of +/-25% of the optimal solution. The results of this study are featured in Figure 41.

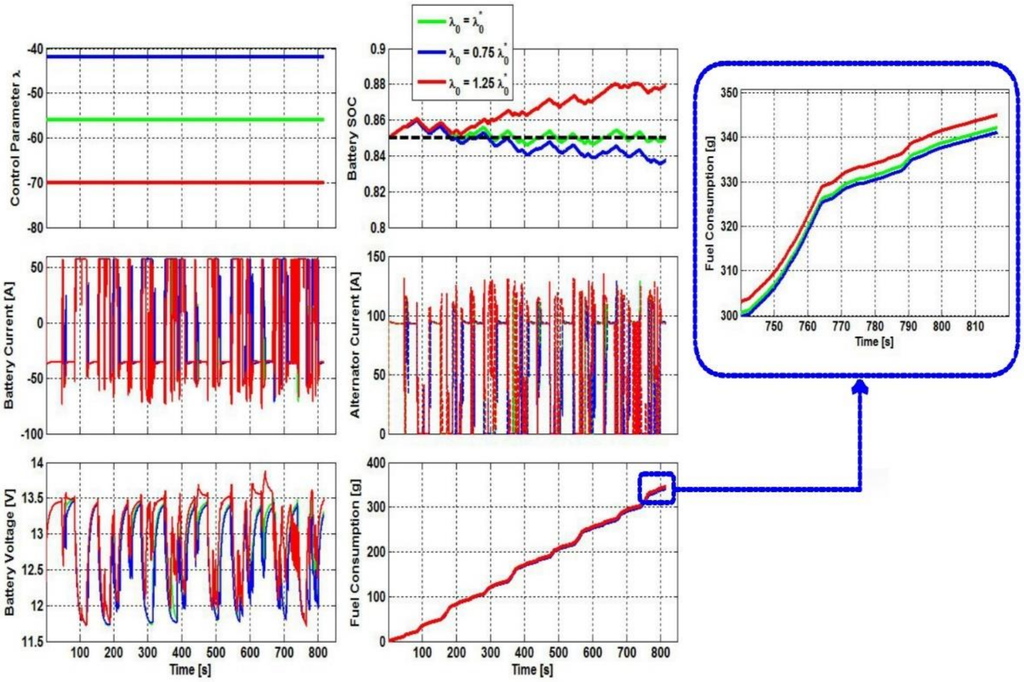

Figure 41: Co-State Sensitivity Analysis

Upon observation of the upper right plot in Figure 41, it is clear that underestimating the initial co-state value by 25% results in a discharge of approximately 1% battery SOC; only 1/3 of the way towards the lower threshold on the battery state of charge (82%). In contrast, by overestimating the initial co-state value by 25% the battery SOC drifts to the upper SOC threshold (88%) in approximately 700 seconds. If the co-state variable is overestimated, the duty-cycle command sent to the alternator is less likely to result in battery discharge. On the other hand, if the co-state variable is underestimated, battery charging events are less likely to occur as the value of the battery energy (determined via the co-state variable) is small in comparison with the value of the fuel energy. These results demonstrate that in order to develop any sort of implementable, real-time control strategy, there is a need for control adaptations which prevent the relatively slow battery SOC drift resulting from a sub-optimal initial co-state value.

The battery reference state of charge holds particular relevance in terms of control optimality as the battery should ideally operate around the reference SOC value for its entire lifespan. An effort should therefore be made to understand the impact of the reference state of charge on VES behavior and fuel economy. In order to do so, the reference battery SOC (and the corresponding upper and lower SOC thresholds) is held to three values: 85%, 90%, and 92.5%. The state of charge of the battery should not be increased much above 92.5% as the internal resistance of the battery increases dramatically at near 100% SOC values, therefore decreasing charge acceptance [23]. Likewise, the battery SOC should also not be decreased much below 80% due to both the concern of sufficient current draw for engine startup, and the risks inherent in lead-acid battery deep cycling (as discussed in Section 2.3.2)

The results of the reference state of charge analysis are depicted in Figure 42 below.

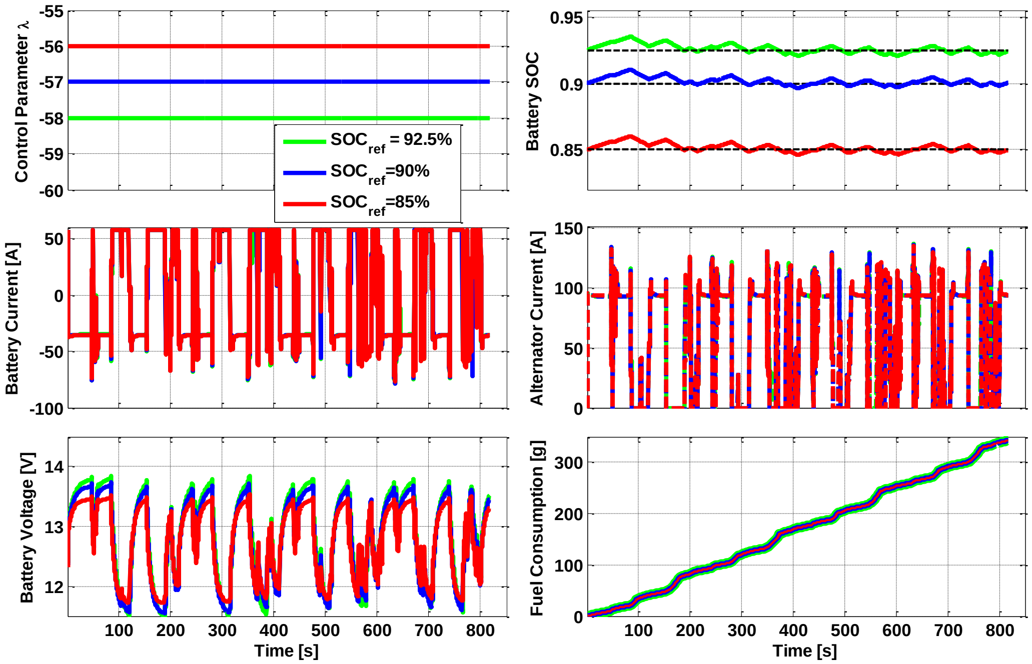

Figure 42: Reference Battery State of charge Sensitivity Analysis

It may be observed that only trivial differences exist, both in terms of VES behavior and the optimal co-state value, upon varying the reference state of charge and corresponding upper and lower SOC bounds. What is notable, however, is the slight increase in both the co-state variable and the magnitude of battery voltage swings as the reference SOC is increased. This may be explained by the fact that the battery model internal resistance increases as the battery state of charge increases from 85% to 92.5%. Despite battery operation being slightly less efficient as the reference SOC is increased (via ohmic losses in the equivalent circuit model), the corresponding decrease in fuel economy is negligible, equating to less than 0.01% of the total vehicle fuel consumption. The reference battery state of charge is therefore held to 85% in order to ensure that both deep-cycling and high SOC operation need not be of concern.

The system constraints of the PMP controller, as discussed in Section 3.1.2, restrict the dynamics of the vehicle electrical system in order to ensure customer comfort and safety, and avoid excessive wear and tear on the battery and alternator. Restricting the VES dynamics also translates to removing a number of potential candidates from the current-split array (γ), resulting in a departure from optimal control behavior. It is therefore necessary to balance both the reduction in VES aging, and the corresponding reduction in vehicle fuel economy, due to the imposition of the VES system constraints. Both the battery voltage constraints, V_{min} and V_{max}, and the battery voltage time rate of change constraint, $\dot{V}_{max}$, are initially non-existent, leaving the VES model behavior unconstrained. The constraints are then imposed in finite increments in order to study the corresponding reduction in the range of battery operating conditions and fuel economy. The results of the battery voltage constraint study are illustrated in Figures 43 and 44, whereas the results of the battery voltage time rate of change constraint study are depicted in Figures 45 and 46. Take note that as a 0^{th}-order battery model is used to predict the resultant battery voltage of all current-split candidates and filter out any candidates that result in constraint violations, error is introduced into the imposed constraints. Therefore, instead of specifying an exact value for the minimum and maximum allowable battery voltage and the maximum allowable battery voltage time rate of change, the percent reduction in battery operating range is specified. The VES behavior is evaluated for the unconstrained, 55%, and 62% constrained battery voltage scenarios, and is evaluated for the unconstrained, 38%, and 75% constrained battery voltage time rate of change scenarios.

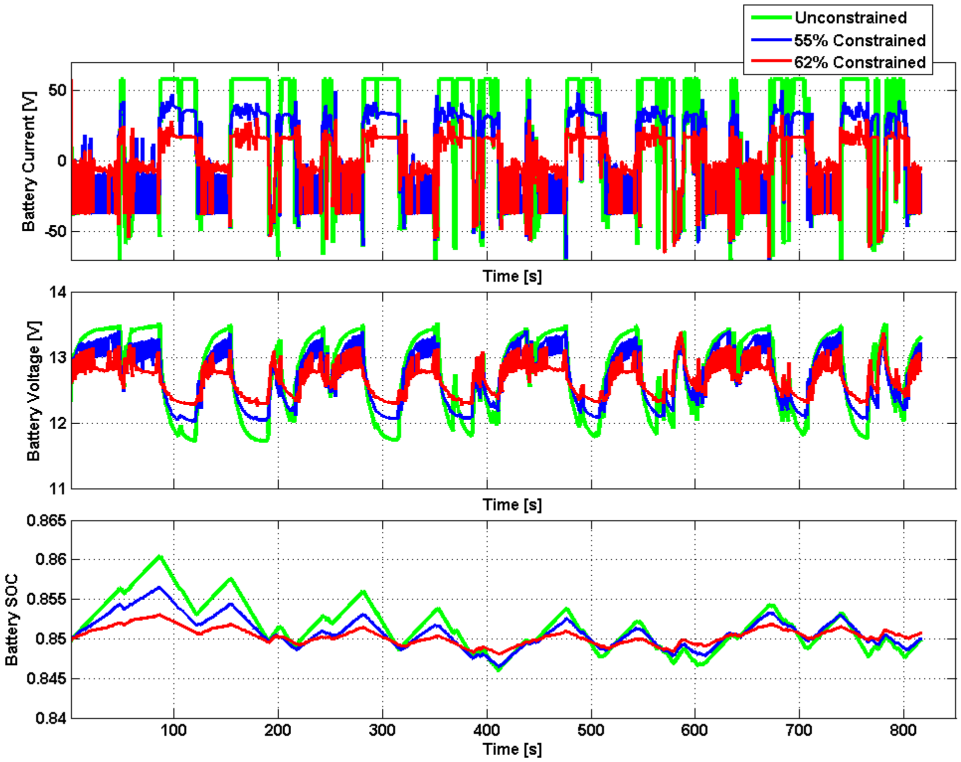

Figure 43: Battery Voltage Constraints Sensitivity Analysis

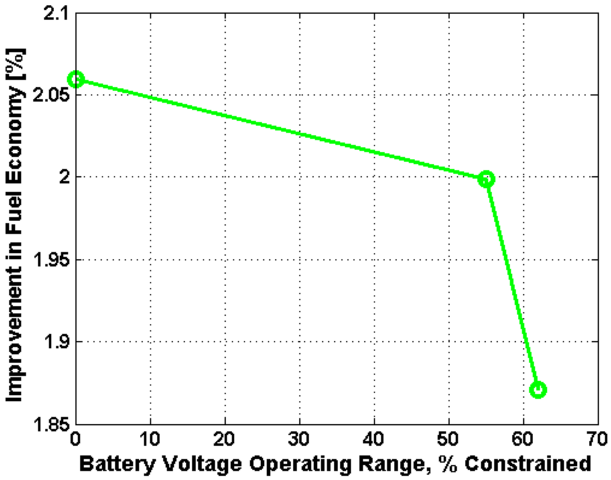

Figure 44: Battery Voltage Constraints Sensitivity Analysis, Fuel Economy

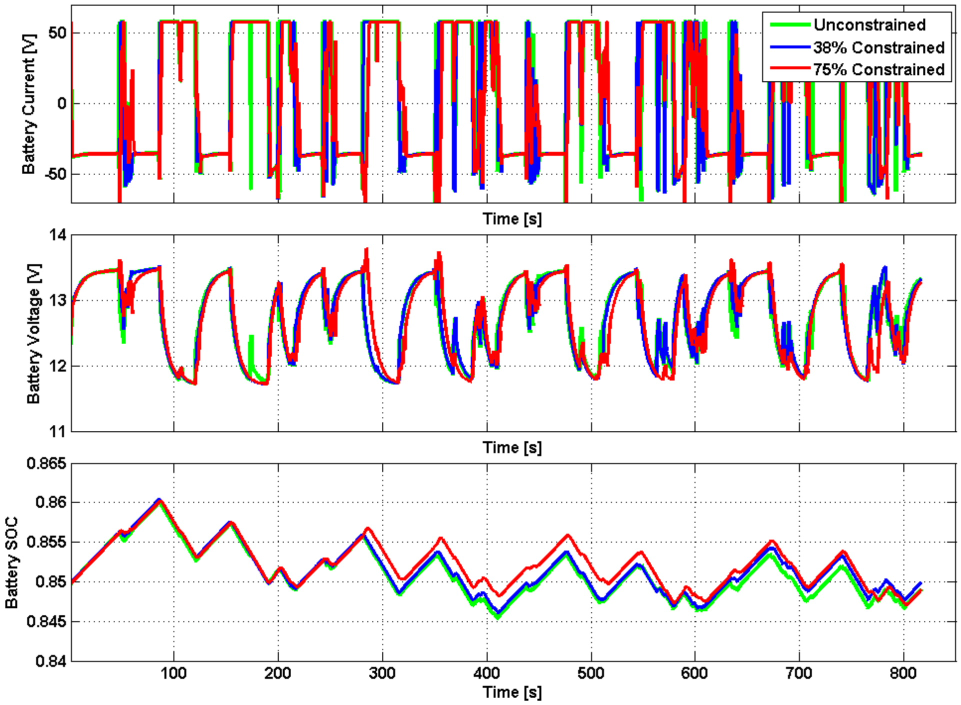

Figure 45: dV_{max} Constraints Sensitivity Analysis

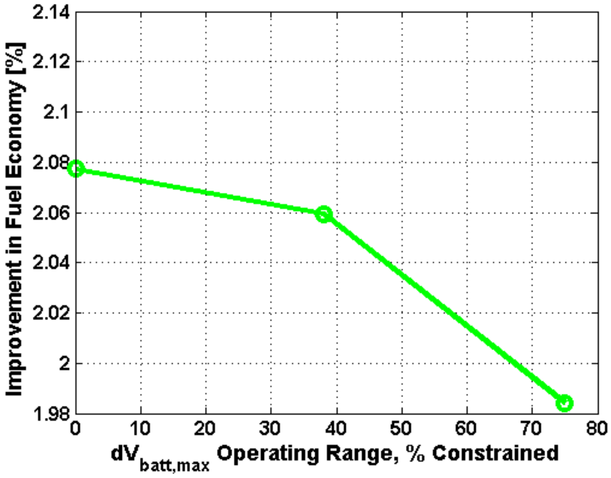

Figure 46: dV_{max} Constraints Sensitivity Analysis, Fuel Economy

Upon observation of Figures 43 and 44, it may be noted that the battery voltage constraints impact the behavior of the VES significantly, whereas restricting the time rate of change of the battery voltage does very little to change overall VES behavior. This is indicative of the PMP controller's behavior; while extended periods of battery charging and discharging (translating to a wide battery voltage operating range) lead to the optimal solution, the optimal magnitude of these charging and discharging events does not much surpass approximately 50A (translating to a limited dV_{max} value). The dV_{max} constraint, however, does provide the advantage of filtering out some of the bang-bang behavior which is characteristic of the PMP optimal control strategy. Limiting the battery voltage therefore restricts optimal VES behavior more drastically then does limiting the time rate of change of battery voltage. Despite the drastic changes in battery voltage behavior due to constraining V_{min} and V_{max}, the battery voltage never drops below 11.5V, and never raises above 14V, well within the allowable voltage operating range. It logically follows that imparting constraints upon the minimum and maximum allowable battery voltage results in a greater reduction in fuel economy than reducing dV_{max}, which may be observed in Figures 44 and 46. Restricting the battery voltage operating range by 62% results in an approximately 10% reduction of the PMP fuel economy benefits, whereas restricting dV_{max} by 75% only reduces the PMP fuel economy benefits by about 5%. Therefore, in order to facilitate maximum fuel economy benefits while avoiding any undue, choppy battery current behavior, the battery voltage operating range will be minimally constrained, whereas the time rate of change of the battery voltage will be constrained by 38% (balancing the “filtering” and fuel economy benefits of the dV_{max} constraint).

The battery is subjected to much higher magnitude charging and discharging current levels when regulated by the PMP controller. In order to gather an understanding of the significance of this and quantify the extent to which the battery is utilized as an energy mover as compared to the EVR controller, the absolute net energy flux (in ampere-hours) of the battery is analyzed for both the case of the EVR and PMP control strategies. This analysis is expanded to all combinations of drive and electrical load profiles in Section 3.2.4. Table 6 summarizes the results of the energy flux analysis for the VES model subjected to the New European Drive Cycle at 57.5A.

Table 6: PMP Energy Flux Analysis Results

Controller	Energy Flux (Ah)
Chrysler EVR	4.07
Optimal Control	9.93
% Increase	**144%**

Approximately 9.93 Ah, or 13.24% of the battery’s capacity, are moved in and out of the battery model when subjected to the PMP control strategy, whereas only about 4.07 Ah are moved through the EVR-subjected battery model. The battery is therefore utilized to a much greater extent as an energy mover with the PMP control strategy in place. While fuel economy benefits are realized as a result of this, the results also imply that the battery subjected to the PMP controller will be overused (when compared to the baseline EVR controller). Any adverse effects that this overuse may have on the battery should therefore be analyzed as well.

3.2.4: Extension of Control Analysis to Numerous Data Sets

In Sections 3.2.2 and 3.2.3, the effects of the optimal control strategy on the VES model were investigated for the case of the New European Drive Cycle with a fixed electrical load of 57.5A. This allowed for an in-depth analysis in regards to the influence of numerous control parameters (i.e. system constraints, initial co-state value, etc…) on VES behavior and fuel consumption. In order to fully understand how the optimal control strategy functions over a wide variety of operating conditions, this analysis is expanded to numerous combinations of driving cycles and constant electrical load profiles. By fixing the electrical load to a constant value and varying the driving schedule, the effects which the driving schedule and electrical load demand have on the determination of the optimal control and state trajectories may be essentially decoupled from one another and studied independently. This process is critical to the development of an adaptive, implementable, Pontryagin-derived control strategy, and is summarized as follows.

The optimal initial co-state value is first located for each individual drive-cycle/electrical load combination. Simulations are then run for each optimal scenario considered, and the improvement in fuel economy, overall change in battery state of charge$(SOC_f - SOC_0)$, and net energy flux of the battery (in ampere-hours) are all tabulated. The battery SOC trajectory for each control scenario considered is studied in detail to ensure that the upper and lower state of charge bounds are not violated at any point during the drive cycle. The co-state trajectory is observed as well in order to ensure that a near-constant value is maintained over the length of the drive cycle under consideration. A representative set of co-state dynamics extracted from simulation results may be observed in Figure 47.

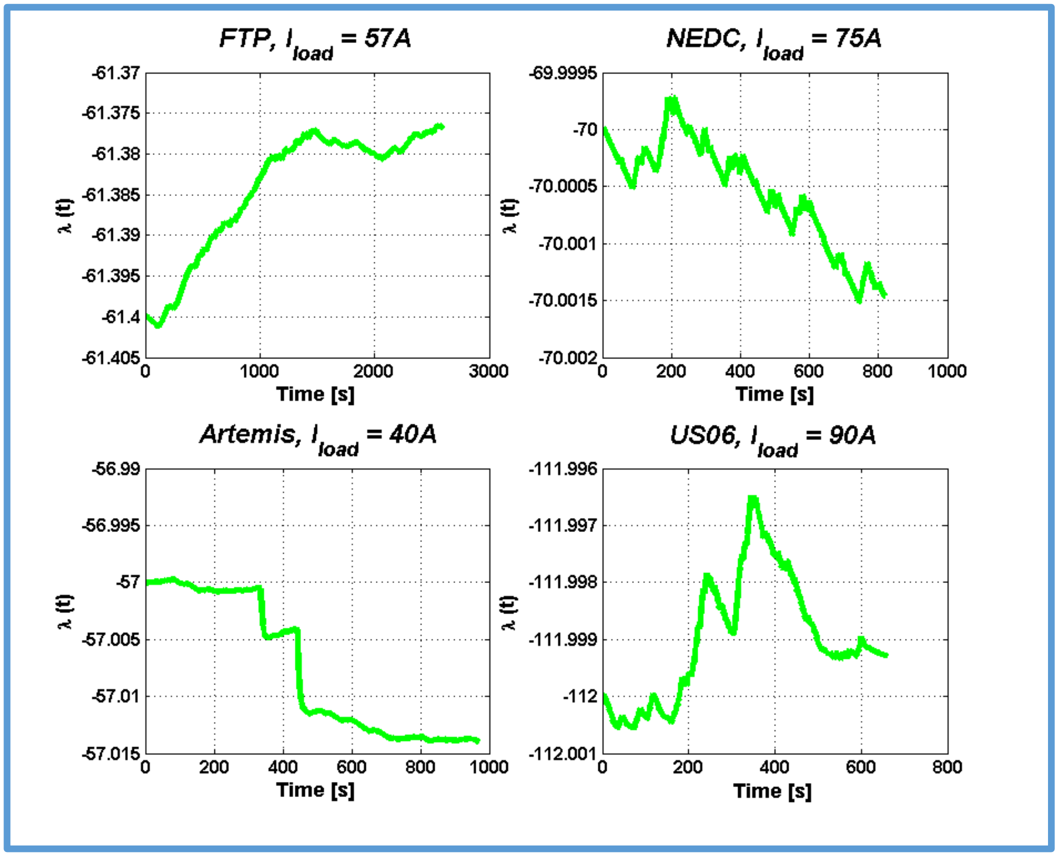

Figure 47: Sample Set of Co-state Dynamics

The initial co-state value is then increased and decreased by 25%, and the resultant improvement in fuel economy and change in battery SOC are tabulated as well. This process is performed for a total of 35 different drive-cycle/electrical load combinations, with the results featured in Tables 7-10. Take note that % F.E. denotes the percentage improvement in fuel economy over the baseline EVR control strategy.

Table 7: Listing of Performance Parameters for PMP Controller $(\boldsymbol{\lambda_0} = \boldsymbol{\lambda_0^*})$

Load [A]	**30**		**40**		**57.5**		**75**		**90**	
Drive Cycle	λ_0^*	$\%F.E.$	λ_0^*	$\%F.E.$	λ_0^*	$\%F.E.$	λ_0^*	$\%F.E.$	λ_0^*	$\%F.E.$
FTP	-59	1.7	-61	1.7	-61	1.7	-80	1.8	-105	1.7
FTP (no soak)	-56	1.8	-62	1.7	-78	1.6	-90	1.6	-108	1.6
NEDC	-27	1.8	-28	1.7	-56	2.1	-70	2.2	-90	2.2
Artemis	-54	1.2	-57	1.2	-58	1.6	-77	1.7	-97	1.7
Indian Urban	-20	1.2	-57	1.6	-66	1.8	-76	1.9	-91	1.9
JC08	-49	1.5	-53	1.9	-68	1.8	-78	1.9	-100	1.7
US06	-60	0.6	-76	1.0	-89	1.1	-105	1.0	-112	1.0

It may be observed from Table 7 that the optimal control strategy consistently provides improvements in fuel economy ranging from 0.6% all the way up to 2.2% in simulation. Additionally, the boundary penalty function μ is set to a fixed value of 400 which is sufficient, even in the case of an incorrect calibration of the initial condition of the Lagrangian multiplier, as is the case in Tables 9 and 10. Of particular interest when investigating the various optimal control scenarios featured in Table 7 is the relation between the optimal initial co-state value, the driving cycle, and the electrical load demand. At lower electrical load demands, there is a slight variance in the optimal initial co-state value from drive cycle to drive cycle; particularly in regards to the NEDC and Indian Urban drive cycles. However, as the electrical load demand is increased, the variance in λ_0 from drive cycle to drive cycle diminishes, leaving the electrical load demand as the primary factor influencing the optimal initial co-state value. Furthermore, as the actual vehicle electrical system will typically not see extended periods of usage much below 60-70A of load, the co-state drive cycle variance at 30A and 40A of load is of lesser importance than any variance at higher electrical loads. In an effort to quantify the variance in the optimal co-state value at each constant electrical load scenario considered, λ_0 is plotted versus the electrical load demand for each drive cycle. All 35 data points, one for each control scenario considered, are then linearly curve-fit. This process is depicted in Figure 48.

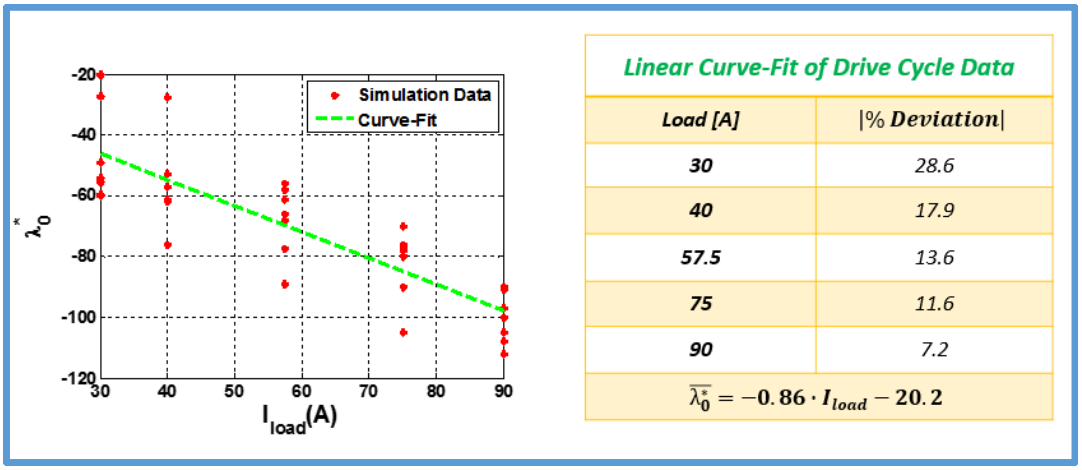

Linear Curve-Fit of Drive Cycle Data

Load [A]	$\lvert\%\ \boldsymbol{Deviation}\rvert$
30	28.6
40	17.9
57.5	13.6
75	11.6
90	7.2

$$\overline{\lambda_0^*} = -0.86 \cdot I_{load} - 20.2$$

Figure 48: Variance in Optimal Initial Co-state Value

The maximum percent deviation is simply the average percent difference between the curve-fit and each data point, and may be observed to be approximately 28.6% at an electrical load of 30A. As the electrical load is increased, this variance decreases; all the way down to 7.2% at an electrical load demand of 90A. These findings prove to be particularly significant and useful when developing an implementable PMP-based control strategy, which will be discussed in Chapter 4.

Table 8: Additional Performance Parameters for PMP Controller ($\boldsymbol{\lambda_0 = \lambda_0^*}$)

Load [A]	**30**		**40**		**57.5**		**75**		**90**	
Drive Cycle	ΔSOC [%]	$\lvert\Phi_E\rvert$ $[Ah]$	ΔSOC [%]	$\lvert\Phi_E\rvert$ $[Ah]$	ΔSOC [%]	$\lvert\Phi_E\rvert$ $[Ah]$	ΔSOC [%]	$\lvert\Phi_E\rvert$ $[Ah]$	ΔSOC [%]	$\lvert\Phi_E\rvert$ $[Ah]$
FTP	0.8	25.2	-0.1	31.3	0	32.0	0.3	26.7	-0.2	19.1
FTP (no soak)	-0.2	20.6	0.3	24.4	-0.3	24.4	0.3	22.2	0.1	16.8
NEDC	-0.5	7.6	-0.2	9.2	0.1	9.9	0	8.4	-0.2	5.3
Artemis	0.4	15.3	0.6	15.3	-0.4	12.2	-0.1	10.7	-0.2	6.9
Indian Urban	-0.2	15.3	-0.8	4.6	0	30.6	0.1	30.6	-0.3	20.6
JC08	-0.2	11.5	0.7	13.7	0.2	14.5	-0.2	12.2	-0.1	8.4
US06	0	4.6	-0.2	22.9	-0.2	9.2	0	8.4	-0.1	6.9

Referring to Table 8, two conclusions may be drawn regarding the optimal control strategy; the net change in the battery state of charge is always maintained to below 1%, and the net energy flux of the battery is typically many times greater than the EVR battery energy flux. The most severe example of the difference in battery energy flux is observed for the case of the FTP drive cycle at a fixed electrical load of 57.5A. At 32 Ah, the amount of energy flowing in and out of the battery subjected to optimal control is over 2.5 times greater than the energy flux of the battery when controlled by the EVR.

Table 9: Listing of Performance Parameters for PMP Controller ($\boldsymbol{\lambda_0 = 0.75\lambda_0^*}$)

Load [A]	**30**		**40**		**57.5**		**75**		**90**	
Drive Cycle	ΔSOC [%]	$\%F.E.$	ΔSOC [%]	$\%F.E.$	ΔSOC [%]	$\%F.E.$	ΔSOC [%]	$\%F.E.$	ΔSOC [%]	$\%F.E.$
FTP	-2.8	0.9	-2.8	0.9	-2.9	0.7	-2.6	0.8	-2.7	0.8
FTP (no soak)	-2.8	1.0	-2.8	0.9	-2.3	0.8	-2.5	0.8	-2.7	0.8
NEDC	-3.0	1.1	-3.0	1.0	-1.1	1.6	-2.9	2.1	-3.0	2.1
Artemis	-2.5	1.1	-1.8	2.0	-2.8	1.2	-2.6	1.4	-2.9	1.5
Indian Urban	-3.0	0.8	-3.0	1.0	-2.6	1.0	-2.7	1.2	-2.9	1.2
JC08	-2.7	1.0	-2.7	0.8	-2.8	0.9	-2.8	1.0	-2.9	1.2
US06	-1.4	0.5	-3.3	0.7	-1.5	0.8	-2.4	0.9	-2.8	0.9

Table 9 demonstrates the effects of under-estimating the optimal initial co-state value by 25%. This under-estimation translates to a devaluing of the battery energy, resulting in overall charge-depleting battery behavior. Despite excessive battery discharge, the fuel economy is still largely negatively influenced by this sub-optimal control behavior. Take, for instance, the percent improvement in fuel economy for the FTP drive cycle; at the optimal initial co-state value the average improvement in fuel economy over all electrical load scenarios considered is approximately 1.7%. In comparison, the average improvement in fuel economy for the FTP drive cycle when the initial co-state value is under-estimated by 25% is only about 0.7%.

Table 10: Listing of Performance Parameters for PMP Controller $(\boldsymbol{\lambda_0 = 1.25\lambda_0^*})$

Load [A]	**30**		**40**		**57.5**		**75**		**90**	
Drive Cycle	ΔSOC [%]	$\%F.E.$	ΔSOC [%]	$\%F.E.$	ΔSOC [%]	$\%F.E.$	ΔSOC [%]	$\%F.E.$	ΔSOC [%]	$\%F.E.$
FTP	3.0	0.5	3.0	0.5	2.6	0.6	2.2	0.6	3.0	0.2
FTP (no soak)	3.0	0.6	3.0	0.5	3.0	0.3	3.0	0.3	3.0	0.2
NEDC	3.0	0.4	2.8	0.5	3.0	0.6	3.0	0.5	2.3	0.5
Artemis	3.0	0.4	1.9	0.2	3.0	0.5	3.0	0.4	3.0	0.2
Indian Urban	3.0	0.4	1.7	0.7	3.0	0.8	3.0	0.8	3.0	0.7
JC08	3.0	0.4	2.9	0.3	3.0	0.1	3.0	0.2	3.0	-0.1
US06	0.1	0.3	3.0	0.2	3.1	0.3	3.0	0.1	3.0	0.0

Referring to Table 10, the fuel economy is observed to decrease drastically when the co-state variable is over-estimated by 25%. This may be attributed to two factors; the control strategy is operating on a sub-optimal control and state trajectory, and the battery is charged over the length of the drive cycle under investigation. A portion of the overall reduction in vehicle fuel economy may therefore be associated with the fuel invested into charging the battery.

By evaluating various combinations of control parameters, drive cycles, and constant electrical load demands in Sections 3.2.3 and 3.2.4, the underlying structure of the PMP control strategy is established. The critical observations and analyses performed in this chapter may be summarized as follows:

- The state constraints and reference battery SOC are selected in order to balance the benefits of improved fuel economy with the consequences of rapid battery current swings and battery over-usage.

- The governing factors which determine the optimal control and state trajectories are determined to be primarily functions of the initial co-state value, which in turn depends heavily upon the electrical load demand of the VES.
- The dependence of the initial condition of the optimal co-state value on the driving schedule diminishes as the electrical load demand increases.
- The co-state dynamics prove to be negligible, varying by as much as 0.01% in the control scenarios under consideration.

These findings are all relied upon in Chapter 4 in order to develop an adaptive, Pontryagin-based control strategy which may be implemented in a production vehicle in real-time.

Chapter 4: Development and Implementation of an Adaptive-PMP Control Strategy

In the previous chapter, an optimal control strategy was derived from Pontryagin's Minimum Principle for the energy-optimal control of the electrical system of a passenger vehicle, and was verified in simulation. While this control strategy allows one to evaluate the potential for fuel economy improvement, such benefits may not be realized without all knowledge of the driving profile and electrical load profile "a priori". Thus, there is a need to modify the existing PMP control in order to allow for an online, or "forward-looking" implementation, without "a priori" knowledge of the driving and load profiles.

The present chapter bridges the gap between the optimal PMP control strategy and an adaptive, PMP-based control strategy which is implementable in real time.

The chapter begins by highlighting the critical findings of Chapter 3 that are relevant to the development of a real-time capable control strategy; in particular the dependence of the optimal control trajectory on observable vehicle states and outputs (i.e. current, voltage, etc…). These findings are then translated into a physical control structure which replaces the co-state dynamics subsystem discussed in Section 3.1.3, thus removing the need for "a priori" input knowledge. The adaptive control strategy (A-PMP) is then tuned in simulation to yield the best possible fuel economy, and benchmarked against the PMP control. Section 4.2 discusses the controller experimental test setup, and includes a summary of experimental testing results with respect to vehicle fuel economy. Finally, Section 4.3 addresses potential drivability issues associated with the A-PMP control strategy and examines possible solutions to these problems with special consideration given to vehicle fuel economy.

Section 4.1: Design of an Adaptive PMP-based Control Strategy

Proper tuning of the initial condition of the co-state variable, λ_0, is essential in determining the optimal control trajectory with respect to both charge-sustaining behavior and minimal fuel consumption. This condition is, however, contingent on the appropriate selection of the initial condition of the co-state variable, which requires a priori knowledge regarding the specific drive cycle and electric load profile of interest. Such a control strategy is non-causal in nature, and would thus be impossible to implement in a forward-looking case. Therefore, in order recognize any potential fuel savings in-vehicle, it is first necessary to develop a control strategy that can approximate the co-state value with a separately defined control parameter, which will be termed “lambda”, and update the value of this parameter as needed to ensure charge-sustaining behavior and improve vehicle fuel economy. The newly defined control parameter (λ) is passed into the Hamiltonian calculation subsystem just as the co-state variable is in optimal control, and may be expressed as follows.

$$\lambda(k) = K_{SOC} \cdot \left(SOC(T_{s1}) - SOC_{ref}\right) + \lambda_0(T_{s2}) \tag{36}$$

Where k is an integer number indicating the discrete time step, and T_s denotes adaptations made to the function at regular intervals of fixed duration. Take note that T_{s1} and T_{s2} do not necessarily need to be equal to one another.

As discussed in Section 3.2.4, the co-state dynamics (w/ constant electrical loads imposed) appears negligible throughout the entirety of each driving schedule considered and could thus be approximated as constant and equal to its initial value. Table 8 illustrates the dependence of the initial condition of the co-state variable on both drive cycle and electrical load. While there is a notable, inversely proportional relationship between the optimal initial condition of the co-state variable and the electrical load demand, the dependence of λ_0 on the driving schedule decreases significantly as the electrical load demand increases above 57.5A. As the radiator fan alone requires 30-40A and typical operating conditions in the vehicle requires between 60-80A, the contribution of the driving profile to the optimal initial condition of the co-state variable may be neglected for implementation purposes. Following this point, the optimal initial condition of the co-state variable may be approximated solely as a function of the electrical load demand. Figure 48 quantifies the variance in the optimal initial condition of the co-state variable with no consideration given to the driving schedule, only the electrical load demand. As an example, at a load demand of 90A the percent deviation in the optimal initial condition of the co-state variable between all 7 drive cycles considered is only 7.2%, justifying the approximation of the initial condition of the co-state variable as a function of electrical load demand alone. Therefore, the electrical load demand of the vehicle may be measured in real time and passed through a lookup table in order to approximate the optimal initial condition of the co-state variable. From this point onward, λ_0 refers to the output of this lookup table and no longer to the initial condition of the co-state variable. The lookup table was generated for electrical load values of 30A, 40A, 57.5A, 75A, and 90A by averaging the corresponding optimal initial conditions of the co-state values across all driving schedules considered in Section 3.2.4, with the exception of the NEDC and Indian Urban drive cycle. The NEDC and Indian Urban drive cycles are ignored due to numeric disparities with the rest of the initial conditions of the co-state variables (at low electrical loads). Table 11 features the λ_0 lookup table as a function of electrical load.

Table 11: λ_0 Lookup Table

$I_{load}\ (A)$	$\lambda_0(I_{load})$
30A	**-55.6**
40A	**-61.9**
57.5A	**-70.8**
75A	**-86**
90A	**-104.4**

The λ_0 lookup table does not operate continuously in time, but rather is updated at discrete sampling instances ($T_{s2} = T_s(I_{load})$). This provides for an educated projection of the charge-sustaining control solution, however the battery state of charge will depart from the reference value without an additional term incorporated into λ.

A proportional correction on this “SOC-drifting” behavior, which is based on SOC feedback and ensures the robustness of the control strategy [17], is necessary to ensure that excessive battery depletion or charging does not occur. This approach towards ensuring charge-sustaining battery behavior has been used in automotive control applications with success, and may be investigated in greater detail in [31, 34]. From an implementation perspective, the proportional correction on the battery state of charge may be expressed as follows.

$$\text{SOC Correction Factor} = K_{SOC} \cdot (SOC(k) - SOC_{ref}) \tag{37}$$

Where K_{SOC} is the proportional gain on the differential of the battery state of charge, $SOC(k)$ is the actual battery state of charge, and SOC_{ref} is the reference battery state of charge. The corrective term on the battery state of charge is updated at discrete sampling times ($T_{s1} = T_s(\Delta SOC)$), in order to allow the vehicle to make use of the available energy buffer. The SOC-correction is added to the output of the λ_0 lookup table, and the resulting sum (alongside the average of the previous two lambda values) is taken as an input into the Hamiltonian calculation subsystem.

Figure 49 assists in visualizing the underlying control logic of the newly defined “Lambda-Calculation Subsystem”, which replaces the co-state dynamics subsystem of the previously discussed PMP control. Take note that the electrical load demand is passed through a moving average subsystem which filters the signal prior to the λ_0 LUT. The purpose of the filter is to mitigate the high-frequency noise inherent in the battery and alternator current measurements and allow for an approximation of the appropriate lambda value based on the mean electrical load demand.

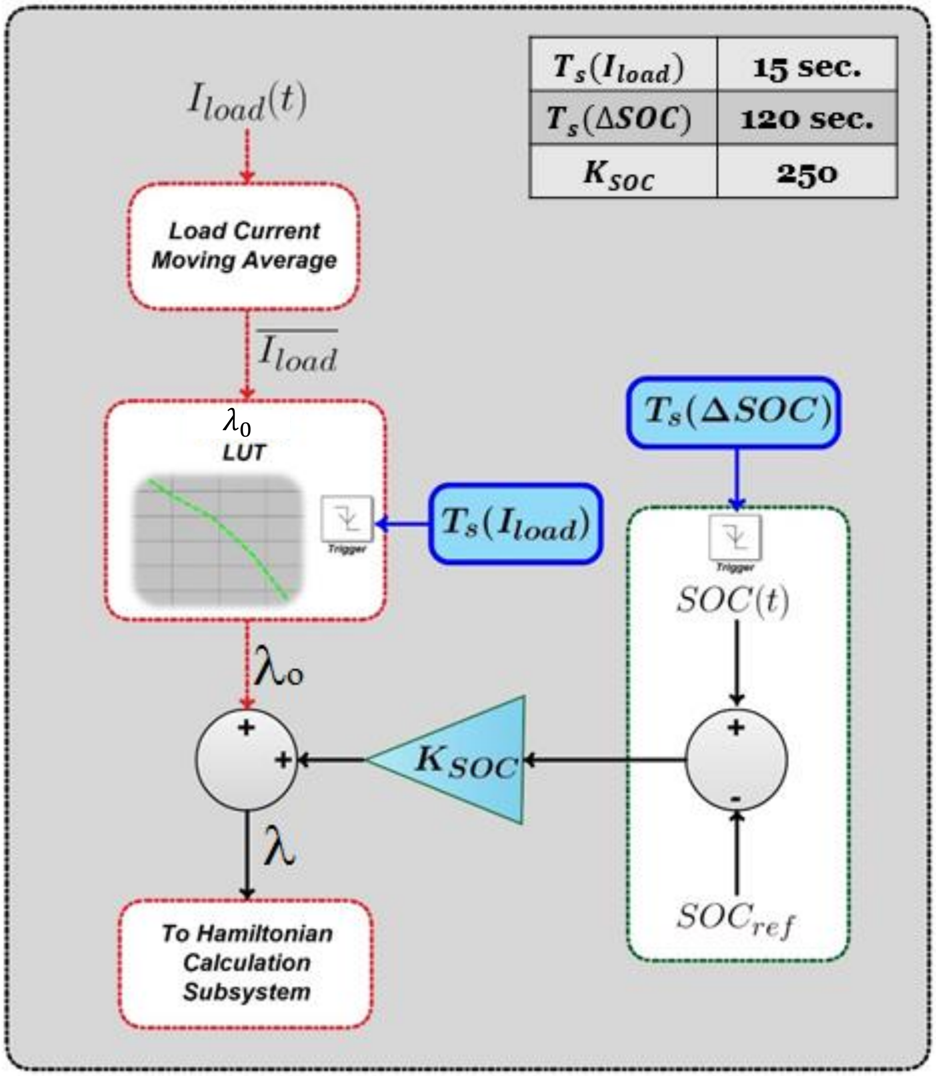

Figure 49: Lambda Estimation Control Structure

The gain on the battery state of charge, K_{SOC}, needs to be calibrated to ensure proper weighting of the battery energy at both the upper and lower state of charge thresholds. In particular, the net lambda value (i.e. the sum of the LUT and the SOC-correction) must assist in maintaining the battery SOC around the reference value while still allowing freedom for the battery to operate as an energy mover. If, for example, K_{SOC} is set to too large a value, the battery SOC dynamics will be restricted and fuel economy benefits may be significantly reduced. On the hand, if K_{SOC} is set to a very small value, the battery SOC will eventually drift to either the upper or lower threshold value, chattering for the remainder of the drive cycle and reducing potential fuel savings. Proper calibration of the proportional gain on the battery state of charge is therefore critical to the successful implementation of an adaptive-PMP control strategy. In order to quantify the effects of changing the SOC-gain and ensure that the best possible value is selected, the influence of K_{SOC} on the trajectory of the battery state of charge and overall vehicle fuel economy must be studied. The magnitude and frequency of the low frequency state of charge trajectory are useful metrics in understanding how changes in the SOC-gain effect battery behavior. Figure 50 illustrates how the SOC magnitude and frequency are determined, and features simulation data derived from an on-road drive cycle. Take note that prior to any calculation of the SOC magnitude and frequency, the state of charge signal is filtered to remove dynamics with a frequency greater than 0.1Hz. This filter is implemented, strictly in post-processing, to allow for accurate calculation of the “peak-to-valley” SOC values (i.e. the SOC magnitude) and the “peak-to-valley” time intervals (i.e. the inverse of the SOC frequency).

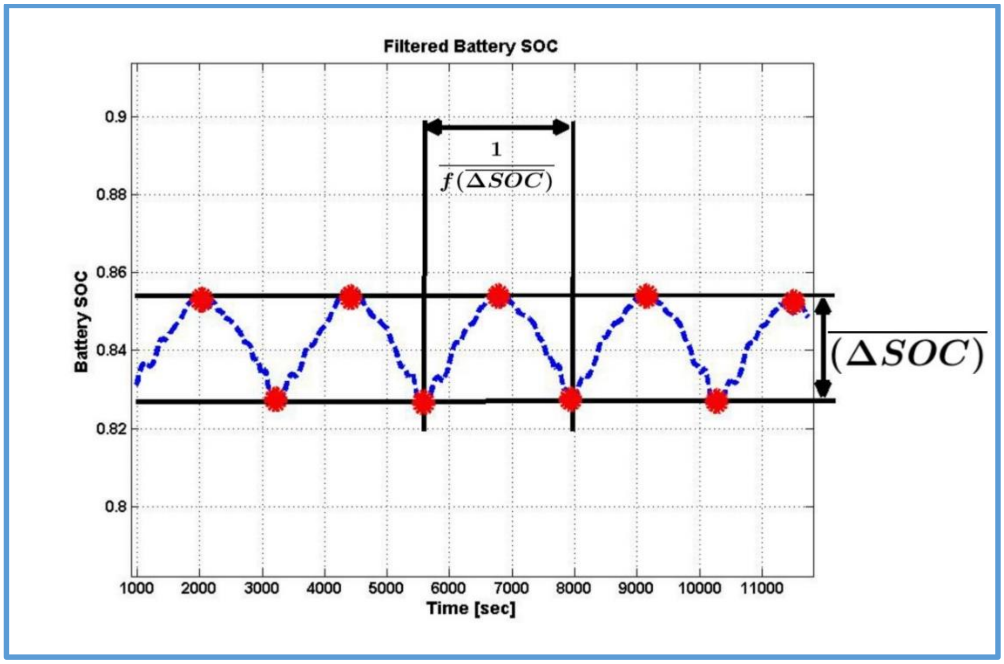

Figure 50: Metrics Used to Quantify State of charge Dynamics

Each SOC peak (maximum) and valley (minimum) is determined and marked, as observed in Figure 50. The mean SOC “swing magnitude”, $\overline{\Delta SOC}$, and the SOC “swing frequency”, $f(\overline{\Delta SOC})$, are then calculated by averaging the sum of the individual parameter values. Table 12 catalogues the effects, in simulation, of changing K_{SOC} on the aforementioned SOC metrics, as well as fuel economy, over an on-road experimental drive cycle with experimental electrical loads. This drive cycle, analyzed in simulation, will be the basis for all control parameter tuning for the remainder of Section 4.1. Take note that the rightmost column of Table 12 quantifies the ratio of the improvement in fuel economy w/ the adaptive control in place over the improvement in fuel economy w/ optimal control in place (i.e. $\%F.E.^{*}$).

Table 12: Effects of Modifying SOC Gain

$\boldsymbol{K_{SOC}}$	$\overline{\boldsymbol{\Delta SOC}}$ **[%]**	$\frac{\mathbf{1}}{\boldsymbol{f(\overline{\Delta SOC})}}$ $[\boldsymbol{sec}]$	$\frac{\%\boldsymbol{F.E.}}{\%\boldsymbol{F.E.}^*}$
100	6	1143	0.93
250	5.6	1180	0.94
500	5.2	1173	0.93
1500	4.2	1144	0.92
3000	2.6	2473	0.89

As K_{SOC} is increased from 100 to 3000, $\overline{\Delta SOC}$ decreases by approximately 57%. At a value of 100, the battery is making use of the entirety of its SOC operating range (+/- 3% SOC), and even saturates at the threshold values. In comparison, when $K_{SOC} = 3000$, the battery is using less than half of its allowable capacity. This behavior is to be expected, as increasing the SOC-gain results in more charging at low SOC values and more discharging at high SOC values, therefore discouraging SOC fluctuations. The period of the SOC swings increases significantly when the gain is elevated from 1500 to 3000 due to the restriction imposed on the battery dynamics. As the battery is forced to operate within a very limited range of SOC values, "peaks" and "valleys" in the state of charge are less likely to occur. Increasing the gain on the SOC differential has adverse effects on the fuel economy due to more stringent limitations on the state of charge dynamics. The battery is therefore not used to its fullest potential as an energy buffer. At an SOC-gain value of 250, the fuel economy benefit provided by the adaptive control strategy is only 6% less than what optimal control provides. In contrast, when $K_{SOC} = 3000$, the adaptive controller provides 11% less fuel economy benefit than the optimal control. A tradeoff is therefore associated with selecting a value for K_{SOC}; too high of a value results in diminished fuel economy benefits due to restrictions on battery usage, whereas too low of a value potentially results in the battery reaching the SOC thresholds, thus also reducing vehicle fuel economy (as shown in Table 12 for $K_{SOC} = 100$). A SOC-gain of 250 provides maximum fuel economy while also preventing the state of charge from reaching either the upper or lower allowable value, and is therefore selected for implementation in the vehicle.

Referencing Figure 49, both the λ_0 lookup table and the proportional gain on the state of charge differential include update times; $T_s(I_{load})$ and $T_s(\Delta SOC)$, respectively. The update time on the λ_0 LUT, $T_s(I_{load})$, physically operates by sampling the moving average of the electrical load signal at specified time intervals (T_s) and holding the sampled value in between sampling instances. This provides the functionality of smoothing out the dynamics of λ, and must be tuned in order to capture the true electrical load behavior. If the sampling time is too large, major changes in the electrical load (such as what may be introduced by switching on the cabin blowers or radiator fan) could potentially be neglected due to the presence of the moving average filter, resulting in non-representative values of λ_0. Thus, it is necessary to select a suitable value for $T_s(I_{load})$ which can take into account any significant changes in electrical load behavior while also mitigating erratic co-state behavior. Table 13 catalogues the effects which $T_s(I_{load})$ has on the battery SOC and vehicle fuel economy. In addition, the RMS error, $e_{RMS}(I_{load})$, of the filtered electrical load signal as compared to the actual electrical load is tabulated for reference.

Table 13: Effects of Modifying $\boldsymbol{T_s(I_{load})}$

$\boldsymbol{T_s(I_{load})}$ **[sec]**	$\boldsymbol{e_{RMS}(I_{load})}$ **[sec]**	$\boldsymbol{\overline{\Delta SOC}}$ **[%]**	$\boldsymbol{\frac{\%F.E.}{\%F.E.^*}}$
15	6.87	5.4	0.93
60	9.17	5.8	0.93
120	11.09	5.9	0.89
180	12.75	6.0	0.89

The RMS error of the filtered electrical load signal increases as the sampling period increases, translating to a less representative value for λ_0, and resulting in excessive drifting of the battery state of charge from the reference value. At a sampling period of 180 seconds, the magnitude of SOC swings is equal to the allowable operating range of the battery. In addition, as $T_s(I_{load})$ is increased from 60 seconds to 120 seconds, the fuel economy benefit decreases from 93% to 89%, largely due to the battery SOC reaching the operating limits of the battery state of charge. While allowing the battery to make full use of its SOC operating range proves beneficial to vehicle fuel economy, any time the battery spends operating at the upper and lower threshold values has adverse effects on fuel economy. Therefore, as a preventative measure, $T_s(I_{load})$ is selected such that battery operation around the upper and lower allowable SOC values is kept to a minimum, while still allowing for an accurate calculation of the λ_0. A sampling period of 15 seconds satisfies both criteria, and is therefore deemed suitable for vehicle implementation.

The update time for the gain on the SOC differential, $T_s(\Delta SOC)$, is necessary to allow the controller to function more freely within the batteries allowable operating range (and thus closer to the optimal control command). For example, with $T_s(\Delta SOC)$ set to a very low value, as would be the case if $T_s(\Delta SOC) = T_s(I_{load})$, a significant departure from the optimal control command will occur in proximity of the SOC thresholds due to the heavily weighted additional term introduced by K_{SOC}. A portion of the batteries operating range may therefore be under-utilized, resulting in diminished fuel economy benefits. In comparison, a very large value for $T_s(\Delta SOC)$ tends to neglect SOC-drifting and potentially allow the battery state of charge to reach the upper or lower allowable SOC values, resulting in undesirable SOC chattering and again reducing the potential fuel economy benefits that may be realized with such a control strategy. From a physical standpoint, $T_s(\Delta SOC)$ is implemented by sampling the actual battery state of charge at predefined time intervals, and holding this SOC value between sampling instances. A study into the behavior of the A-PMP control strategy subject to various values of $T_s(\Delta SOC)$ is featured in Table 14.

Table 14: Effects of Modifying $\boldsymbol{T_s}(\Delta\boldsymbol{SOC})$

$\boldsymbol{T_s}(\Delta\boldsymbol{SOC})$ [sec]	$\overline{\Delta\boldsymbol{SOC}}$ [%]	$\frac{\%\boldsymbol{F.E.}}{\%\boldsymbol{F.E.}^*}$
30	5.2	0.91
60	5.3	0.91
120	5.5	0.93
180	5.7	0.93

As the sampling time for the SOC-gain is increased from 30 to 180 seconds, $\overline{\Delta SOC}$ increases from approximately 86% to 95% of the operating range of the battery. The resulting fuel economy ratio reflects this, increasing from 91% to 93%. Similar to the selection process laid out for $T_s(I_{load})$, the sampling time for the state of charge gain is chosen in order to balance fuel economy benefits with the potential ramifications of allowing the state of charge to drift into either the upper or lower threshold. A sampling time of 120 seconds proves to satisfy the desired performance criteria, and is therefore selected for implementation in the vehicle. Table 15 summarizes the control parameters selected for in-vehicle implementation

Table 15: A-PMP Control Parameter Selection Summary

Control Parameter	Value
$\boldsymbol{K_{SOC}}$	250
$\boldsymbol{T_s(I_{load})}$	15
$\boldsymbol{T_s(\Delta SOC)}$	120

It may be observed from Tables 12-15 that the adaptive control strategy yields fuel savings ranging from approximately 89-94% of the results provided by the optimal control for the experimental drive cycle under consideration, with the primary drivers of these disparities relating to the introduction of an approximation of co-state dynamics and in the model describing the variation of the control parameter λ_0. The effects of these approximations are not strictly limited to fuel economy, but alter the control trajectory, and thus VES behavior, as well. In particular, any departure from optimal control will result in a change in the duty-cycle command and the battery state of charge trajectory. With minimal fuel economy differences observed between optimal control and the A-PMP control strategy, it is reasonable to expect that the A-PMP control and SOC trajectories will resemble those resulting from optimal control. Figure 51 depicts the control command trajectories for both optimal control and the A-PMP control strategy. Figure 52 illustrates the similarities between the optimal control and A-PMP state of charge dynamics over the first 815 seconds of the aforementioned experimental drive cycle.

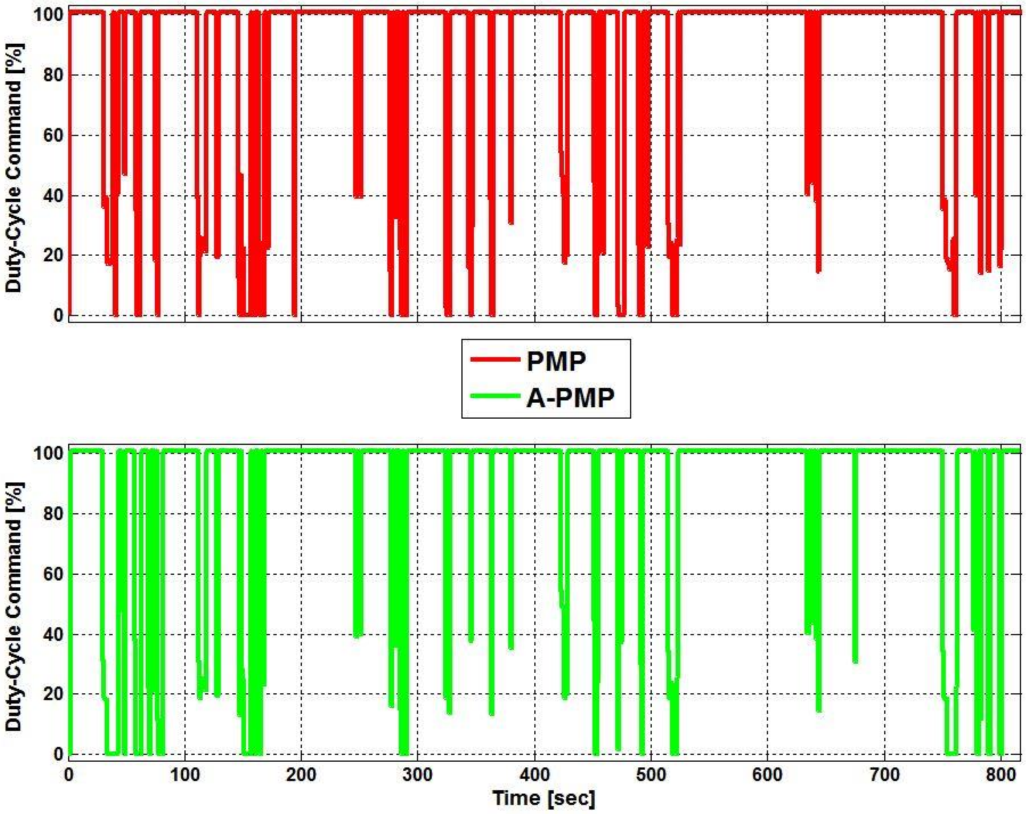

Figure 51: Comparison of PMP and A-PMP Control Command Trajectories

Referencing Figure 51, the A-PMP control command is observed to closely follow the optimal control command.

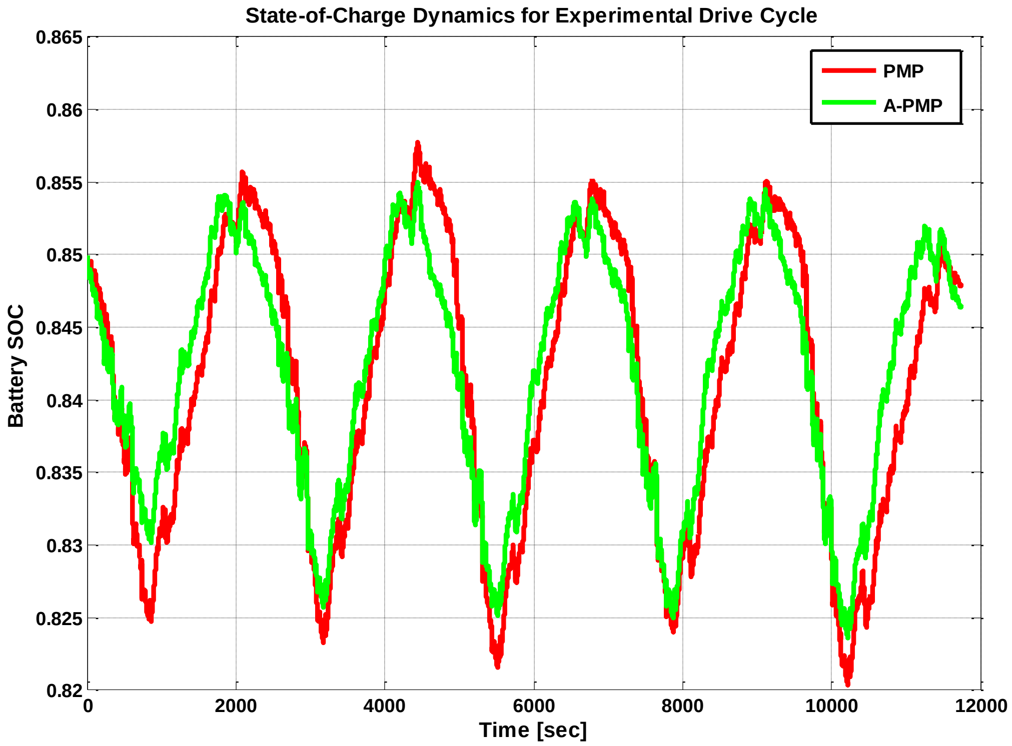

Figure 52: Comparison of PMP and A-PMP Battery SOC Dynamics

Figure 52 depicts the similarities between the optimal control and adaptive control state of charge dynamics. The final battery state of charge of both the PMP and A-PMP control strategies lie within half of a percentage of the initial SOC, indicating that the adaptive control strategy provides suitable estimations of the co-state variable throughout the entirety of the drive cycle under consideration. The battery subjected to the adaptive control strategy is, however, observed to function within a smaller SOC operating range, primarily due to the imposition of the state of charge corrective factor, K_{SOC}. As the battery SOC diverges from the reference trajectory, the effects of the SOC correction become more apparent (as may be noted in the "valleys" of the battery SOC).

Nonetheless, the adaptive control strategy provides near-optimal fuel economy improvements, and results in control command and SOC trajectories which are very similar to that resulting from optimal control. To ensure acceptable adaptive-control performance across a wide variety of driving styles, the A-PMP controller is benchmarked in simulation against the PMP control strategy with 3 additional experimental data sets. The results of this analysis are featured in Table 16. Take note that the data set analyzed throughout this section is titled “On-Road (08/30) x5”. Take note that “(08/30)” refers to the date of experimental testing, and is used to differentiate the two different experimental drive cycles considered in this section.

Table 16: Benchmarking of A-PMP against Optimal Control in Simulation

Drive Cycle	**% $F.E.$**	% $F.E.^*$
On-Road (08/30) x5	1.2	1.3
On-Road (09/06) x5	1.1	1.1
FTP x5	1.6	1.7
NEDC x5	1.5	2.0

The adaptive PMP control strategy consistently provides near-optimal fuel economy improvements, despite the lack of “a-priori” velocity and electrical load profile information. Furthermore, the battery SOC is maintained within the desired operating range, avoiding any concern of excessive battery charging or discharging. This control strategy is therefore suitable for real-time control, and may be directly implemented in-vehicle.

Section 4.2: Implementation and Experimental Testing of the A-PMP Control Strategy

In order to facilitate timely controller implementation and tuning, an ETAS ES1000.3 rapid prototyping platform is utilized for experimental testing. Detailed information regarding the underlying hardware and software of the ETAS system is described and illustrated in Section 2.1.2. Intecrio Experiment Environment software, operating on an in-vehicle laptop computer, enables real-time controller tuning and vehicle behavioral analysis, and allows for data acquisition as well. Experiment Environment also has the added benefit of allowing the user to ensure that individual control subsystems and all sensors coupled to the ETAS platform are functioning appropriately. Figure 53 illustrates the Experiment Environment user interface during experimental controller testing.

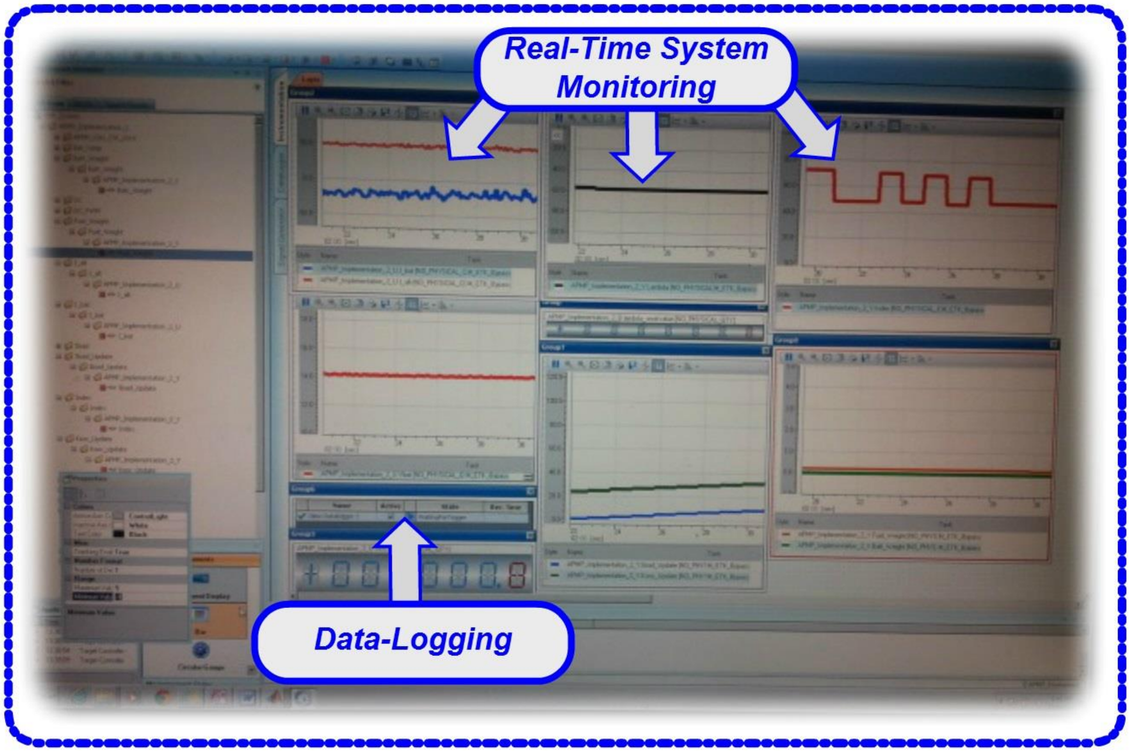

Figure 53: Intecrio Experiment Environment User Interface

As discussed in Section 2.1.2, both a battery and alternator shunt, as well as an ETAS ETK-ECU bypass driver allow for control system feedback. In order to allow for entirely closed-loop functionality, the battery state of charge needs to be monitored in real-time as well. This is not only critical to the calculation of the Hamiltonian, as discussed in Section 3.1.3, but is also required for implementation of the SOC correction factor, K_{SOC}. While estimating the battery state of charge through integration of the experimental battery current signal ideally allows for precise SOC monitoring, battery inefficiencies, signal noise, and measurement errors accumulate over time and contribute to the actual battery SOC diverging from the calculate battery SOC. For these reasons, a Bosch

Intelligent Battery Sensor (IBS) was installed on the automotive battery. The IBS software consists of a Kalman filter with a 3rd-order equivalent circuit lead-acid battery model, and allows for estimation of the battery state of charge with a resolution of 1%. Figure 54 illustrates the structure of the IBS.

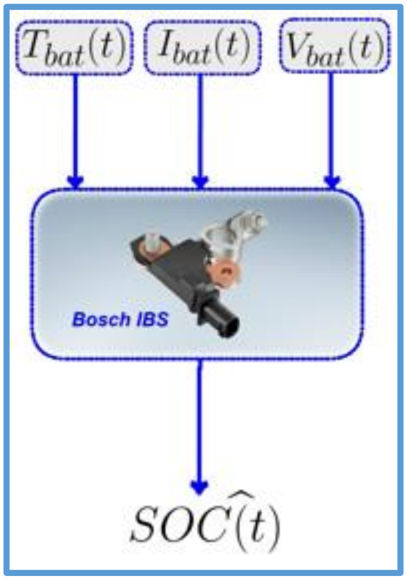

Figure 54: Bosch IBS Kalman Filter Lead-Acid Battery I/O

The battery terminal voltage, current and temperature $(V_{bat}, I_{bat}, T_{bat})$ are the measured inputs of the Kalman filter, whereas $SO\hat{C}(t)$ is the estimated state variable. The IBS is directly fastened to the ground terminal of the automotive battery, with a lead wire coupled to the positive terminal of the battery.

The IBS utilizes a serial network protocol termed LIN (Local Interconnect Network) which allows for communication between the battery sensor (slave node) and the LIN controller (master node). LIN is analogous to a single-wire CAN communication network, and sends and receives data frames in hexadecimal format. Thus, there is a need to translate the LIN hexadecimal data which corresponds to the battery state of charge into a usable analog voltage signal which may be incorporated into the ETAS system. Labview 2013, a laptop computer, a National Instruments USB-8476s LIN interface, and a National Instruments USB-6009 multifunction DAQ are used for this purpose. Figure 55 illustrates the experimental setup used to incorporate the IBS LIN signal into the pre-existing ETAS system.

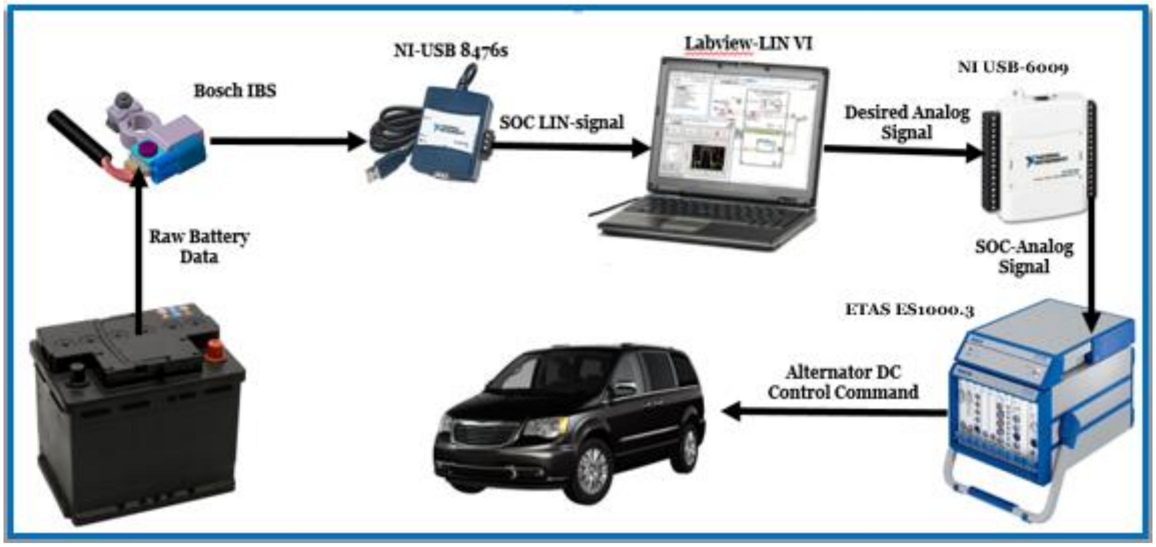

Figure 55: IBS Experimental Test Setup

In order to ensure the IBS' functionality, a validation of the battery sensor is performed. This task is carried out by comparison of the IBS' own measured battery current signal with the battery current signal recorded from the battery shunt. Figure 56 overlays the battery current, as measured by the battery shunt, with the battery current signal provided by the Bosch IBS. This data was collected with the vehicle parked and the engine running under idle conditions. The duty-cycle of the alternator was randomly fluctuated and various electrical loads were powered on and off, such as the cabin blowers and heated seats, in order to provide an electrical load profile representative of real-world conditions.

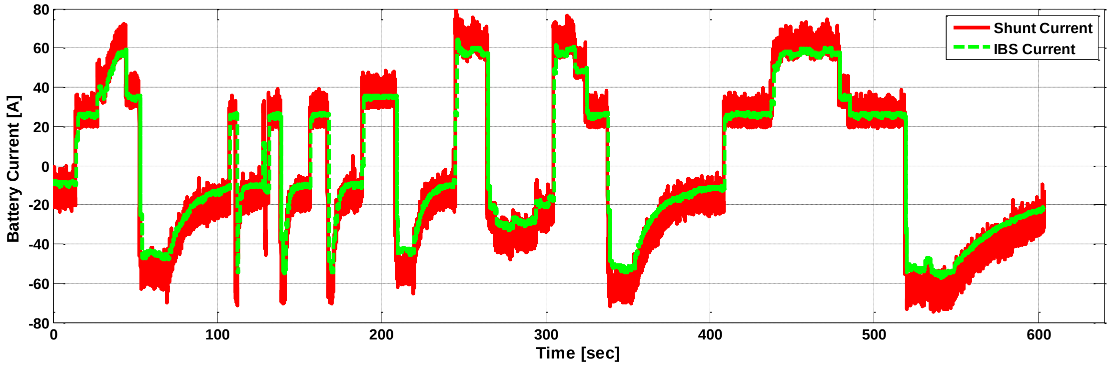

Figure 56: Comparison of Battery Shunt and IBS Battery Current Signal

The IBS battery current signal corresponds with the battery shunt current signal over the entirety of the electrical load profile considered, which provides an indirect method of verifying the IBS' ability to estimate the battery state of charge.

The vehicle, equipped with all necessary testing apparatus, was installed on a light-duty chassis dynamometer in order to perform numerous regulatory and random "errand" drive cycles with the A-PMP control strategy activated. More information regarding the chassis dynamometer experimental setup may be found in Section 2.1.1. Although the chassis dynamometer does present advantages with respect to determining a given vehicles fuel economy, certain issues do arise associated with driver inaccuracies and variations in ambient conditions. In a recent study performed at OSU-CAR, the net fuel consumption of the vehicle over 8 separate NEDC drive cycles, as calculated by both the fuel flow-rate signal logged by the ECU and the Big-Grid fuel consumption map, was analyzed. The cycle-to-cycle variation in net fuel consumption was found to exceed 5% in certain instances. Tables 17 and 18 show the results from this study in cycle-to-cycle percent variation.

Table 17: Cycle-to-Cycle Percent Fuel Consumption Variation as Calculated by ECU

NEDC Cycle No.	1	2	3	4	5	6	7	8
1	-	-0.10	3.02	-1.12	-1.83	-0.32	1.51	1.89
2	0.10	-	3.12	-1.02	-1.74	-0.22	1.61	1.99
3	-3.02	-3.12	-	-4.11	-4.80	-3.33	-1.53	-1.15
4	1.12	1.02	4.11	-	-0.72	0.80	2.62	2.99
5	1.83	1.74	4.80	0.72	-	1.52	3.32	3.69
6	0.32	0.22	3.33	-0.80	-1.52	-	1.83	2.21
7	-1.51	-1.61	1.53	-2.62	-3.32	-1.83	-	0.39
8	-1.89	-1.99	1.15	-2.99	-3.69	-2.21	-0.39	-

Table 18: Cycle-to-Cycle Percent Fuel Consumption Variation as Calculated by Big-Grid Fuel Map

NEDC Cycle No.	1	2	3	4	5	6	7	8
1	-	-0.26	2.30	-2.57	-3.04	-2.97	-2.16	-2.30
2	0.26	-	2.56	-2.31	-2.78	-2.72	-1.90	-2.04
3	-2.30	-2.56	-	-4.81	-5.27	-5.21	-4.41	-4.54
4	2.57	2.31	4.81	-	-0.48	-0.41	0.42	0.28
5	3.04	2.78	5.27	0.48	-	0.06	0.90	0.76
6	2.97	2.72	5.21	0.41	-0.06	-	0.83	0.69
7	2.16	1.90	4.41	-0.42	-0.90	-0.83	-	-0.14
8	2.30	2.04	4.54	-0.28	-0.76	-0.69	0.14	-

Due to the expected improvements in fuel economy of approximately 1-2%, a different approach is clearly required in order to estimate the fuel economy benefits which the A-

PMP control strategy presents over the baseline EVR controller. In order to provide a baseline for comparing the performance of the A-PMP controller (in-vehicle), simulations were conducted using the VES model together with the model of the Chrysler control strategy. Such models have been described in Chapter 2. Therefore, the issues associated with drive cycle repeatability may be mitigated by using engine and electrical load experimental data collected with the A-PMP activated in conjunction with the VES-EVR model. This approach not only ensures that the same velocity profile is followed for both control strategies, but also eliminates disparities in vehicle and ambient operating conditions. In order to estimate the fuel consumption of the vehicle with the A-PMP controller in place, the A-PMP experimental data sets are used to calculate the alternator torque. The alternator torque is then summed with the measured engine torque, and passed through the Big-Grid fuel consumption map alongside the measured engine speed.

Four different experimental data sets in total are used to analyze the fuel economy benefits of the A-PMP controller with the aforementioned technique; 2 random “errand” drive cycles and 2 standardized cycles, one consisting of two consecutive FTPs performed back-to-back and a second comprised of an EPA driving schedule. The random errand drive cycles were performed on the chassis dynamometer with no particular velocity trace observed. The objective of these tests is to emulate a variety of real-world driving conditions by varying both vehicle velocity and electrical load demand. A “double-FTP”, as well as the EPA cycle, were performed in order to examine the effects which the electrical load demand has on the realized fuel savings. The EPA drive cycle was performed with all electrical accessory loads turned off, and the double-FTP test was performed with varying electrical loads (i.e. cabin blowers, radio, heated seats powered on and off). In this section, the variable load FTP drive cycle as well as one of the two random errand drive cycles are considered. The EPA cycle, as well as the second errand drive cycle, are analyzed in Section 4.3 for reasons discussed therein. Table 29 summarizes the experimental improvement in fuel economy (over the baseline EVR controller) for the two drive cycles currently of interest.

Table 19: Experimental Improvement in Fuel Economy due to A-PMP

Drive Cycle	% F.E.
Random Cycle #1	1.4
FTP x2 (Variable Loads)	1.3

The experimental fuel economy observed due to the incorporation of the A-PMP control strategy into the vehicle electrical system provides for an improvement ranging from 1.3-1.4%, depending primarily on the velocity and electrical load profile imposed on the vehicle. In particular, driving schedules which include more frequent acceleration and deceleration events and require more power from the battery and alternator exhibit significantly greater fuel savings as opposed to driving schedules with excessive idling and little electrical load demand. Figures 57-60 illustrate the critical vehicle, engine, and electrical system behavior for Random Cycle #1.

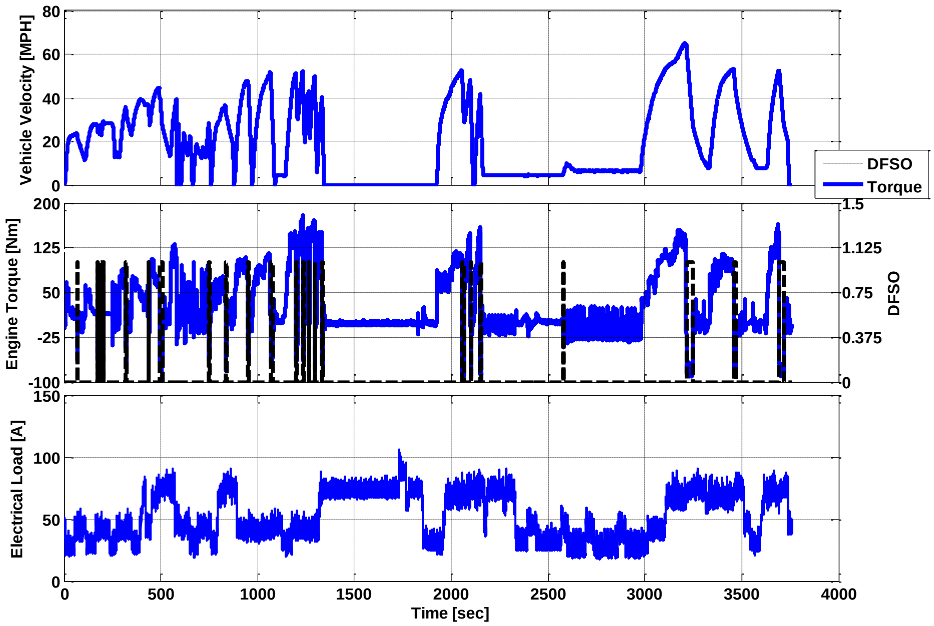

Figure 57: A-PMP Experimental Vehicle Behavior, Random Drive Cycle 1

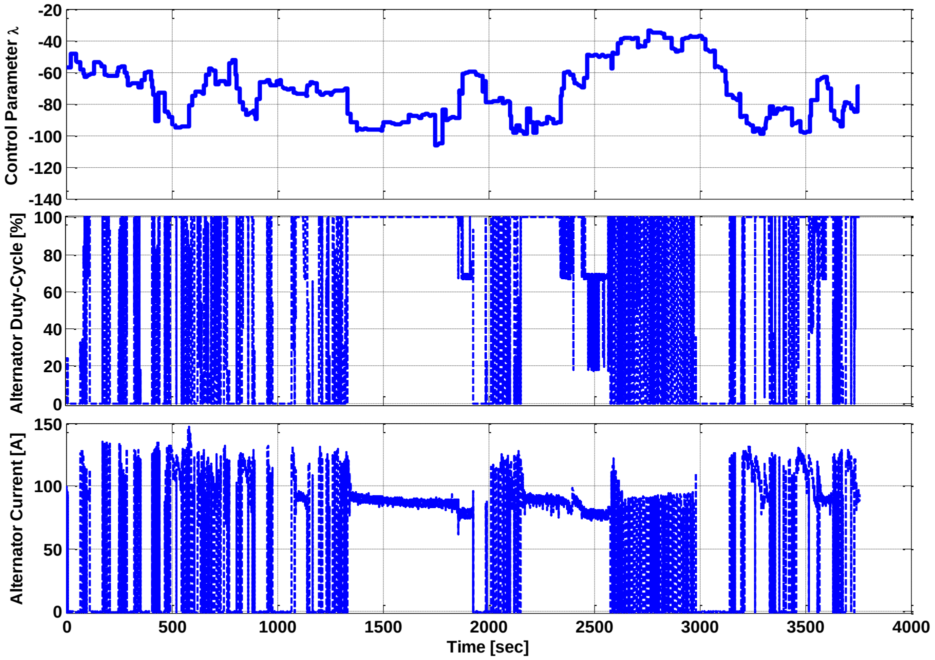

Figure 58: A-PMP Experimental Control Behavior, Random Drive Cycle 1

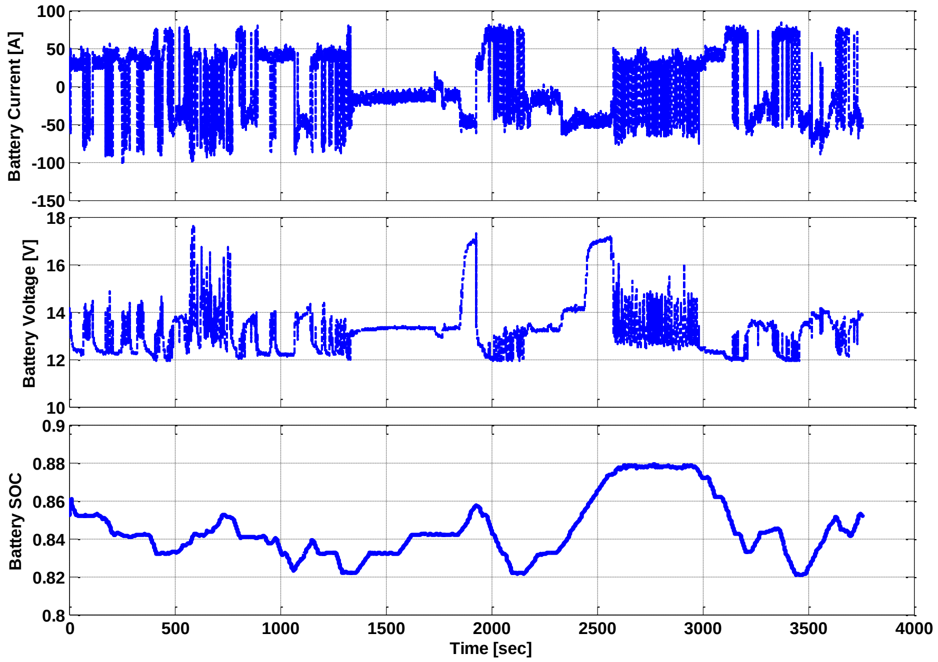

Figure 59: A-PMP Experimental Battery Behavior, Random Drive Cycle 1

Figure 60: A-PMP Experimental Fuel Consumption, Random Drive Cycle 1

Of particular interest is the battery charging/discharging behavior with respect to the vehicle velocity trace. As discussed in Section 3.2.2, behavior reminiscent of regenerative braking is observed with the A-PMP controller in place, as may be observed in Figures 57-60. Hard acceleration events are accompanied by battery discharge, and coasting/braking leads to battery charging. This behavior agrees very well with both optimal control and the adaptive control (in simulation), yielding confidence in the implementation of the controller. Referring to Figure 59, the battery voltage exceeds 15V (the maximum allowable battery voltage) due to inaccuracies associated with the 0th-order battery model and the update time of the A-PMP control strategy (1 second). The battery SOC, on the other hand, remains confined between 82% and 88%, with high-frequency battery current oscillations occurring at the upper and lower thresholds due to the activation of the boundary penalty function, μ. Lambda is observed to reach a maximum value of approximately -40 as the battery state of charge approaches 88%, illustrating the impact of the state of charge gain on lambda. Figure 60 compares the EVR and A-PMP alternator torque profiles along with each control strategies cumulative fuel consumption. The alternator torque profiles clearly demonstrate the rapid-switching behavior characteristic of PMP control. The A-PMP alternator torque exceeds that of the EVR torque under certain circumstances (i.e. vehicle deceleration/coasting), however the fuel losses incurred at this time are more than replenished (as compared to the EVR) as the vehicle accelerates and the battery supplies all necessary power to the electrical loads. The EVR leads to a net fuel consumption of 2028g, whereas the vehicle consumes 2000g of fuel with the A-PMP activated. Figures 61-64 show similar plots for the variable-load dual-FTP drive cycle. An in-depth discussion regarding the trends observed in the following figures will be left to the reader, as observations similar to those just noted may be made.

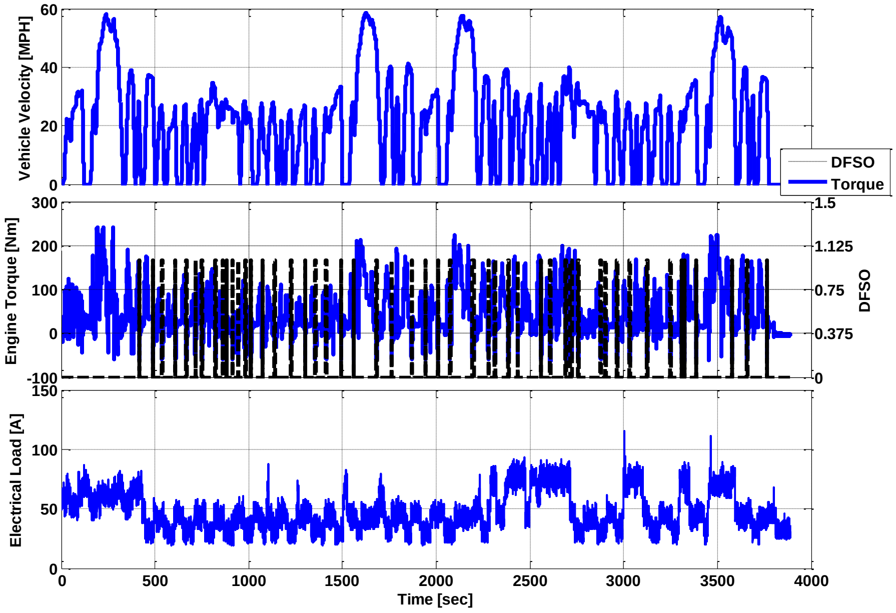

Figure 61: A-PMP Experimental Vehicle Behavior, Dual-FTP w/ Variable Loads

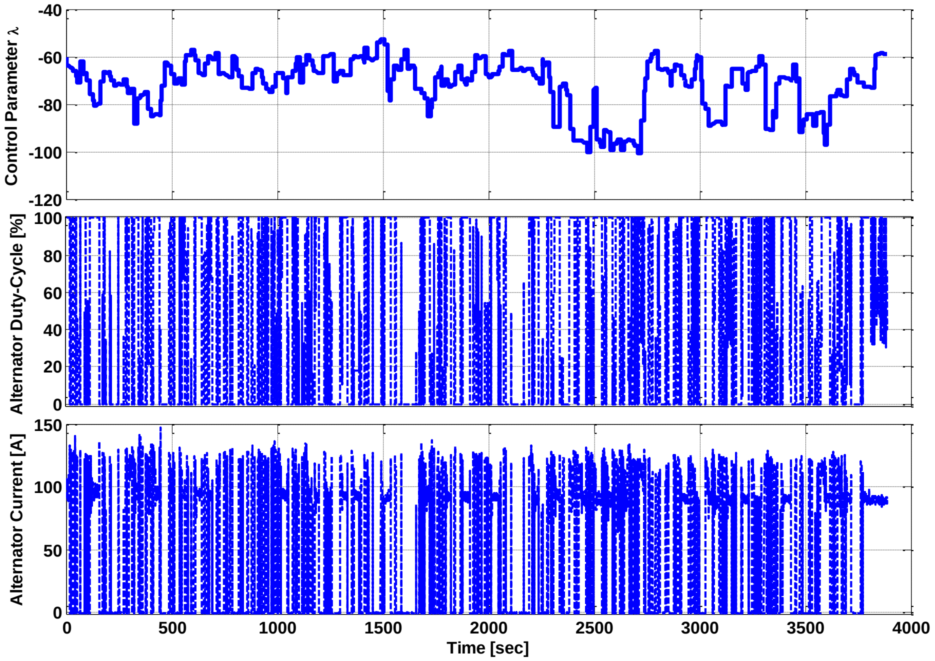

Figure 62: A-PMP Experimental Control Behavior, Dual-FTP w/ Variable Loads

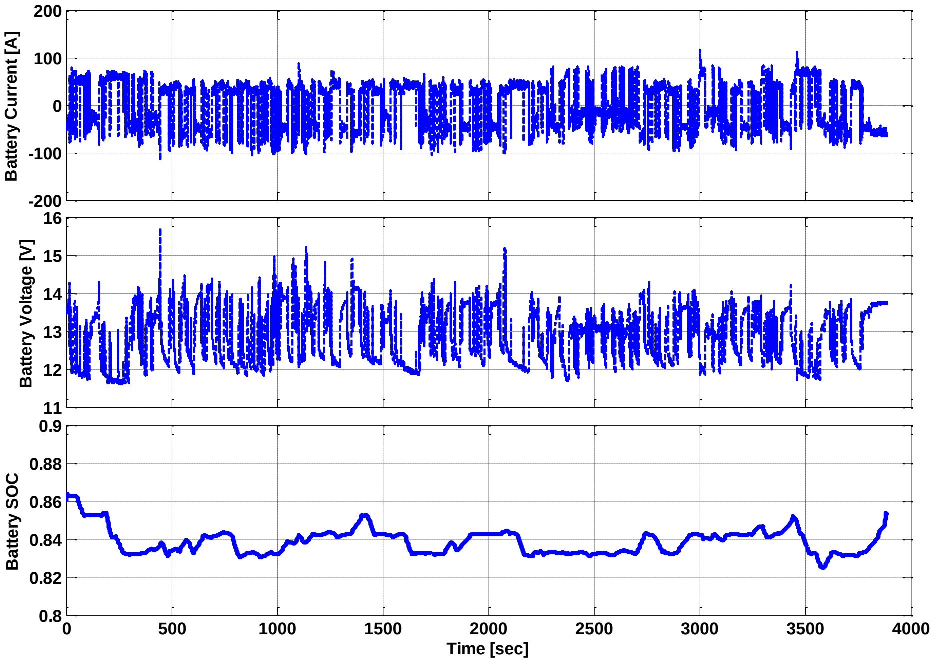

Figure 63: A-PMP Experimental Battery Behavior, Dual-FTP w/ Variable Loads

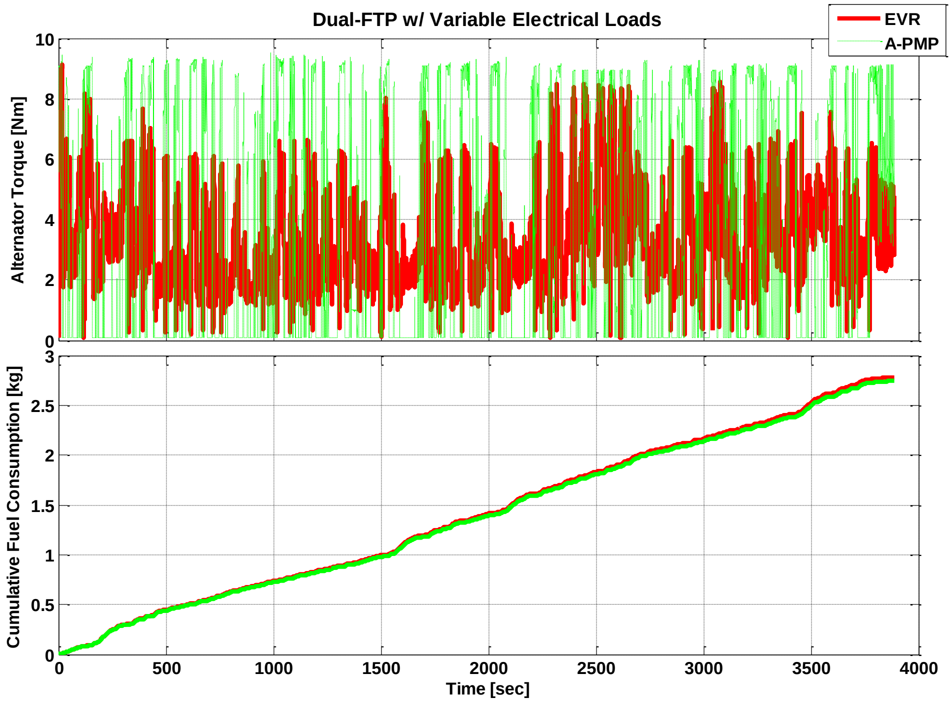

Figure 64: A-PMP Experimental Fuel Consumption, Dual-FTP w/ Variable Loads

While consistently beneficial to overall vehicle fuel economy, the A-PMP control strategy does present issues. The rapid switching behavior observed raises concern regarding accelerated wear-and-tear of the alternator and driver comfort/safety, and therefore measures should be taken to mitigate any unnecessary duty-cycle fluctuations. The battery voltage exceeds the maximum allowable value of 15 V on several occasions. Finally, although the SOC boundaries are successfully enforced in all experimental drive cycles, precautions should be taken as to ensure that the battery is never excessively charged or discharged. For example, if sensors fail and signals become erroneous, activation of the boundary penalty function may become insufficient to restrict the battery SOC operating range. Section 4.3 discusses potential solutions to these drivability issues, and experimentally demonstrates the effects which these solutions have on vehicle behavior.

Section 4.3: A-PMP Drivability Issues and Solutions

In order to ensure driver safety and comfort and guarantee acceptable VES performance, three critical issues associated with the A-PMP controller must be addressed:

1. A controller override, which functions as a safeguard against excessive battery charging/discharging, must be developed and integrated into the A-PMP control strategy.
2. Modifications to the controller must be made such that troublesome rapid switching behavior, characteristic of PMP control strategies, is mitigated.

3. The controller must be able to eliminate battery voltage spikes exceeding 15V.

Solutions to all 3 issues are developed, integrated into the A-PMP control strategy discussed in Section 4.1, and tested in-vehicle on the chassis dynamometer. Two separate experiments are performed on the chassis dynamometer in order to demonstrate the efficacy of the control modifications; a random “errand” drive cycle following no particular velocity trace, and an EPA drive cycle with only baseline electrical loads imposed on the system. It is important to note that for the two experiments performed in Section 4.3, the allowable battery state of charge range has been expanded from 82-88% to 80-90%.

4.3.1: Battery State of Charge Controller Override

Battery discharging and charging beyond the imposed state of charge limitations may result in a variety of undesirable vehicle behaviors, ranging from engine stalling to battery failure and even no-start conditions. There is thus a need to integrate a battery state of charge “fail-safe” control strategy into the existing A-PMP control strategy. This control strategy does not depend on the Hamiltonian to enact the appropriate control command (as is the case with the boundary penalty function), and is therefore a more reliable method of ensuring that the battery SOC remains within the allowable operating range. Assuming that the IBS does not fail, a simple method to implement this control strategy is placing a logic-based controller on the output of the A-PMP. The “SOC-Override” controller monitors the battery state of charge, and when an out-of-range SOC value is detected, an override on the duty-cycle command is enacted. This control override is developed in Mathworks Stateflow, and may be observed in Figure 65.

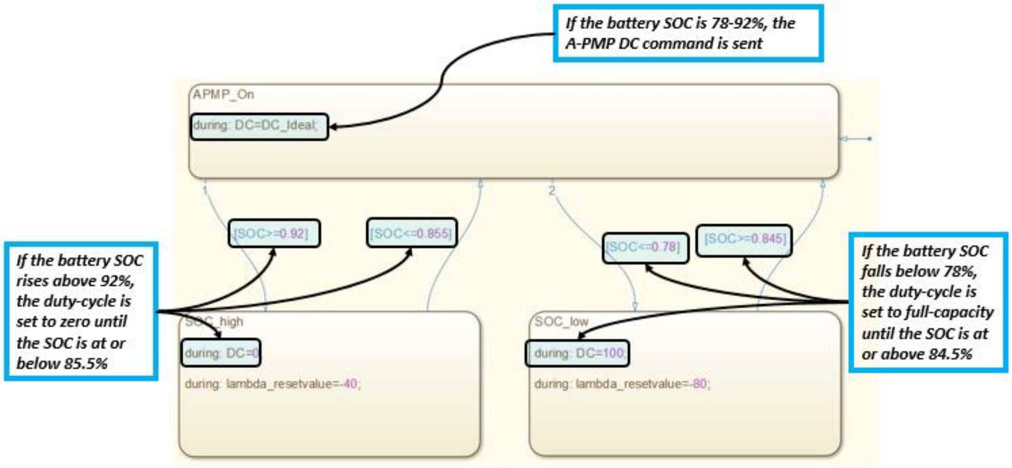

Figure 65: SOC Override Control Logic Implemented in Stateflow

4.3.2: Bang-Bang Behavior Mitigation and Elimination of Voltage Spikes

The rapid on-off switching behavior, or “Bang-Bang” behavior, which is observed in the duty-cycle plots featured in Section 4.2.2, will lead to accelerated aging of the alternator, the auxiliary belt, and possibly other ancillary loads if left untreated. Furthermore, the oscillations of the alternator duty-cycle lead to excessive charging current during deceleration events; the root cause of the undesirable battery voltage spikes. This bang-bang behavior is particularly troublesome at low electrical loads (i.e. baseline loads) during deceleration, and the frequency of oscillations can approach values of approximately 0.5 Hz. Figure 66 illustrates the severity of this issue over the first 500 seconds of Random Errand Cycle #1. Take note of the consistency with which bang-bang behavior accompanies deceleration events at low load demand.

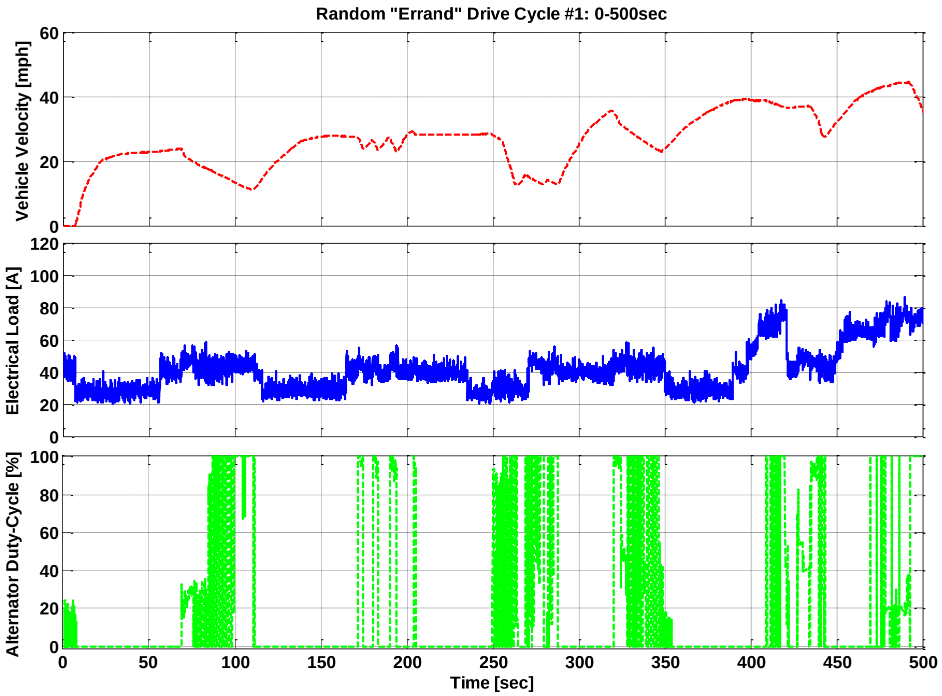

Figure 66: Bang-Bang Behavior, Random Drive Cycle #1

The source of the bang-bang behavior may be traced back to the Hamiltonian subsystem, where the fuel mass flow rate is weighted against the dynamics of the battery state of charge. As the vehicle accelerator pedal is released at low electrical loads, both the fuel mass flow rate and battery state of charge dynamics approach minimal values, resulting in an operating region of instability. The index corresponding to the minimum Hamiltonian value rapidly oscillates from one extreme (100% duty-cycle) to the other (0% duty-cycle), thus instigating the undesirable on-off behavior. One possible solution to this issue may be realized by implementing a filter on the outgoing duty-cycle command. This mitigates high-frequency duty-cycle dynamics, however numerous unsuccessful in-vehicle tests at OSU-CAR have demonstrated that this strategy can lead to unacceptably high battery voltages during acceleration due to the lag associated with the duty-cycle switching from 100% to 0%. Based on the specificity of the problematic vehicle operating points, a “patch” may be imposed on lambda during deceleration events at low electrical load demand which forces a predetermined duty-cycle command. As battery charging is consistently observed during vehicle deceleration, decreasing the co-state variable to a sufficiently negative value provides the desired behavior. The “lambda patch” monitors both a filtered engine torque signal and the filtered electrical load signal, activating only when both signals drop below a predetermined value (i.e. the “activation value”). Table 20 contains the critical lambda patch parameters and values.

Table 20: Lambda Patch Parameter Values

Lambda Override Value	***-140***
Activation Torque (Nm)	***35***
Activation Electrical Load (A)	***55***

The lambda patch parameter values were selected and tuned in-vehicle to ensure that lambda is only overridden when absolutely necessary in order to mitigate voltage spikes and bang-bang behavior. Section 4.3.3 features results of two experimental datasets with the modified A-PMP activated in the minivan.

4.3.3: Modified Controller Experimental Results

The A-PMP controller, complete with the modifications discussed in Sections 4.3.1 and 4.3.2, is implemented in the vehicle and two tests are conducted on the chassis dynamometer. The first test is an EPA (city plus highway) drive cycle, demonstrating the co-state override’s ability to mitigate undesirable bang-bang behavior. A random “errand” drive cycle is completed as well, ensuring the modified A-PMP controller’s performance over a variety of vehicle operating conditions. Table 21 summarizes the experimental improvement in fuel economy (over the baseline EVR controller) for the two drive cycles of interest.

Table 21: Experimental Improvement in Fuel Economy due to Modified A-PMP

Drive Cycle	% F.E.
EPA	1.0
Random Cycle #2	1.4

The modifications to the A-PMP controller do not result in any significant decrease in vehicle fuel economy. Figures 67-70 illustrate the critical vehicle, engine, and electrical system behavior for the low loads EPA drive cycle. Take special note of the reduction in duty-cycle bang-bang behavior (illustrated in greater detail in Figure 71) as well as the elimination of unacceptable battery voltage spikes. Figure 71 compares a roughly 300 second chunk of the modified A-PMP duty-cycle command to that of the original A-PMP duty-cycle for clarity.

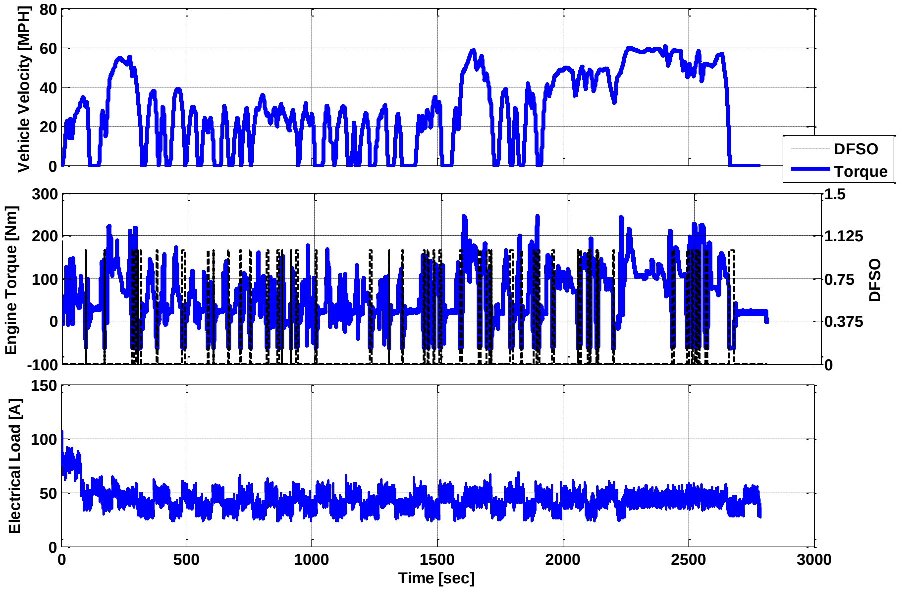

Figure 67: Modified A-PMP Experimental Vehicle Behavior, EPA

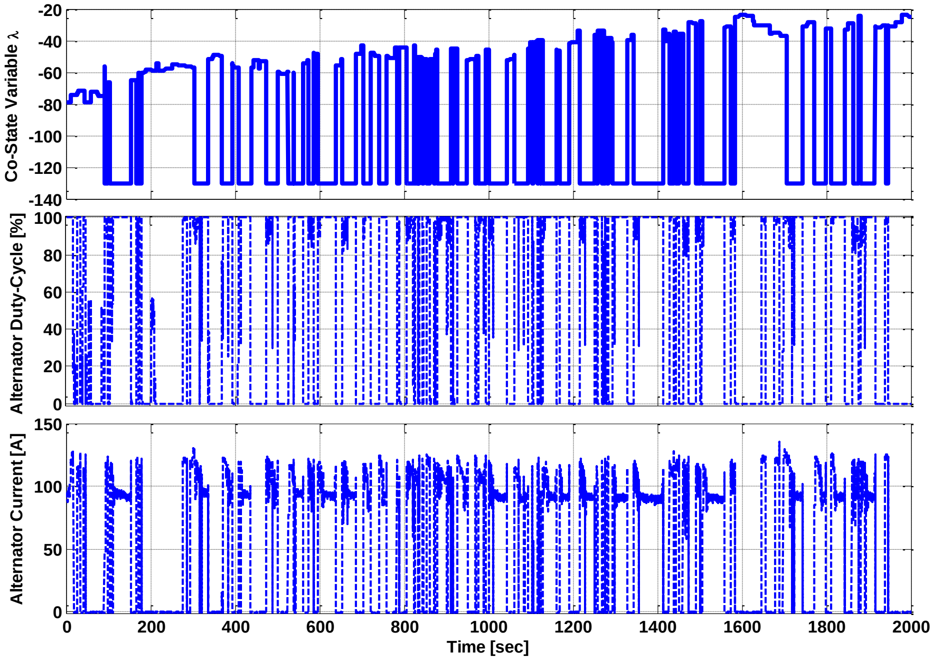

Figure 68: Modified A-PMP Experimental Control Behavior, EPA

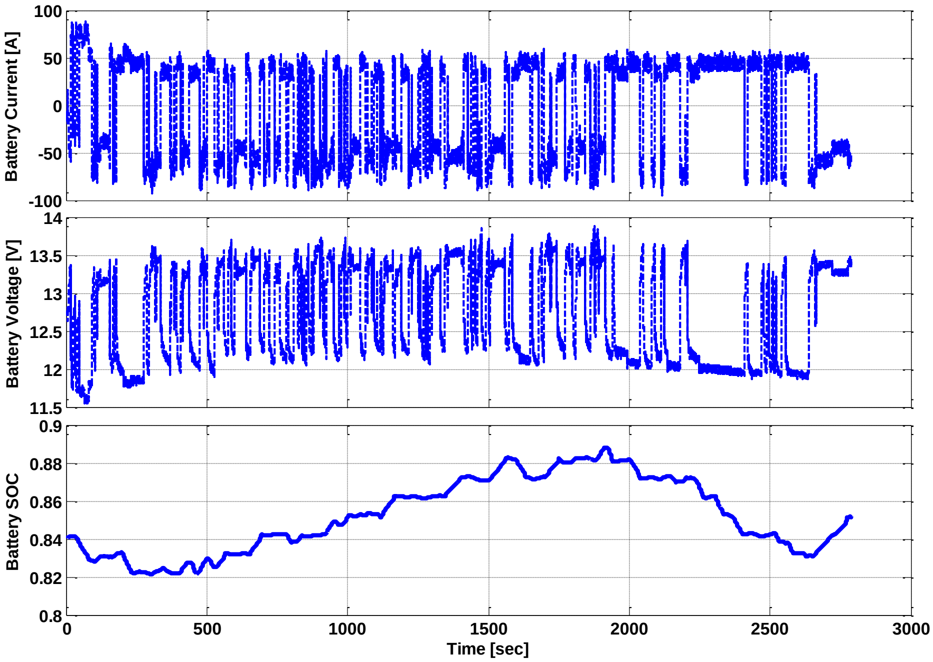

Figure 69: Modified A-PMP Experimental Battery Behavior, EPA

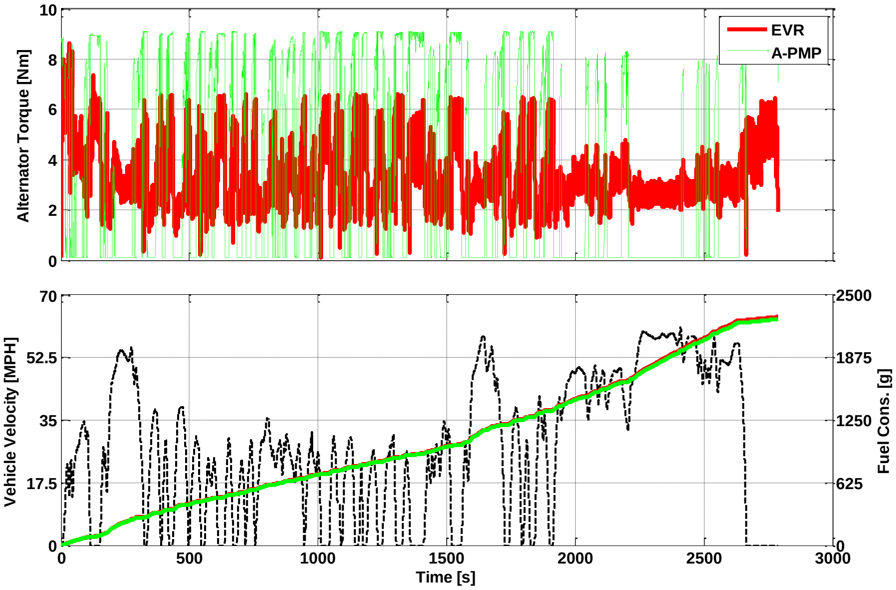

Figure 70: Modified A-PMP Experimental Fuel Consumption, EPA

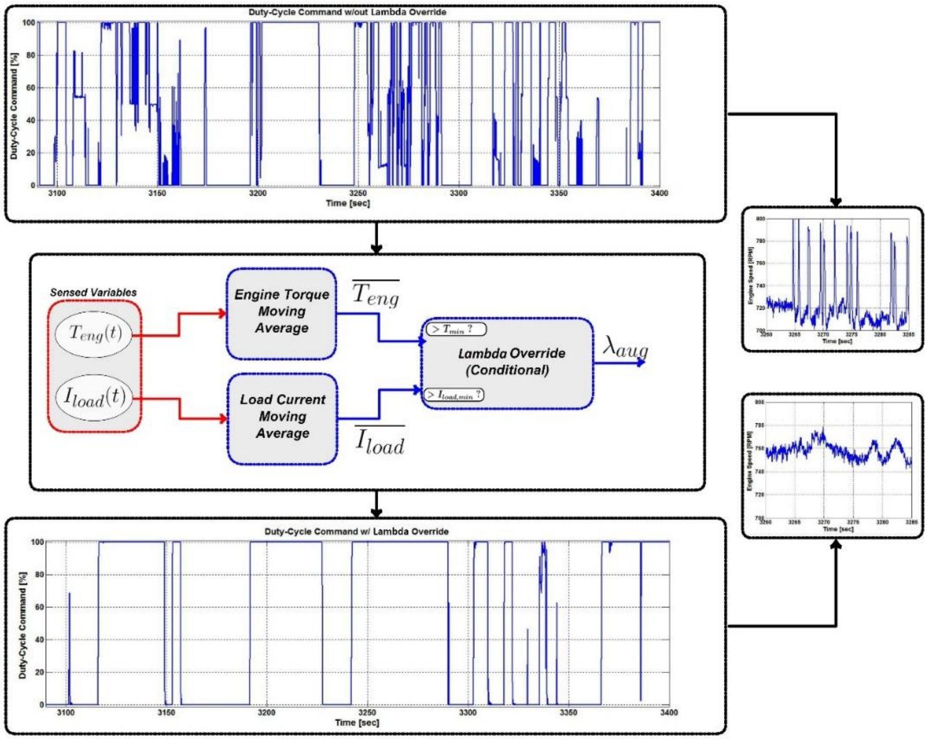

Figure 71: Mitigation of Bang-Bang Behavior

The bang-bang behavior of the A-PMP controller is reduced significantly, as may be directly observed in Figure 71. Figures 72-75 illustrate the critical vehicle, engine, and electrical system behavior for Random Drive Cycle #2.

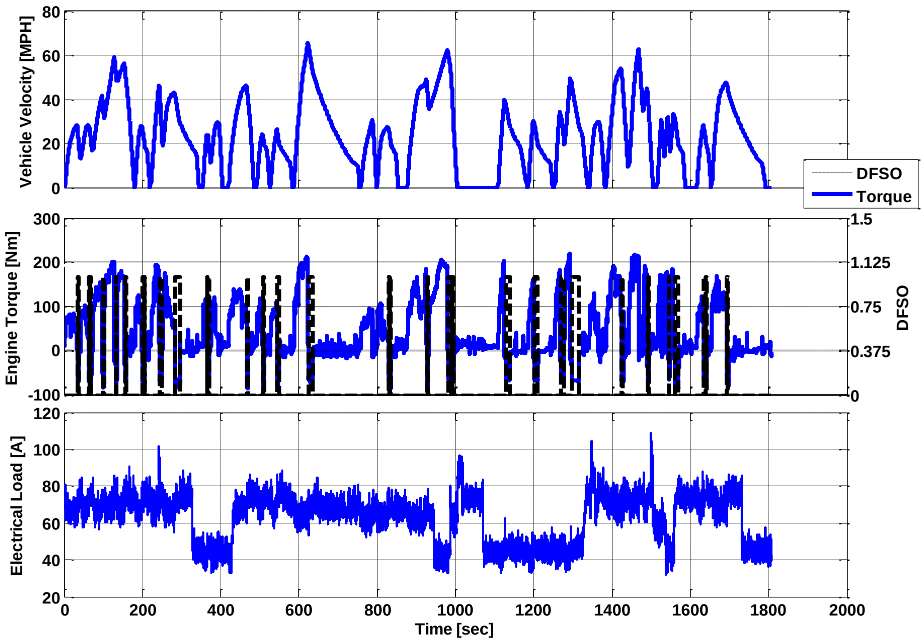

Figure 72: Modified A-PMP Experimental Vehicle Behavior, Random Drive Cycle 2

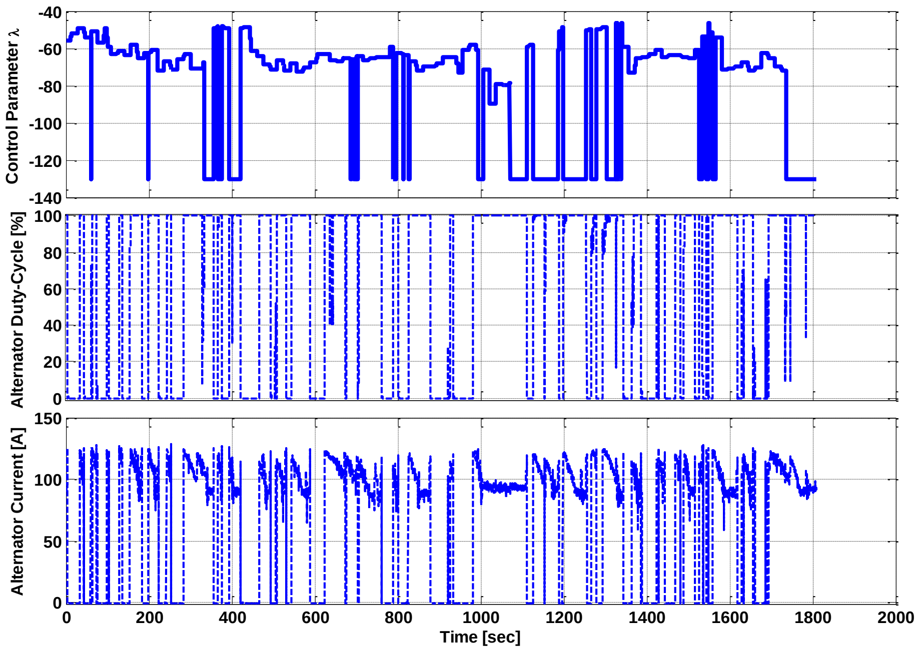

Figure 73: Modified A-PMP Experimental Control Behavior, Random Drive Cycle 2

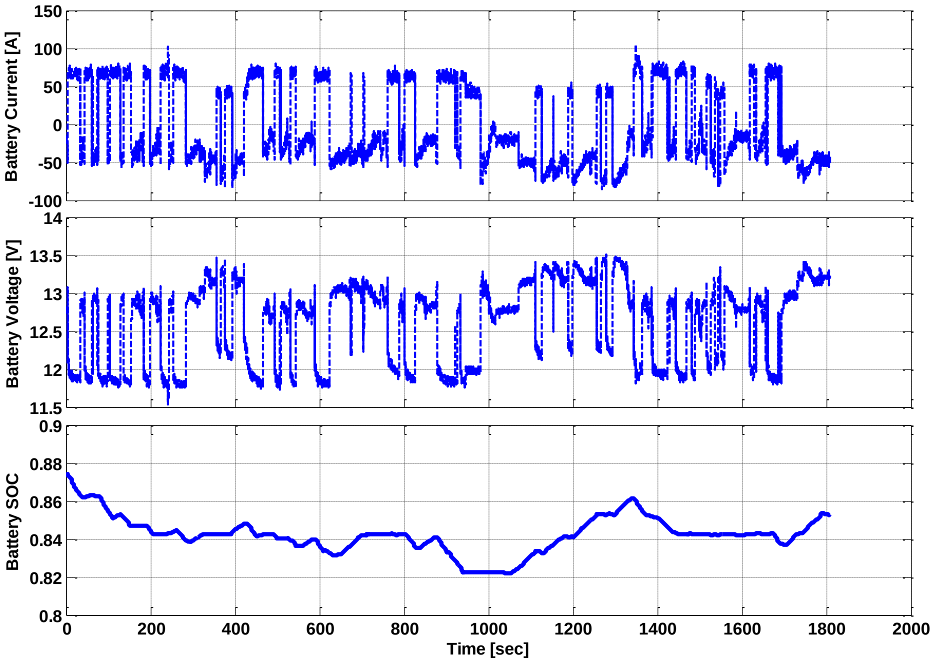

Figure 74: Modified A-PMP Experimental Battery Behavior, Random Drive Cycle 2

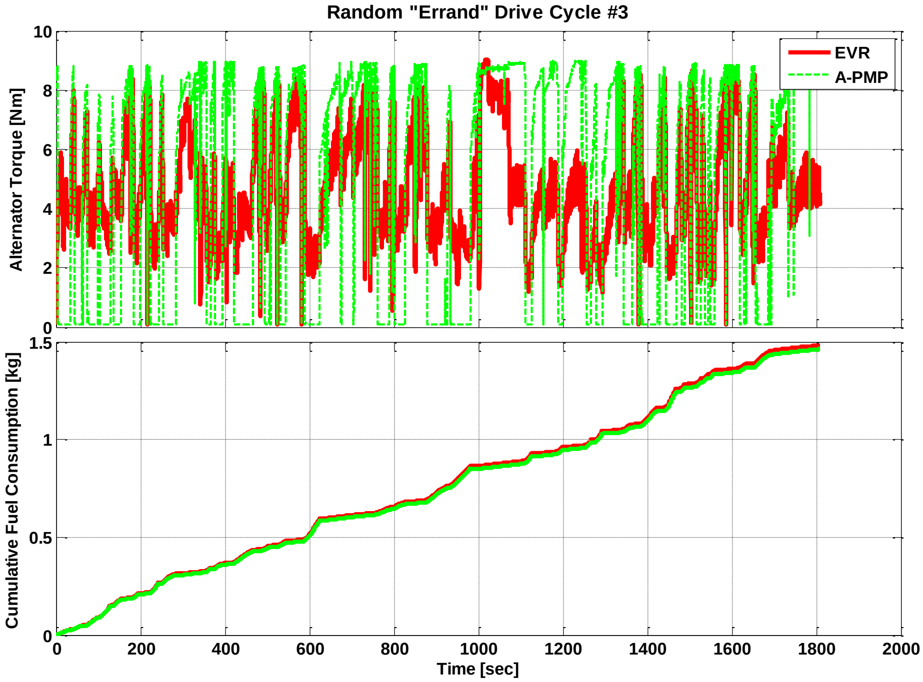

Figure 75: Modified A-PMP Experimental Fuel Consumption, Random Drive Cycle 2

Adaptations made to the optimal VES control strategy, as described in Chapter 3, have allowed for the development and implementation of a real-time capable control strategy which provides significant and consistent experimental improvements in vehicle fuel economy. Drivability issues relating to both component wear and driver comfort are addressed, with several possible solutions discussed, implemented and tested online. The necessary modifications employed have minimal influence on overall vehicle fuel economy.

Chapter 5: Conclusions and Future Work

Section 5.1: Conclusions

The vehicle production alternator control strategy, termed EVR, takes little advantage of the energy storage capabilities of the onboard automotive battery, simply holding the battery voltage to some temperature-dependent reference value. While this control strategy does ensure acceptable cold-cranking performance, significant fuel savings may be realized by implementing a less conservative VES control which takes advantage of the battery's ability to strategically harvest and release energy from the crankshaft. To this extent, an adaptive controller based on Pontryagin's Minimum Principle (PMP) is developed, implemented and tested in-vehicle. This controller is based on critical observations of VES behavior, in simulation, subjected to optimal control, which requires all drive cycle information (such as velocity, torque, engine speed, and electrical load profiles) "a-priori" and is thus impossible to successfully implement in real-time. In order to facilitate rapid controller development and tuning, virtual prototypes of the vehicle electrical system, the baseline EVR control strategy, the optimal PMP control strategy, and the adaptive PMP control strategy are all developed and validated utilizing computerized behavioral modeling tools. Previous work conducted at OSU-CAR has demonstrated that the experimental drive cycle to drive cycle variation of the vehicle of interest's fuel consumption, as measured by both the ECU and Big-Grid fuel consumption maps, may exceed 5% in certain instances. Concerns regarding this issue are mitigated by conducting dynamometer testing with the A-PMP activated, and comparing the experimental A-PMP fuel economy to the validated EVR model's fuel economy. Utilizing these analysis techniques, the A-PMP demonstrates consistent experimental improvements in vehicle fuel economy ranging from 1.1-1.4%. Drivability issues such as accelerated alternator wear-and-tear and unacceptable battery behavior (i.e. excessive charging/discharging) are addressed. Solutions to these issues are implemented and tested in-vehicle, demonstrating negligible effects on overall vehicle fuel economy.

Section 5.2: Future Work

While the present work experimentally demonstrates the potential of an adaptive, PMP-based control strategy to improve vehicle fuel economy while maintaining driver comfort and component reliability, numerous opportunities for extending the scope of this research exist. Completion of the following tasks may allow for further increases in vehicle fuel economy and more precise estimations of the fuel economy benefit which the A-PMP control strategy brings about.

1. **Improved VES Model.** The fully integrated Vehicle Electrical System model, composed of a battery, alternator, and EVR model, has been validated and agrees well with experimental data sets collected across a wide variety of operating conditions. Nonetheless, due to the nature of the analysis techniques used to estimate the A-PMP fuel economy benefit, a more precise VES model would provide useful insight into the experimental vehicle fuel consumption of the EVR-

equipped vehicle. The development of an alternator model which is not strictly based on empirically-derived steady-state data and takes into account the dynamics of the alternator may prove useful to this extent [22].

2. **Expansion of Optimal Control to Load Shedding.** Just as strategic utilization of the alternator and battery reduces overall vehicle fuel consumption, selective reduction of the electrical load demand may allow for more fuel-efficient VES behavior. Studies similar to those performed in Section 3.2, and the resulting experiments described in Section 4.2, may therefore be expanded to allow for a temporary reduction in electrical load demand. This would require the incorporation of a separate term into the Hamiltonian function with an adaptive co-state variable. Furthermore, experimental calibration of the allowable time for which a load may be shed would need to be carried out to ensure driver comfort.

References

[1] “Number of Drivers and Motor Vehicles in the United States, 1960-2009.” Earth Policy Institute, 2012.

[2] “US Auto Industry sees best sales since 2007; recovery expected to slow in 2014.” Michigan Local News, 2013.

[3] “The Road to 2020 and Beyond: What’s Driving the Global Automotive Industry?” Advanced Industries, 2013.

[4] “Highway Statistics 2007; Licensed Drivers, Vehicle Registrations, and Resident Population.” U.S. Department of Transportation, Federal Highway Administration, 2012.

[5] “Annual Energy Outlook 2013.” U.S. Energy Information Administration, 2013.

[6] F. Chiara, M. Canova, and G. Rizzoni. “Future Mobility Challenges, Where Will We Find Fuel Efficient Solutions?” The Ohio State University, 24 April 2012. Print.

[7] “Frost and Sullivan Analysis Suggests Momentum toward Supplementary 48V On-board Power-net.” *Green Car Congress*, 2012.

[8] “Automakers Expanding 48-V Production Plans, says AVL Electrification Chief.” SAE International, 2014.

[9] Chong, Andrew. “Driving Asia – As Automotive Electronics Transforms a Region.” Infineon Technologies Asia Pacific Pte Ltd, 2010. Print.

[10] Hardin, Christopher. “Effect of Automotive Electrical System Changes on Fuel Consumption Using an Incremental Efficiency Methodology.” Thesis. Massachusetts Institute of Technology, 2004. Print.

[11] Bryson, Arthur. “Optimal Control – 1950-1985.” IEEE Control Systems, 1996.

[12] N. Kim, C. Sukwon, H. Peng. “Optimal Control of Hybrid Electric Vehicles Based on Pontryagin’s Minimum Principle.” IEEE Transactions on Control Systems, 2011.

[13] D. Ambuhl, O. Sundstrom, A. Sciarretta, L. Guzzella. “Explicit Optimal Control Policy and its Practical Application for Hybrid Electric Powertrains.” IFAC Journal Of Control Engineering Practice, 2010.

[14] X. Zhang, C. Mi. “Vehicle Power Management: Modeling, Control and Optimization.” Springer, 2011. Print.

[15] J. Liu, H. Peng. “Modeling and Control of a Power-Split Hybrid Vehicle.” IEEE Transactions on Control Systems Technology, 2008.

[16] S. Onori and L. Serrao. “On Adaptive-ECMS Strategies for Hybrid Electric Vehicles.” *Les Rencontres Scientifiques d’IFP Energies Nouvelles,* 2011. Print.

[17] S. Onori, L. Serrao, G. Rizzoni. “Adaptive Equivalent Consumption Minimization Strategy for Hybrid Electric Vehicles.” Proceedings of the ASME 2010 Dynamic Systems and Control Conference, 2010.

[18] S. Stockar, V. Marano, M. Canova, G. Rizzoni, L. Guzzella. “Energy-Optimal Control of Plug-in Hybrid Electric Vehicles for Real-World Driving Cycles.” IEEE Transactions on Vehicular Technology, 2011.

[19] J. Kessels, M. Koot, B. Jager, P. Bosch, N. Aneke, D. Kok. “Energy Management for the Electric Powernet in Vehicles with a Conventional Drivetrain.” IEEE Transactions on Control Systems Technology, 2007.

[20] J. Couch, M. Canova, L. Fiorentini. “An ECMS-based Approach for the Energy Management of a Vehicle Electrical System.” The International Federation of Automatic Control, 2013.

[21] Ma, Xiaoliang. “Optimal Controls of Fleet Trajectories for Fuel and Emissions.” IEEE Intelligent Vehicles Symposium, 2013.

[22] A. Scacchioli, G. Rizzoni, M. Salman, W. Li, S. Onori, X. Zhang. “Model-based Diagnosis of an Automotive Electric Power Generation and Storage System.” IEEE Transactions on Systems, Man, and Cybernetics: System, 2014.

[23] Ceraolo, Massimo. “New Dynamic Models of Lead-Acid Batteries.” IEEE Transactions on Power Systems, 2000.

[24] N. Moubayed, J. Kouta, A. El-Ali, H. Dernayka, R. Outbib. “Parameter Identification of the Lead-Acid Battery Model.” IEEE Paper 978-1-4244-1641-7.

[25] Mayer, D. “Modelling and Analysis of Lead Acid Battery Operation.” Telecommunications Energy Conference, 1989.

[26] A. Scacchioli, G. Rizzoni, and P. Pisu. “Model-Based Fault Detection and Isolation in Automotive Electrical Systems.” *ASME International Mechanical Engineering Congress and Exposition*, 2006. Print.

[27] Y. Hu, S. Yurkovich, Y. Guezennec, and B.J. Yurkovich. “Electro-Thermal Battery Model Identification for Automotive Applications.” *Journal of Power Sources* 196, 2011. Print.

[28] Jackey, Robyn. A. “A Simple, Effective Lead-Acid Battery Modeling Process for Electrical System Component Selection.” SAE Paper 2007-01-0778.

[29] Jiang, Shugang. “A Parameter Identification Method for a Battery Equivalent Circuit Model.” SAE Paper 2011-01-1367.

[30] K. Salloux, J. McHardy. “Eliminating Battery Failure – Two New Leading Indicators of Baterrry Health – A Case Study.” IEEE Telecommunications Energy Conference, 2007.

[31] Couch, Jeremy. “An ECMS-based Controller for the Electrical System of a Passenger Vehicle.” Thesis. The Ohio State University, 2013.

[32] S. Chiniforoosh, A. Davoudi, P. Alaeinovin, J. Jatskevich. “Dynamic Modelling and Characterization of Vehicular Power System Considering Alternator Iron Core and Rectifier Losses.” IET Electrical Systems in Transportation, 2012.

[33] Yedeg, Esubalewe. “Control and Design of Engineering Mechanics Systems.” Thesis. Umea University, Sweden, 2013.

[34] L. Serrao, S. Onori, G. Rizzoni. “ECMS as a Realization of Pontryagin’s Minimum Principle for HEV Control.” American Control Conference, 2009